

4.9 Laserresonator

Versuchsanleitung zum Fortgeschrittenen-Praktikum

Abteilung A

Version 2.3



TECHNISCHE
UNIVERSITÄT
DARMSTADT

Fachbereich Physik
Institut für Angewandte Physik
AG Nichtlineare Optik/Quantenoptik



Inhaltsverzeichnis

Versuchsanleitung	3
-------------------	---

Anhang

The World of Fabry-Perots	10
The Spherical Mirror Fabry-Perot Interferometer	16
Laser Beams and Resonators	32
SA200-Series Scanning Fabry-Perot Interferometer Datenblatt	50
SA210-Series Scanning Fabry-Perot Interferometer Datenblatt	51
SA201 Spectrum Analyzer Controller Anleitung	56
S120C Leistungsmesskopf Datenblatt	67
PM100D Leistungsmessgerät Kurzanleitung	71
PicoScope 3000 PC-Oszilloskop Anleitung	83

Vorbereitung

- **Laserprinzip:** Besetzungsinversion, Anregungsmechanismen, 3- und 4-NiveauSystem, Einwegverstärkung
- **Laseroszillatoren:** Verstärkung durch Rückkopplung, Laseroszillator, Modenspektrum von Laseroszillatoren, Bandbreite, Eigenschaften der Laserstrahlung, HeNe-Gaslaser.
- **Resonatortheorie:** Optische Resonatoren, Resonatorgeometrie, (planparallel, konfokal, hemisphärisch) und deren Eigenschaften, Stabilitätsdiagramm, Verluste optischer Resonatoren, Moden (transversal und longitudinal), Fabry-PerotInterferometer, Gauß-Optik.
- Gefahren durch Laserstrahlung (siehe z.B. [Wikipedia](#))
- **Vorbereitende Aufgaben:** Gehen Sie die einzelnen Versuchsteile durch und bearbeiten Sie die drei Vorbereitungsaufgaben. Sollten Fragen zur Vorbereitung oder den Vorbereitungsaufgaben aufkommen, können Sie sich bis einschließlich freitags vor dem Versuch per Mail an den Betreuer wenden.

Überlegen Sie sich vor Versuchsbeginn welche Größen gemessen werden müssen und erstellen Sie einen Messplan, der sämtliche zu messenden Größen inkl. Fehlerangaben(!) jedes Aufgabenteils enthält.

Literatur

- W. Demtröder: „*Laserspektroskopie: Grundlagen und Techniken*“, 6. Aufl.
- F.K. Kneubühl, M.W. Sigrist: „*Laser,*“ Vieweg + Teubner (2008)
- J. Eichler, H.-J. Eichler: „*Laser: Bauformen, Strahlführung, Anwendungen*“, 8. Aufl.
- M. Hercher: „*The Spherical Mirror Fabry-Perot-Interferometer*“, Applied Optics **7** 951 (1968) (siehe Anhang)
- H. Kogelnik, T. Li: „*Laser Beams and Resonators*“, Applied Optics **5**, 1550 (1966) (siehe Anhang)
- W.S. Gornall: „*The World of Fabry-Perots*“, Lasers & Applications, 47 (July 1983) (siehe Anhang)

Einleitung

Seit der Erfindung des Lasers (light amplification by stimulated emission of radiation) in den 1960er Jahren hat dieser weitreichende Anwendungen gefunden. Diese Anwendungen beinhalten bspw. hochaufgelöste Spektroskopie, zeitlich aufgelöste Studien molekularer Dynamik mittel Erzeugung ultrakurzer Lichtpulse, Fangen und Kühlen von Atomen zur Erzeugung von Bose-Einstein Kondensaten, Medizin/Chirurgie (z.B. Laserskalpell), Messtechnik (z.B. Abstandsmessung), Materialbearbeitung in der Industrie und Unterhaltungselektronik (CD/DVD-Spieler).

Das Grundprinzip des Lasers lässt sich kurz folgendermaßen zusammenfassen:

Ein Laser besteht im Wesentlichen aus drei Komponenten:

- einem *verstärkenden Medium*, in das von
- einer „*Energiepumpe*“ selektiv Energie hineingepumpt wird und
- einem *Resonator*, der einen Teil dieser Energie in Form elektromagnetischer Wellen in wenigen Resonatormoden speichert.

Die Energiepumpe erzeugt im Lasermedium eine vom thermischen Gleichgewicht extrem abweichende Besetzung eines oder mehrerer Energieniveaus. Bei genügend großer Pumpleistung wird zumindest für ein Energieniveau E_k die Besetzungsdichte $N_k(E_k)$ größer als die Besetzungsdichte $N_i(E_i)$ für ein energetisch tiefer liegendes Niveau E_i , das mit E_k durch einen erlaubten Übergang verbunden ist (Inversion). Da in einem solchen Fall die induzierte Emissionsrate auf dem Übergang $E_k \rightarrow E_i$ größer wird als die Absorptionsrate, kann Licht beim Durchgang durch das aktive Medium verstärkt werden. Die Aufgabe des Resonators ist es nun, Licht, das von den durch die Pumpe aktivierten Atomen des Lasermediums emittiert wird, durch selektive, optische Rückkopplung wieder durch das verstärkende Medium zu schicken und dadurch aus dem Laserverstärker einen selbstschwingenden Oszillator zu machen. Mit anderen Worten: Der Resonator speichert das Licht in wenigen Resonatormoden, so dass in diesen Moden die Strahlungsdichte groß wird und damit die induzierte Emission wesentlich größer als die spontane Emission werden kann.

Während alle Laser auf diesem Prinzip basieren, ist die technische Realisierung der drei Komponenten Resonator-Pumpe-Medium recht vielfältig. Die Pumpe lässt sich z.B. durch Blitzlampen, Gasentladungen, Strom oder auch andere Laser implementieren. Aktive Medien reichen von Gasen, dotierten Festkörperkristallen, Halbleitern, bis zu in Flüssigkeiten gelösten Farbstoffen.

In diesem Versuch soll das Laserprinzip anhand eines Helium-Neon-Gaslasers veranschaulicht werden. Durch Aufbau und Justage eines Resonators um das aktive Medium soll zuerst die Laseroszillation erreicht und dann die im folgenden aufgeführten Aufgaben bearbeitet werden.

Versuchsdurchführung & Auswertung

WICHTIG: Dokumentieren Sie immer **alle** Messergebnisse der einzelnen Aufgaben! Die Messdaten sind am Ende des Versuchs vom Betreuer unterzeichnen zu lassen.

WICHTIG: Die Gasentladung im Lasermedium wird über eine Hochspannung von mehreren kV gezündet. Berühren Sie nicht die Anschlüsse! Das Lasermedium inkl. Halterung darf **nicht** von der Schiene genommen und nur vom Betreuer bewegt werden!

WICHTIG: Die während der Versuchsdurchführung aufgenommenen Messwerte sind **im Original** in die Auswertung einzufügen! Trennen Sie die Auswertung der Messwerte von der Versuchsdurchführung! Es muss **nachvollziehbar** sein, wie die Auswertungsergebnisse aus den Messdaten erhalten wurden!

Aufgaben:

1. Inbetriebnahme des Laserresonators

Benutzen Sie den Justierlaser sowie die Irisblende um eine optische Achse zu definieren. Richten Sie dann das Laserrohr und die Resonatorspiegel bzgl. dieser Achse aus. Achten Sie hierbei darauf, dass der Strahl des Justierlasers mittig durch das Laserrohr läuft und die Resonatorspiegel zentrisch trifft.

Der Krümmungsradius der Spiegel beträgt $R = 450 \text{ mm}$ und der Spiegeldurchmesser beträgt $d_M = 7.75 \text{ mm}$. Der Durchmesser des Laserrohrs beträgt ca. $d_R = 1.0 \text{ mm}$ und seine Länge ca. $L = 20 \text{ cm}$.

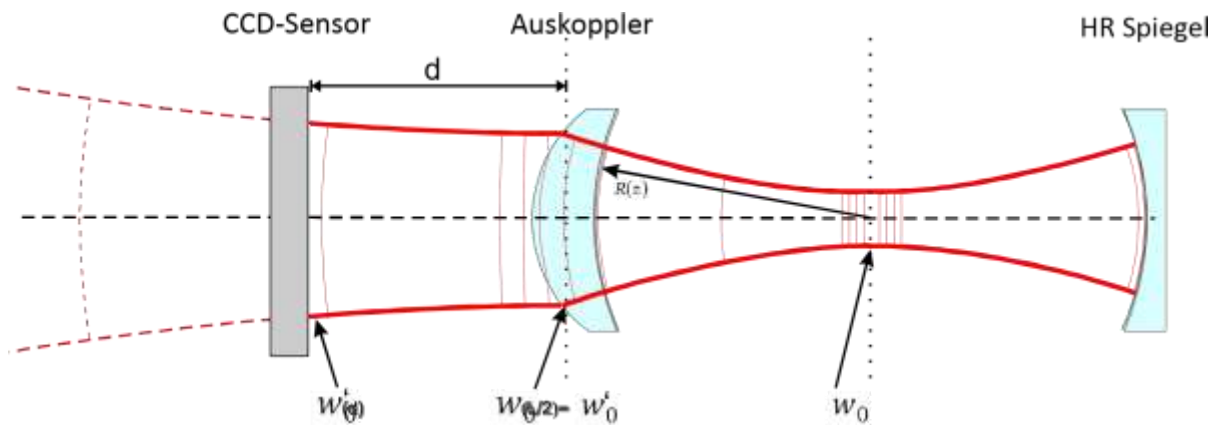
Führen Sie nun die Aufgaben 2-4 für 8 Resonatorlängen jeweils nacheinander durch. Das Lasermedium soll sich bei jeder Messung in der Mitte des Resonators befinden. **Beginnen Sie mit** einem Spiegelabstand von **30 cm** und vergrößern Sie diesen dann schrittweise (einzustellende Resonatorlängen in cm: 45, 55, 65, 75, 85, 88). Nehmen Sie zusätzlich eine weitere Messung für eine Resonatorlänge $> 88 \text{ cm}$ auf. Achten Sie hier darauf, dass Sie sich trotzdem innerhalb der Stabilitätsgrenzen aufhalten.

2. Ausgangsleistung des Lasers in Abhängigkeit von der Resonatorlänge

Aufgabe zur Vorbereitung: Erstellen Sie eine Messwert-Tabelle mit den 8 zu untersuchenden Resonatorlängen. Die Tabelle sollte neben Feldern für die Messwerte und den Fehler auch zwei Spalten für die Spiegelpositionen nebst Fehler, sowie eine Spalte für Kommentare beinhalten.

Messen Sie die Ausgangsleistung des Lasers in Abhängigkeit von der Resonatorlänge und bestimmen Sie so die Stabilitätsgrenze des Resonators. Tragen Sie die Ergebnisse graphisch auf. Diskutieren Sie die Ergebnisse.

Hinweise: Maximieren Sie die Ausgangsleistung für jeden Messpunkt durch Justage der Spiegel und des Laserrohrs.



3. Strahlbreite der Grundmode in Abhängigkeit von der Resonatorlänge

Aufgaben zur Vorbereitung: Berechnen Sie für die beiden Resonatorlängen von 30cm und 88cm den Strahldurchmesser der TEM₀₀-Mode am Auskoppelspiegel.

Bestimmen Sie für die beiden Resonatorlängen 30cm und 88cm den Fehler (in Prozent vom erwarteten Messwert), der sich aus der Vereinfachung für einen Abstand $d=8\text{cm}$ ergibt. Diskutieren Sie später in der Auswertung gegebenenfalls dessen Relevanz.

(a) Aufnahme der Messdaten

Bestimmen Sie Strahlbreite w am Ort des Auskoppelspiegels in Abhängigkeit von der Resonatorlänge. Nehmen Sie hierzu die Intensitätsverteilung der ausgekoppelten Laserstrahlung mit Hilfe einer CCD-Kamera in festem und möglichst geringem Abstand d vom Auskoppelspiegel auf (siehe Abb. 1). Die Maße der aktiven Sensorfläche betragen 4,8mm horizontal und 3,6mm vertikal. Achten Sie bei der Aufnahme der Bilder darauf, dass der Chip nicht übersättigt ist!

Für jede Resonatorlänge soll die TEM₀₀-Mode des Lasers angeregt werden. Dies kann z.B. durch verkippen des Laserrohres erreicht werden. Die Bildaufnahme erfolgt über das Programm **Beamscope**. Die Messdaten befinden sich im Ordner „D:/Measurement Data/Beamscope VGA/“. Das Programm erstellt automatisch einen horizontalen und einen vertikalen Schnitt durch das Maximum der Intensitätsverteilung. Tragen Sie die aus einer nichtlinearen Regression erhaltenen Strahlbreiten w in einem Diagramm über der Resonatorlänge auf. Die Betrachtung eines vertikalen und horizontalen Schnitts ermöglicht einen Rückschluss auf die Genauigkeit der Messung.

(b) Vergleich mit berechneten Werten.

Der Auskoppelspiegel besitzt eine gewölbte Außenfläche und kollimiert den Gauß'schen Laserstrahl mit dem Strahlradius $w(L/2)$. Das heißt, es bildet sich ein neuer Gauß'scher Strahl mit der Strahltaile $w_0' = w(L/2)$ aus. Für kleine Abstände d können Sie daher zunächst davon ausgehen, dass $w_0' = w'(d)$. Tragen Sie die berechneten Werte in das in 2(a) erzeugte Diagramm ein. Diskutieren Sie das Ergebnis.

4. Longitudinale Modenstruktur in Abhängigkeit von der Resonatorlänge

Beobachten Sie die longitudinale Modenstruktur des HeNe-Resonators in Abhängigkeit der Resonatorlänge und vergleichen Sie die Ergebnisse mit der Theorie. Die longitudinale Modenstruktur wird mit dem Fabry-Perot Interferometer (Thorlabs SA210 bzw. SA200 & Steuergerät SA201) gemessen. Das Ausgangssignal des Interferometers kann mit einem Digitaloszilloskop (Pico Modell 3204) auf den PC mittels des Programms **PicoScope** übertragen werden.

Bestimmen Sie nun den Modenabstand in Abhängigkeit der Resonatorlänge. Vergleichen Sie in einer Tabelle die gemessenen mit berechneten Werten und tragen Sie die Werte in einem Diagramm mit der theoretischen Kurve auf.

Achten Sie darauf, während der Messung nur die TEM₀₀-Mode anzuregen! Kalibrieren Sie zunächst die Zeitskala des Oszilloskops mit Hilfe des freien Spektralbereichs des Interferometers zur späteren Umrechnung von der Zeitbasis in den in Frequenzraum.

Achten Sie bei jeder Messung darauf, dass auf dem Oszilloskop klar separierbare, symmetrische Lorenz-Linien erkennbar sind. Justieren Sie gegebenenfalls die Verkippung des Interferometers im Bezug auf den Laserstrahl und stellen sie sicher, dass der Laserstrahl die Eingangs-Iris des Detektors mittig trifft. Stellen Sie die Iris zur Messung auf den kleinsten Durchmesser ein.

Speichern Sie die Daten jeweils im .txt und .png-Format (zur späteren Kontrolle).

Entfernen Sie bei der Justage des Fabry-Perot Interferometers nicht den Detektor, wie in dessen Anleitung beschrieben wird!

5. Verstärkungsbandbreite des HeNe-Lasers.

(a) Aufnahme der Messdaten mithilfe der Persistenz-Funktion

Untersuchen Sie die Verstärkungsbandbreite des Lasers für mindestens eine Resonatorlänge. Die „Persistenz“-Funktion des Oszilloskops eignet sich aufgrund des vorhandenen Moden-Jitters zur Aufnahme des Verstärkungsprofils. Es kann nur ein PNG-Bild der OszilloskopAnzeige gespeichert werden, die grafisch ausgewertet werden muss. Es empfiehlt sich, diese Aufgabe bei einer Resonatorlänge von 60-81cm durchzuführen.

Nehmen Sie das Verstärkungsprofil bei maximaler Ausgangsleistung der TEM₀₀-Mode auf. Bestimmen Sie anschließend die Ausgangsleistung. Reduzieren Sie nun die Ausgangsleistung durch Erhöhen der Beugungsverluste auf die Hälfte des Ausgangswertes. Wiederholen Sie die Messung.

(b) Bestimmen der Verstärkungsbandbreite

Benutzen Sie die in Aufgabe 4 gemachte Kalibrierung der Zeitskala des Oszilloskops zur Bestimmung der Frequenzbandbreite des Verstärkungsprofils. Erläutern Sie den Einfluss der Verluste auf die Verstärkungsbandbreite anhand der Messung. Diskutieren Sie die erhaltenen Werte im Hinblick auf die theoretisch zu erwartende Verstärkungsbandbreite.

6. Beobachtung höherer transversaler Moden.

(a) Aufnahme der Messdaten mittels CCD-Kamera

Nehmen Sie **mindestens vier Bilder** der Intensitätsverteilung unterschiedlicher TEM-Moden mit dem Programm **Beamscope** auf. Der Schalter „LIVE“ ermöglicht es, das Bild einer Intensitätsverteilung zum Speichern einzufrieren. Wählen Sie möglichst Transversal, deren Verteilung *klar* erkennbar ist und die Sie identifizieren können. Speichern Sie die Bilder als BMP-Dateien. Notieren sie für jede Mode, auf welche Art und Weise sie erzeugt wurde und welcher Resonatorlänge genutzt wurde.

Achten Sie auch hier auf eine gute Sensorbelichtung. Sie können durch Nutzung der Mittelungsfunktion das Bildrauschen verringern. Achten Sie dabei jedoch darauf, dass nicht verschiedene Transversalmoden zu einem Bild akkumuliert werden.

(b) Räumliche Intensitätsverteilung der Moden.

Legen Sie sinnvoll ausgerichtete Schnitte entlang der Symmetrieachsen durch die Intensitätsverteilung der Moden. Hierzu dient das Programm **SliceBMP**. Die Position der Schnitte lässt sich durch die Schieberegler rechts und oben am Bild anpassen. Die Drehung durch Eingabe eines Winkels und Bestätigung mit Enter. Mit Klick auf „Schnitt erstellen“ Werden sowohl das gedrehte Bild, als auch die beiden Intensitätsprofile im angegebenen Ordner gespeichert.

(c) Vergleich der gemessenen Werte mit berechneten Intensitätsverteilungen.

Plotten Sie die berechneten Intensitätsverteilungen im jeweils zugehörigen Graph der gemessenen Verteilung aus 6(a). Passen Sie für die Berechnung die Amplitude und die Strahlbreite w der theoretischen Verteilung an die experimentellen Daten an.

Stellen Sie in der Auswertung links neben dem Graph die zweidimensionale Intensitätsverteilung mit den Schnittgeraden dar, welche die Lage des benutzten Schnittes innerhalb der Intensitätsverteilung aufzeigt. Diskutieren Sie die Qualität der Graphenanpassung an die Messdaten.

Vergleichen sie den erhaltenen Radius mit dem Radius der Grundmode bei gleicher Resonatorlänge aus Aufgabe 3(a). Diskutieren Sie die Ergebnisse im Hinblick auf die theoretische Beschreibung der Transversalmoden.

Wichtige Punkte zum Laserschutz

Ganz allgemein gilt: Im Umgang mit Lasern ist der gesunde Menschenverstand nicht zu ersetzen! Einige spezielle Hinweise werden im Folgenden angeführt.

1. Die Laserschutzvorschriften sind immer zu beachten.
2. Halten Sie Ihren Kopf niemals auf Strahlhöhe.
3. Die Justierbrille immer aufsetzen.
4. Schauen Sie nie direkt in Strahl – auch nicht mit Justierbrille!
5. Achtung: praktisch alle Laser für Laboranwendungen sind mindestens Klasse 3, also von vornherein für die Augen gefährlich, ggf. auch für die Haut – evtl. auch hierfür Schutzmaßnahmen ergreifen. Zur Justage kann der Laserstrahl mittels einem Stück Papier sichtbar gemacht werden.
6. Auch Kameras besitzen eine Zerstörschwelle!
7. Spiegel und sonstige Komponenten nie in den ungeblockten Laserstrahl einbauen! Vor Einbau immer überlegen, in welche Richtung der Reflex geht! Diese Richtung zunächst blocken, bevor der Strahl wieder frei gegeben wird.
8. Nie mit reflektierenden Werkzeugen im Strahlengang hantieren! Unkontrollierbare Reflexe! Vorsicht ist z.B. auch mit BNC-Kabeln geboten, die in den Strahlengang gelangen könnten! Gleiches gilt auch für Uhren und Ringe. Diese vorsichtshalber ausziehen, wenn Sie mit den Händen im Strahlengang arbeiten.
9. Auch Leistungsmessgeräte können Reflexe verursachen! Unbeschichtete Silizium-Fotodioden reflektieren über 30% des Lichtes!
10. Achtung im Umgang mit Strahlteilerwürfeln! Diese haben immer einen zweiten Ausgang! Ggf. abblocken!
11. Warnlampen bei Betrieb des Lasers anschalten und nach Beendigung der Arbeit wieder ausschalten.
12. Dafür sorgen, dass auch Dritte im Labor die richtigen Schutzbrillen tragen, oder sich außerhalb des Laserschutzbereiches befinden.
13. Filtergläser in Laserschutzbrillen dürfen grundsätzlich nicht aus- oder umgebaut werden!!!
14. In besonderem Maße auf Beistehende achten.
15. Optiken (Linsen, Spiegel etc.) nicht direkt mit den Fingern berühren!

Hiermit erkläre ich, dass ich die vorstehenden Punkte gelesen und verstanden habe. Ich bestätige, dass ich eine Einführung in den Umgang mit Lasern sowie eine arbeitsplatzbezogene Unterweisung erhalten habe.

Name:

Unterschrift:

Datum:

The World of Fabry-Perots

These Elegant Instruments Are Versatile, High-Resolution Tunable Wavelength Filters

by William S. Gornall

The Fabry-Perot interferometer was invented by two French opticians, Charles Fabry and Alfred Perot¹ in 1897. For decades it received limited use even in spectroscopic research because few emission sources were sufficiently monochromatic to take advantage of its high resolving power. The advent of lasers in the early 1960s produced a renaissance of interest in Fabry-Perot interferometry that continues to grow as new applications and techniques are found.

The Fabry-Perot is the simplest of all interferometers, consisting of two partially transmitting mirrors facing each other. Depending on the application, these mirrors may be flat or spherical, and the distance between them can range anywhere from micrometers to meters. All Fabry-Perot designs share some common features, but there are important differences which determine the right choice of interferometer for a particular application.

The author is manager of research and development at Burleigh Instruments, Inc., Fishers NY 14453

How It Works

The Fabry-Perot mirrors form an optical cavity in which successive reflections create multiple beam interference fringes.

The simplest and most versatile design is the flat mirror cavity. As shown in Figure 1, illumination by an extended monochromatic light source produces bright fringes of equal inclination in the focal plane of L_2 , producing a characteristic "bull's-eye" pattern.

At the angle θ where a bright fringe is observed, the relationship between the source wavelength λ and the mirror spacing d is

$$m\lambda = 2nd \cos \theta \quad (1)$$

where n is the refractive index of the medium between the mirrors and m is an integer identifying the order of interference. A pinhole aperture on the optical axis at the focal point of L_2 limits the light transmitted through the pinhole to that passing through the Fabry-Perot parallel

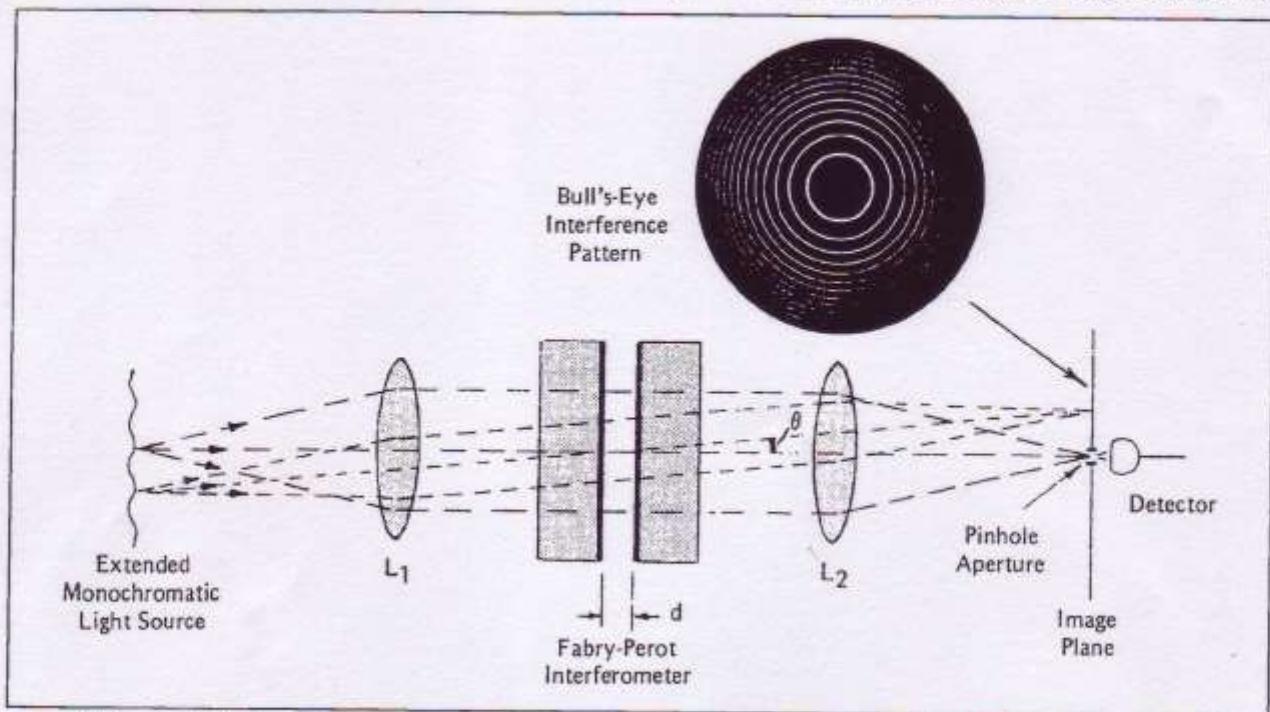


Figure 1. Diagram of Fabry-Perot spectrometer.

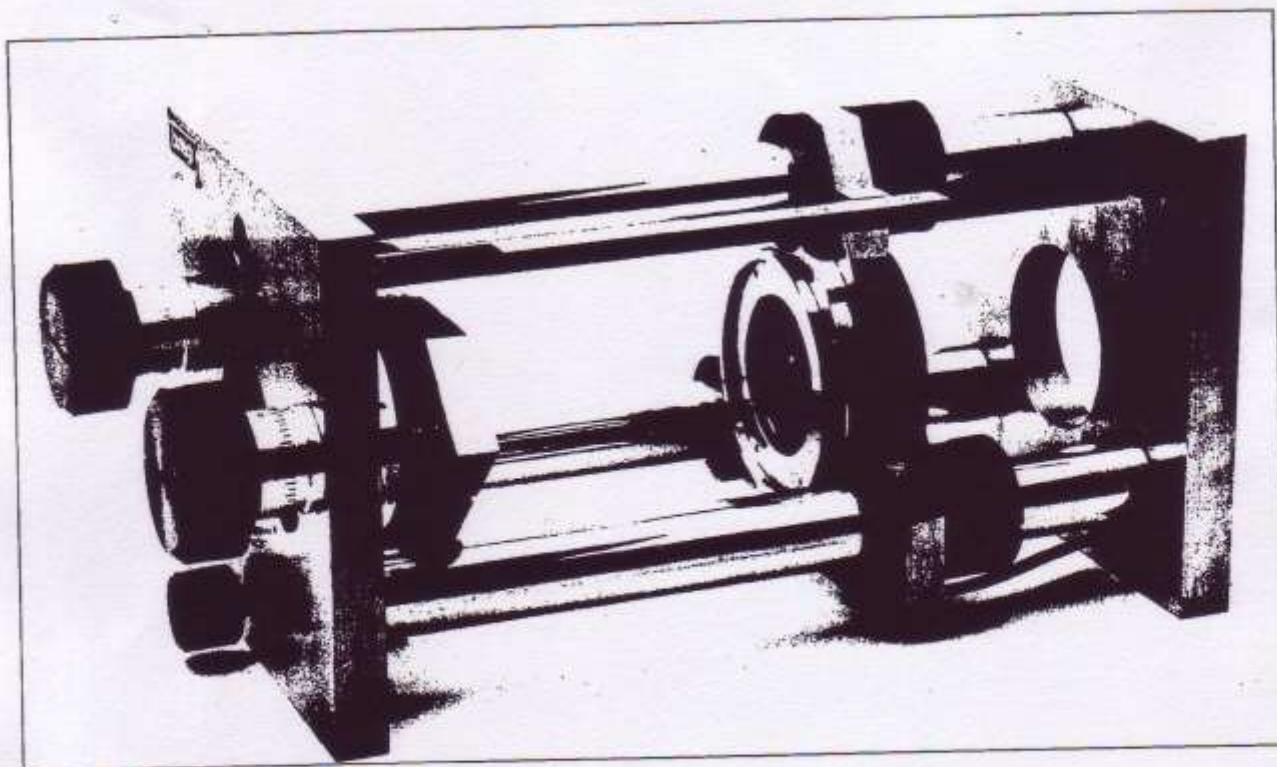


Figure 2. Super-Invar Fabry-Perot interferometer.

to the optical axis ($\theta = 0$), and therefore satisfying the condition

$$m\lambda = 2nd \quad (2)$$

The Fabry-Perot spectrometer so formed may be tuned to transmit any wavelength by varying either n or d .

If the medium between the mirrors is air or some other gas, n can be varied by changing the gas pressure. Such pressure scanning is rarely used now because it is cumbersome and slow. If the medium is a solid, n can be changed by adjusting the temperature, but this too is slow and difficult to control.

Modern interferometers are more often tuned by changing the mirror spacing, d . The optical path length between the mirrors can be altered by rotating the Fabry-Perot interferometer, but rotation results in non-linear tuning and must be limited to small angles or the resolving power of the interferometer is degraded. A more versatile technique for changing d is to mount one mirror on three piezoelectric elements and translate that mirror in a direction perpendicular to its surface while the other remains fixed.

As Equation 2 shows, any wavelength can be transmitted through the interferometer if d changes by at least $\frac{1}{2}\lambda$. For visible wavelengths, it is possible to construct piezoelectric assemblies that will move several wavelengths, providing ample tunability.

A modern Fabry-Perot interferometer with piezoelectric tuning is pictured in Figure 2. The main structure is heavy super-Invar for mechanical rigidity and low thermal sensitivity. The cavity spacing can be set anywhere between 0 and 15 centimeters by adjusting the movable mirror mount. One mirror can be mechanically aligned parallel to the other with the large alignment screws. Once these are set, fine alignment and tuning or

scanning can be performed by remote control of voltages applied to the piezoelectric assembly that supports the opposite mirror.

The Meaning of Finesse

Before discussing further the criteria for choosing a Fabry-Perot interferometer, it is necessary to define some important terms.

A scanning Fabry-Perot spectrometer illuminated with monochromatic light transmits a peak in intensity every time the wavelength satisfies Equation 2. The range of wavelengths that can be displayed in the same spectral order m without overlapping adjacent orders is called the free spectral range (FSR). For a plane mirror Fabry-Perot with spacing d ,

$$\text{FSR} = \frac{1}{2}nd \quad (3)$$

If d is in cm, FSR is in wavenumbers (cm^{-1}).

The resolvable bandwidth or instrumental resolution is the full width at half-maximum of the spectral profile that would be observed from a perfectly monochromatic source. It is defined arbitrarily as

$$\Delta\nu = \text{FSR}/F \quad (4)$$

where F is called the *finesse*, and $\Delta\nu$ is resolvable bandwidth measured in wavenumbers.

Finesse is a measure of the interferometer's ability to resolve closely spaced lines; the higher the finesse the better. Finesse can be thought of as the effective number of interfering beams involved in forming the interference fringes. The factors that limit finesse are those which reduce the strength of the interference as the number of reflections increases. Important examples are mirror reflectivity less than 100% and lack of parallelism or flatness of the mirror surfaces. A separate finesse is associated with each of these factors.

The *reflectivity finesse* for a plane mirror interferometer with mirror reflectivities R is

$$F_R = \frac{\pi\sqrt{R}}{1-R} \quad (5)$$

Typical intensity contours of Fabry-Perot fringes for different mirror reflectivities are shown in Figure 3.

The *flatness finesse* is

$$F_F = M/2 \quad (6)$$

where M is the fractional wavelength deviation from true flatness or parallelism across the mirror aperture. Mirror flatness is commonly specified as λ/M at a standard wavelength of 546 nanometers.

The net finesse due to flatness and reflectivity is called the *instrument finesse*, F_I , where

$$1/F_I^2 = 1/F_R^2 + 1/F_F^2 \quad (7)$$

A plot of F_I is shown in Figure 4 for mirrors with a spherical error amounting to $\lambda/100$ and $\lambda/200$ over their aperture.

When the Fabry-Perot interferometer is used in a spectrometer, as shown in Figure 1, the *pinhole size* determines the degree of collimation of light passing through the interferometer that reaches the detector. If the pinhole is too large, rays passing through the Fabry-Perot at different angles are accepted, thus broadening the instrumental linewidth. The associated *pinhole finesse* is

$$F_p = \frac{4\lambda f^2}{D^2 d} \quad (8)$$

where D is the pinhole diameter and f is the focal length of lens L_2 . To compute the total instrumental finesse of a Fabry-Perot spectrometer, the contribution from F_p should be included with F_R and F_F :

$$\frac{1}{F_I^2} = \frac{1}{F_R^2} + \frac{1}{F_F^2} + \frac{1}{F_p^2} \quad (9)$$

Throughput and Étendue

An advantage of Fabry-Perot interferometers over other types of high resolution spectrometers is their efficiency, both in transmission and "étendue," or light-gathering power. For small apertures or perfectly flat and parallel mirrors, the transmission on the peak of a fringe,

$$T_{\max} = \left(1 - \frac{A}{1-R}\right)^2 \quad (10)$$

depends on A , the scattering and absorption loss at the mirrors. For modern multilayer dielectric mirrors $A \leq 0.2\%$. Consequently, mirror reflectivities as high as 98% can yield throughput close to 80% over a small aperture. The étendue for a plane Fabry-Perot interferometer is

$$U = \Omega \cdot A_m = \frac{\pi D^2 \lambda}{4 d F_I} \quad (11)$$

All the radiation at wavelength λ within a solid angle Ω subtended at a mirror aperture A_m can be transmitted in the bandpass defined by the instrumental finesse F_I .

The above formulae apply to Fabry-Perot interferometers using plane mirrors. Similar formulae exist for spherical mirror interferometers.² The most common interferometer of this type is the confocal design, where identical concave mirrors are spaced by precisely their radius of curvature. For this case the free spectral range $1/4nd$, or half of a plane-mirror system.

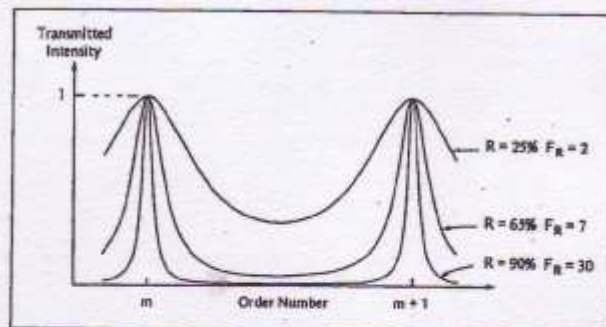


Figure 3. Fabry-Perot transmission for different mirror reflectivities.

Choosing the Right Fabry-Perot

The best Fabry-Perot interferometer for a particular application depends on many factors, including size, stability, tunability, free spectral range, resolution, light-gathering power, and price. Distinguishing features of the various types of Fabry-Perot systems are outlined below. (Note: The word "etalon" is usually used for small Fabry-Perots that might serve as wavelength-selective filters inside the laser cavity. The following discussion uses the terms etalon and interferometer according to common practice; for some devices they are practically interchangeable.)

Solid etalons and *fixed-air-gap etalons* are stable and compact, making them ideal for wavelength filtering, frequency calibration, coherence extension, and intracavity mode selection in lasers. Solid etalons are made from a piece of optically homogeneous material such as fused quartz. Opposite faces are polished flat and parallel, and coated to any desired reflectivity. In a *fixed-air-gap etalon*, two mirrors are bonded to a solid spacer element.

Both types are highly stable mechanically, but solid etalons are more sensitive to temperature changes. A solid etalon is best used in a thermally controlled housing where it can be temperature-tuned or stabilized. Fixed-air-gap etalons are more stable thermally and, unlike solid etalons, they can be pressure-tuned. Both types allow no mechanical variability in spacing; the right spacing must be preselected for a specific application.

The simplest way to tune either etalon is by tilting. This is a good technique provided tilt angles are not so large as to degrade the finesse. These etalons are difficult to manufacture with very flat and parallel surfaces, especially with large mirror spacings. They are best suited for optical systems with small-diameter laserbeams.

Variable-spacing air-gap etalons are similar to fixed-air-gap etalons, except the spacing is established by a mechanically adjustable frame in which the etalon plates are mounted. While adjustable mirror spacing is an advantage, this design is less stable—both mechanically and thermally—than the bonded etalons. Applications are similar.

Piezoelectric mirror control is available for both fixed-air-gap and variable-spacing etalons. In the former the piezoelectric elements are carefully matched in length and cemented directly to Fabry-Perot mirrors. The latter consists of a housing with a built-in piezoelec-

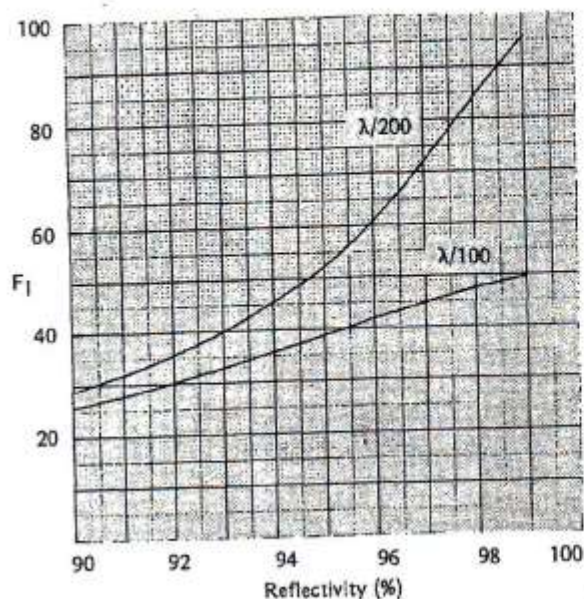


Figure 4. Finesse versus reflectivity for different plate flatnesses.

tric assembly that supports the Fabry-Perot mirrors. Some mechanical means of adjusting the mirror spacing and aligning the mirrors is provided although it is generally less manageable than large-scale designs. In many cases, this difficulty in initial alignment is not important because once the adjustment is set the range of piezoelectric control is sufficient to subsequently optimize the interferometer mirror alignment.

The small size and simple integrity of piezoelectric etalons enhances thermal and mechanical stability. Because these etalons are electronically tunable they can be used with active stabilization systems. Fixed-air-gap etalons with piezoelectric control have been built with capacitance displacement transducers that can be used for automatic alignment and cavity stabilization.³

Applications for piezoelectrically tunable etalons include spectral analysis, laser tuning, active optical filtering, and spectroscopy—all examples where it's not essential to have large spacing with full cavity adjustment, high finesse, or high étendue.

Confocal etalons have two identical concave mirrors spaced precisely at their common radius of curvature. Each mirror images the other back upon itself so that any paraxial ray entering the interferometer is superimposed upon itself after four reflections, resulting in a very high étendue. Because the mirrors are spherical, the requirement for parallel alignment is greatly reduced and only axial piezoelectric tuning is necessary. A typical confocal interferometer has cavity spacing of 50 cm and can resolve 1 megahertz.

Confocal interferometers are commonly called spectrum analyzers when used for laser mode analysis. Because mirror alignment is not critical, they are easier to temperature stabilize than other high resolution Fabry-Perot interferometers. Thus, they are often used as passive reference cavities to stabilize laser frequency and to calibrate frequency of tunable lasers. The high étendue also offers an advantage for high resolution spectroscopy of diffused light sources.

Large-frame Fabry-Perot interferometers are useful in spectroscopy and other research where the highest performance is desired. A large-frame design such as that shown in Figure 2 combines a rigid, thermally stable mechanical structure with a full mirror spacing adjustment and mirror alignment capability not found in small instruments.

The greatest advantage of the large frame Fabry-Perot is the light gathering power or étendue provided by the large mirror aperture. Large mirrors, however, are only feasible if they can be supported without distortion so that the instrument finesse is not degraded by reduced surface flatness. A technique developed at Burleigh Instruments uses three Invar tabs cemented to the rim of each mirror (Figure 5). Glass balls cemented in these tabs align with three V-pads in the mirror cell and are secured by a spring ring that circles the mirror substrate. This kinematic suspension allows the mirror to self-locate so that any stress or torsional force produced by the spring ring is relieved by rotation of the ball in the V-block, and does not warp the mirror surface. Mirrors as large as 70 mm in diameter are routinely mounted this way without altering their surface figure. These mirrors attach to the fixed and piezoelectrically driven mirror mounts. The mounting permits easy mirror changes as necessary.

The piezoelectric assembly provides sufficient alignment and scanning control so that, once mechanically aligned, the instrument can be thermally isolated in an insulated box and operated completely by remote control. This is particularly advantageous for stability as the lab temperature fluctuates. In extreme environments active temperature control may be added inside the thermal box. Experiments that require long periods of stable operation would benefit from an electronic stabilization system that actively corrects for spacing and alignment.

Mirrors and Coatings

With the exception of mirrors used in the far-infrared, most Fabry-Perot mirrors are made of a high-quality fused silica such as Spectrosil B. Plane mirror substrates are wedged at an angle of about 10 arc minutes to prevent secondary interference fringes generated by the back surfaces of the mirrors. Also, the back surfaces are antireflection coated to reduce reflections and to increase throughput.

High-quality, low-loss multilayer dielectric coatings are available from the ultraviolet to the infrared. These so-called "soft coatings" give good spectral coverage (typically with pass-bands 100 nm or more in the visible) with losses less than 0.2% and minimal flatness error. Broader-band coatings are available, but they require a greater number of dielectric layers that may introduce flatness errors ($\sim \lambda/100$) and higher absorption losses (0.3% to 0.4%). Also available are "hard coatings," which are applied hot and may warp the mirror substrates, so are not advised for Fabry-Perot mirrors unless necessary for resistance to high-power laserbeams.

Ramp Generators

Piezoelectric tuning of an interferometer requires a special electronic controller. Its function is to sweep the

mirror spacing in a repetitive scan by applying an adjustable ramp voltage to the piezoelectric elements, so it is often called a "ramp generator." Modern Fabry-Perot ramp generators include many additional features. A common bias allows manual tuning of the mirror spacing, while other bias controls permit changing the voltage on individual piezoelectric elements to tilt the movable mirror. These controls also make it possible to interface automatic cavity and alignment stabilization systems.

Generally, the elements in a piezoelectric assembly are not identical but have slightly different voltage sensitivities. As a result, the mirror supported by that assembly will tilt as it is translated. Tilt-free translation can be restored by "trim controls" on the ramp generator that adjust the ratio of ramp voltages applied to the separate piezoelectric elements.

Piezoelectric materials do not extend perfectly linearly with applied voltage. One way to linearize the motion is to produce a nonlinear voltage ramp that counteracts the piezoelectric nonlinearity. In Burleigh ramp generators this feature improves scan linearity tenfold.

Fabry-Perot Systems

The Fabry-Perot interferometer is actually an optical filter, passing some frequencies and rejecting others. When tuned to transmit one frequency of light, the greatest rejection occurs for frequencies that are displaced by one half of the free spectral range. The ratio of maximum transmission to maximum rejection contrast is related to the finesse as shown by the transmission profiles in Figure 3. A reflectivity of 93% will typically produce a finesse of 40 and a contrast of 600.

For some applications a much higher contrast ratio or larger free spectral range is necessary. For this purpose, combinations of interferometers that constitute Fabry-Perot systems have been devised.

Just as with other identical filters, when two or more Fabry-Perot interferometers are placed in series the transmission functions multiply to improve both resolution and contrast. In practice, it is much easier, more stable, and less expensive to pass the light beam through different sections of the same interferometer several times. A simple three-pass configuration is shown in Figure 6.

Extremely high contrast can be obtained in this way. Theoretically, a Fabry-Perot with 93% reflectivity mirrors can have a contrast of $\sim 10^8$ in three-pass operation, $\sim 10^{14}$ in five-pass operation. Although other factors, such as stray reflections and mirror flatness, limit the ultimate contrast, performance approaching theoretical can be obtained with careful design.

Multipassing was made practical and popularized by the application of corner cube retroreflectors.⁴ Corner cube retroreflectors displace the reflected beams laterally, greatly simplifying the separation of input beams. They also have the all-important feature of producing a reflected beam accurately parallel to the input beam even if the corner cube is tilted. This feature greatly simplifies

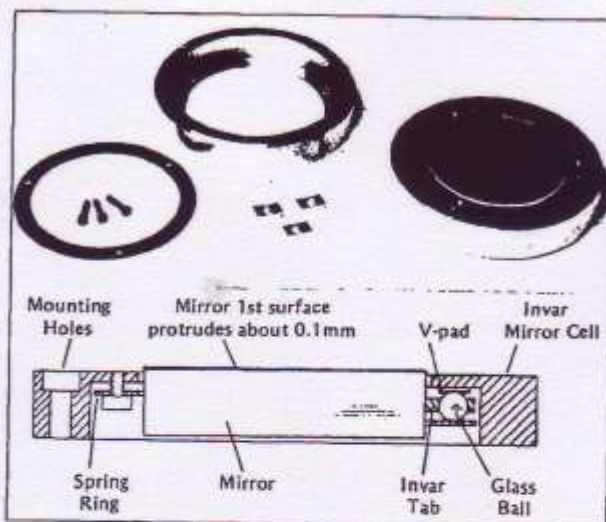


Figure 5. Distortion-free technique for mounting mirrors in a large-frame Fabry-Perot.

the optical alignment so that only the Fabry-Perot mirror alignment remains critical.

Figure 7 shows a scheme utilizing modified corner cube retroreflectors for five-pass operation of a Fabry-Perot interferometer. Individual beams are well-separated on the mirror surfaces so that cross-transmission between beam paths due to stray reflections and scattering can be minimized by inserting light baffles.

Multipass operation of Fabry-Perot interferometers is now widely used, especially for experiments involving spectral analysis of light scattered from surfaces, thin films or opaque materials. Throughput of a properly designed multipass system is very good. With 93% reflectivity mirrors, the actual throughput compared to single pass with the same entrance aperture is approximately 50% for three-pass and 30% for five-pass.

Mirror flatness is very important for good multipass operation so that the mirror spacing can be made identical for all passes; therefore, only large frame Fabry-Perot interferometers with distortion-free mirror suspensions are recommended. Special retroreflector assemblies for three-pass or five-pass operation are commercially available.⁵

The use of two or more interferometers in tandem to alleviate the problems of overlapping spectral orders has often been proposed. One scheme simply utilizes a low-resolution Fabry-Perot interferometer with a fixed spacing to prefilter a portion of the spectrum followed by a high resolution scanning interferometer with free spectral range equal to or greater than the bandwidth of the prefilter. The transmission profile is that of the high resolution interferometer with a throughput modified by the prefilter that serves to reject adjacent spectral orders. Often an interference filter is added to such a system to provide complete blockage of unwanted spectral orders beyond the free spectral range of the prefilter interferometer.

Another way to eliminate overlapping spectral orders is to increase the free spectral range. This is possible without reducing the resolving power by using two interferometers in tandem with slightly different

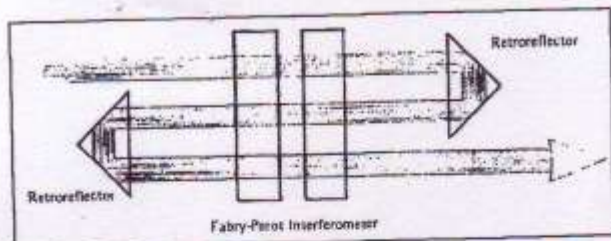


Figure 6. Triple-pass Fabry-Perot interferometer.

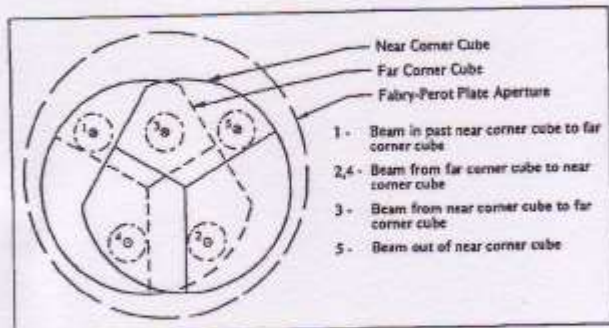


Figure 7. Retroreflector design for a five-pass interferometer.

mirror spacings. When each is tuned to transmit a particular frequency the effective free spectral range of the pair is increased because adjacent orders of one interferometer do not coincide in frequency with those of the other. The major difficulty in using such a tandem system is maintaining the two interferometers frequency-locked to each other and scanning both synchronously. A special mechanical design⁶ allows two interferometers to be scanned simultaneously by mounting one mirror of each on a common piezoelectrically driven mount. The interferometers are set at an angle related to the ratio of the interferometer mirror spacings to achieve synchronous frequency scanning. Two separate Fabry-Perot interferometers of different mirror spacing can also be operated in synchronous fashion using electronic stabilization circuitry that couples them by referencing the scan of both instruments to the laser line frequency.

Tandem operation of piezoelectrically scanned interferometers is not difficult when certain simple optical alignment procedures are followed.⁷ Synchronous frequency scanning is achieved by driving the two interferometers with simultaneous ramp voltages proportional to their respective mirror spacings.

Stabilization Techniques

Often, the passive thermal stability of a well-designed Fabry-Perot interferometer is not enough. These situations include collection of weak spectra where data accumulation over long periods is necessary; multipass operation where mirror alignment is critical; and tandem operation where accurate correlation in frequency scanning must be maintained. Such cases call for some form of active stabilization.

One technique uses capacitance displacement transducers on the circumference of the Fabry-Perot mirrors to monitor changes in spacing or alignment from a preset position.³ Extremely stable and reliable instruments have been built using this technique; they are particularly suited for observational astronomy where no prominent spectral features are available for optical stabilization.

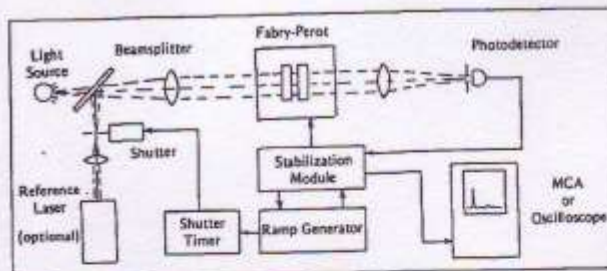


Figure 8. Stabilized Fabry-Perot spectrometer.

The one drawback to capacitance transducers is that their limited displacement range (typically 100 micrometers) precludes changing the mirror spacing once a particular set of transducer elements has been attached to the mirrors.

The most versatile technique for active Fabry-Perot stabilization is one that makes use of the light transmitted through the interferometer to control the cavity spacing and optimize the mirror alignment. A prominent spectral feature, such as the laser line in a light scattering experiment, is chosen as a reference frequency for cavity and alignment stabilization. During setup this feature is centered at some designated position in the frequency scan. By monitoring the relative intensity in two "windows" on either side of this position, any drift of the interferometer relative to the reference frequency can be detected and corrected through the cavity bias control on the ramp generator. Parallel mirror alignment can be optimized by applying tiny angular changes to the piezoelectrically driven mirror on successive scans and detecting the resultant change in intensity of the reference peak. After each test a correction is applied to the alignment bias voltages on the ramp generator in the direction that produced the greater throughput.

The main advantage of the optical stabilization technique is that it may be used with any piezoelectrically controlled Fabry-Perot system because it makes use of the transmitted signal rather than relying on separate transducers. In effect, it continually corrects for cavity and alignment drift the same way one would do manually, so that any system that can be aligned can be maintained in alignment with this technique. If an appropriate reference frequency does not exist in the observed spectrum, one can be introduced as shown in Figure 8. Since the reference frequency is only used for a small fraction of the scan, it may be blocked by a shutter the rest of the time if it would otherwise interfere with the collection of spectral intensity from the light source. ●

References

1. C. Fabry and A. Perot, *Ann. Chem. Phys.* **16**, 115, 1899.
2. M. Hercher, *Appl. Opt.* **7**, 951, 1968.
3. T.R. Hicks, N.K. Reay, and R.J. Scaddan, *J. Phys. E: Sci. Instrum.* **7**, 27, 1974.
4. J.R. Sandercock, in *Light Scattering in Solids*, M. Balkanski, Ed., Flammarion Press, Paris, 1971 p. 9.
5. For further details consult Burleigh Instruments Tech Memo entitled "Multipass Fabry-Perot."
6. J.R. Sandercock, U.S. Patent #4225236, assigned to RCA Corp., 1980.
7. J.G. Dil, N.C.J.A. van Hijningen, F. van Dorst, and R.M. Aarts, *Appl. Opt.* **20**, 1374, 1981.

The Spherical Mirror Fabry-Perot Interferometer

Michael Hercher

The theory, design, and use of the confocal spherical mirror Fabry-Perot interferometer (FPS) is described in detail. Topics covered include performance of an FPS for small departures from the confocal mirror separation, optimization of the (resolution) \times (light gathering power) product, factors limiting realizable finesse, mode matching considerations, alignment procedures, and general design considerations. Two specific instruments are described. One is a versatile spectrum analyzer with piezo-electric scanning; the other is a highly stable etalon with fixed spacing. Examples of the performance of these instruments are given.

I. Introduction

The spherical mirror Fabry-Perot interferometer (FPS) was first described by Connes over ten years ago.¹⁻³ Although this instrument is mentioned in some recent texts,^{4,5} Connes' papers contain the only detailed descriptions of the spherical mirror Fabry-Perot interferometer. This paper is intended to review and extend Connes' treatments of the theory of operation of the FPS, to describe specific instrument designs, and to outline practical procedures for using this instrument in both static and scanning modes. I have drawn freely from the results obtained by Connes, particularly those contained in Ref. 2. In those cases where our results differ, it is generally because I consider only relatively high reflection mirrors with uniform transmission, whereas Connes described interferometers in which the mirrors had zero transmission (and nearly complete reflection) over half of their apertures.

Following the introduction of curved mirror resonators as laser cavities, it was found that with little modification they could effectively be used as spectrum analyzers. Fork *et al.* have analyzed spherical mirror interferometers in general terms, and have demonstrated the extraordinarily high resolutions that can be obtained, particularly when the interferometer has optical gain as in a subthreshold laser.⁶ While they recognized that confocal resonators (or spherical mirror Fabry-Perot interferometers—the two terms are interchangeable) offer certain distinct advantages over nonconfocal arrangements, the tendency to date has been to use nonconfocal cavities for high spectral resolution with laser light sources. The advantages of a non-

confocal arrangement are (a) the relatively loose tolerance on the mirror separation, and (b) the ability to select various free spectral ranges with a given pair of mirrors. Its disadvantages are (a) the necessity to match the input radiation field to a transverse mode of the cavity, and (b) the relatively low light gathering power of the resonator with spatially incoherent sources. The FPS, on the other hand, requires a relatively precise control of the mirror separation with a resulting fixed free spectral range. This disadvantage is largely offset by the high light gathering power of the FPS (even at very high resolution), freedom from mode matching considerations, and the capability of the instrument to be used to display spectral information in the form of a multiple beam interference fringe pattern. The FPS is clearly superior to a nonconfocal resonator for use with spatially incoherent sources and with fast pulsed light sources. It is also very much easier to use with cw laser sources and permits the spectral analysis of lasers operating in a number of different transverse modes.

Section II deals with the theory of the FPS and includes subsections on the localized fringe pattern, spectral resolution and instrument profile with finite apertures, light gathering power, and mode matching considerations.

Section III contains descriptions of prototype scanning and static FPS spectrum analyzers and practical procedures for their optimum use. We have been able to achieve finesses well in excess of 150 with both 5-cm and 10-cm mirror spacings: both instruments are thermally compensated and mechanically stable, and the 5-cm FPS incorporates a piezoelectric scanning device which permits its use in either a static or rapid scan mode.

Table I lists the symbols used.

The author is with the Institute of Optics, University of Rochester, Rochester, New York 14627.

Received 2 January 1968.

This work supported in part by the Air Force Cambridge Research Laboratories.

Table I. List of Symbols

A	=	area of FPS entrance aperture
c	=	velocity of light
d	=	FPP mirror separation
D	=	aperture diameter (FPS or FPP)
F	=	finesse = $(\pi R)/(1 - R^2)$, (FPS)
L	=	cavity loss per transit
M	=	fringe pattern magnification factor
r	=	FPS mirror radii and confocal separation
R	=	mirror reflectivity
\mathcal{R}	=	spectral resolving power
T	=	mirror transmission
T_0	=	FPS instrumental transmission
U	=	étendue = ΩA
δ	=	phase increment = $2\pi\Delta/\lambda$
Δ	=	path difference
ϵ	=	difference between FPS mirror separation and confocal spacing r .
λ	=	wavelength
ν	=	optical frequency
$\Delta\nu_m$	=	minimum resolvable frequency difference, or instrumental bandpass.
$\Delta\nu_f$	=	free spectral range, $c/4r$ (FPS)
ρ	=	fringe radius
ρ_s	=	radius of central spot = $(\lambda r^2/F)^{1/2}$
Ω	=	solid angle subtended by source

II. Theory of Operation

A. Interference Fringes

A spherical mirror Fabry-Perot interferometer is comprised of two identical spherical mirrors separated by a distance very nearly equal to their common radius of curvature. When light from a source lying close to the axis is incident on the FPS, a multiple beam interference pattern is produced in the vicinity of the central plane of the interferometer. To see how this interference pattern arises, consider an entering ray which intersects the two mirrors at points P_1 and P_2 , which are located at distances ρ_1 and ρ_2 from the axis. As shown in Fig. 1, θ is the skew angle of the entering ray. According to paraxial optics, each mirror serves to image the other mirror back upon itself, so that a paraxial ray is reentrant, i.e., falls back upon itself, after traversing the interferometer four times [Fig. 2(a)]. Owing to aberration, however, a general ray is not reentrant but follows a path such as that shown in Fig. 2(b). Even though it is not reentrant, if the incident ray is not at too great an angle to the axis, it will continue to intersect itself in the vicinity of a point P , located in the central plane of the FPS at a distance ρ from the axis. The position of the points at which rays continue to intersect themselves determines the position of the fringe pattern. If the axial mirror spacing is precisely r , the mirror radius, it is straightforward to show that the four-transit path, i.e., the path taken between successive intersections at the point P , exceeds the paraxial path $4r$ by an amount:

$$\Delta_0 = \rho_1^2 \rho_2^2 \cos 2\theta / r^3 + \text{higher order terms.} \quad (1)$$

More generally, if the mirror spacing is $(r + \epsilon)$, the four-transit ray path exceeds the corresponding paraxial ray path $4(r + \epsilon)$ by an amount:

$$\Delta = \rho_1^2 \rho_2^2 \cos 2\theta / r^3 + 2\epsilon(\rho_1^2 + \rho_2^2) / r + \text{higher order terms.} \quad (2)$$

If we now restrict our attention to a small and distant source, close to the axis of the interferometer, we may write for Eq. (2):

$$\Delta(\rho) \approx \rho^4 / r^3 + 4\epsilon \rho^2 / r^2, \quad (3)$$

where ρ is the height at which an entering ray crosses the central plane of the FPS. Referring to Fig. 2(b) we see that for each entering ray there are two sets of transmitted rays: those which have been reflected $4m$ times (type 1), and those which have been reflected $(4m + 2)$ times (type 2), where m is an integer. The interference

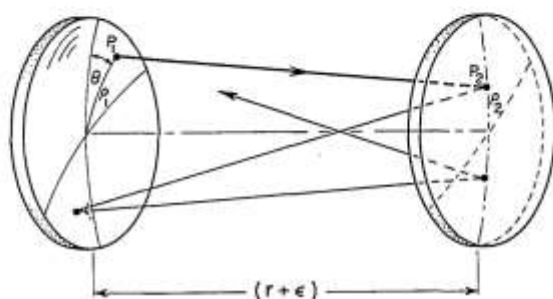


Fig. 1. General ray path in a spherical mirror Fabry-Perot interferometer.

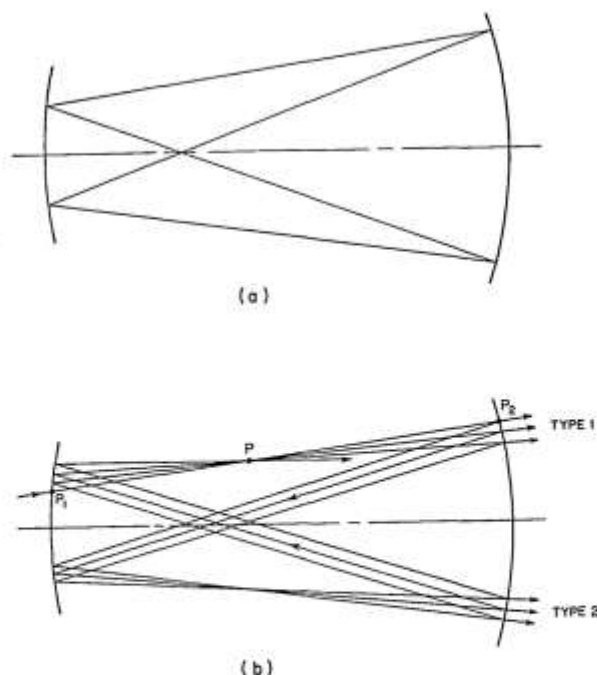


Fig. 2. (a) Ray path in an FPS in the paraxial approximation (reentrant rays), (b) aberrated ray path, showing intersection of rays at point P .

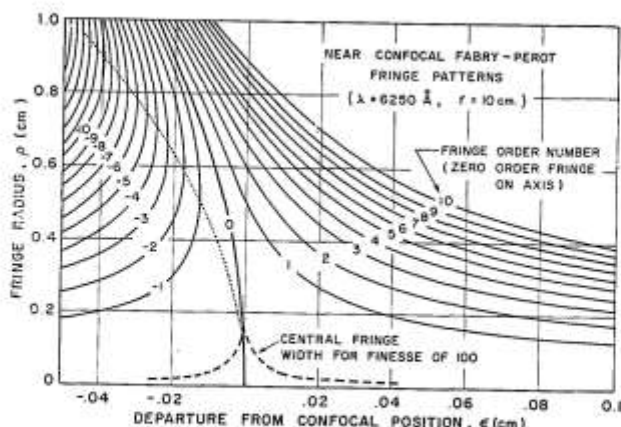


Fig. 3. Near confocal FPS fringe patterns. At each value of ϵ , the solid curves give the radii of the circular interference fringes for the case of a monochromatic source and a bright fringe on axis. The dashed line shows the spot size radius ρ_s for a finesse of 100, and the dotted line defines the zone of best focus as a function of ϵ . (Appendix I shows how to change the scales for different wavelengths and mirror separations.)

patterns produced in the central plane of the interferometer are described by:

Type 1:

$$I_1(\rho, \lambda) = I_0 [T / (1 - R^2)]^2 \{ 1 + [2R / (1 - R^2)]^2 \times \sin^2[\delta(\rho, \lambda) / 2] \}^{-1} \quad (4a)$$

or,

Type 2:

$$I_2(\rho, \lambda) = R^2 I_1(\rho, \lambda) \quad (4b)$$

where,

$$\delta(\rho, \lambda) = (2\pi/\lambda)[\Delta(\rho) + 4(r + \epsilon)]. \quad (5)$$

(See Table I for a list of symbols.) The derivation of these equations exactly follows the usual derivation for a plane mirror Fabry-Perot interferometer (FPP). When the mirror reflectivity R is close to unity, the interference patterns for both types of rays are the same and are superposed. When the two types of ray leave the interferometer at a small angle, e.g., if the entering beam is approximately collimated but at an angle to the axis, they will form an additional interference pattern made up of equally spaced straight fringes whose separations are determined by the angle at which the two beams are brought to focus. This two-beam, i.e., \sin^2 , interference pattern modulates the multiple beam pattern of circular fringes and, of course, arises only when the two beams are coherent. Examples of this incidental two-beam pattern are shown in Sec. III.

From Eq. (4) we see that bright fringes are formed in the central plane of the interferometer when $\delta(\rho, \lambda)$ satisfies $\delta(\rho, \lambda) = 2m\pi$, or,

$$\rho^2/r^2 + 4\epsilon\rho^2/r^2 = m\lambda, \quad (6)$$

where m is a positive or negative integer giving the order of interference relative to the order on axis (which

is assumed, for convenience, to be an integer). Fringes thus have radii given by:

$$\rho_m = [-2\epsilon r \pm (4\epsilon^2 r^2 + m\lambda r^2)^{1/2}]^{1/2}. \quad (7)$$

For $\epsilon > 0$, ρ_m is single-valued and $m > 0$. When $\epsilon < 0$, ρ_m is two-valued for $m \leq 0$, and single-valued for $m > 0$. Figure 3 shows this fringe pattern in cross section for different values of ϵ with r and λ fixed. (Appendix I shows how to transform this curve, as well as curves in later figures, so that it corresponds to other values of r and/or λ .)

The maximum radial dispersion in the fringe pattern ($d\rho/d\lambda$) is obtained in the vicinity of the fringe corresponding to the lowest order of interference. For any given value of ϵ this fringe occurs at the value of ρ which corresponds to the zone of best focus for the spherical mirror. (By Fermat's principle, this is just the value of ρ where $d\Delta/d\rho$ is an extremum, or $\rho = (-2\epsilon r)^{1/2}$. No zone of best focus is defined for $\epsilon > 0$.)

In the special case (very nearly approximated in most applications) where $\epsilon \approx 0$, the fringes have radii given by:

$$\rho_m = [(m - \xi)\lambda r^2]^{1/2}, \quad (8)$$

where $\xi < 1$ and $[4(r + \epsilon)/\lambda]$ is the exact order of interference on the axis.

It is obvious from Eq. (8) that the radial dispersion in the fringe pattern is markedly nonlinear near the axis when the interferometer is precisely confocal. This is, of course, no real disadvantage and provides the basis for the high étendue of which this type of instrument is capable. If desired, the dispersion may be made more nearly linear by slightly decreasing (or increasing) the mirror separation. This is evident from Fig. 3 and is illustrated in Sec. III.

B. Spectral Resolving Power

In discussing spectral resolving power in this section, we assume that the interferometer is set at the confocal spacing ($|\epsilon| \leq \lambda$) and is used in the scanning mode with a collimated light source. More specifically, we assume that the central fringe pattern is imaged, 1 to 1, onto a plane containing an axial aperture, coincident with the center of the fringe pattern, behind which is located a linear detector. Since the resonant wavelength of the interferometer is a linear function of the mirror spacing, it is possible to obtain a linear plot of the source spectrum simply by recording the output from the detector as a function of the mirror separation. A change of $\lambda/4$ in the mirror separation scans through a free spectral range of $c/[4(r + \epsilon)]$ Hz.

The spectral resolving power \mathcal{R} of a spectroscopic instrument is defined by:

$$\mathcal{R} \equiv \nu/\Delta\nu_m \approx \lambda/\Delta\lambda_m, \quad (9)$$

where $\Delta\nu_m$ is the minimum resolvable frequency increment in the vicinity of a frequency ν . The classical criterion for defining what is meant by *minimum resolvable increment* is an extension of the criterion used by Rayleigh in discussing diffraction pat-

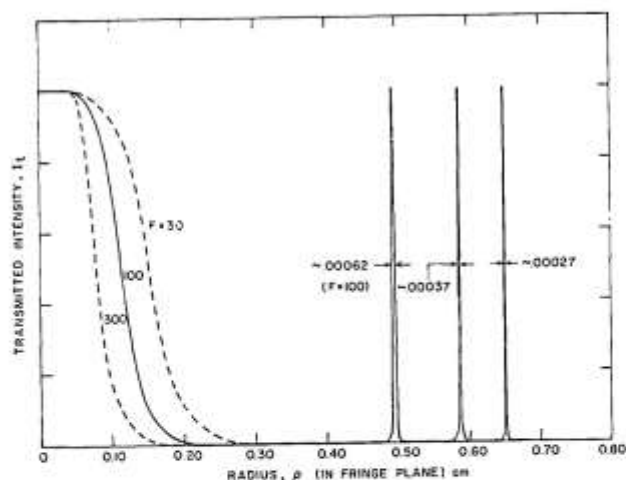


Fig. 4. Calculated distribution of light in an FPS fringe pattern for a monochromatic source and various values for F , the finesse. Note the broad central fringe ($\epsilon = 0$, $r = 10$ cm).

terns. For convenience, we depart from this definition slightly and define the *minimum resolvable frequency increment* as the apparent spectral width (full width at half maximum) of a monochromatic line. This is, of course, just the width of the instrumental profile. In practice, a large number of factors enter into the determination of the instrumental profile of a Fabry-Perot interferometer. These include mirror reflectivity, mirror figure, diffraction losses, and alignment. One of the great advantages of the spherical Fabry-Perot interferometer over its plane parallel counterpart is the relative ease with which reflectivity limited resolution can be realized in practice. Neglecting all but transmission losses at the mirrors, the instrumental profile of an FPS is given by Eq. (4). The resulting value for $\Delta\nu_m$, the width of the instrumental profile, is given by:

$$\Delta\nu_m = c(1 - R^2)/4\pi r R. \quad (10)$$

At this point it is useful to introduce a quantity called the finesse F of the interferometer, which we can define as the ratio of the free spectral range to the instrumental width:

$$F \equiv \Delta\nu_f / \Delta\nu_m. \quad (11)$$

In terms of the finesse F , the instrumental width and spectral resolving power are given by:

$$\Delta\nu_m = c/4rF, \quad (12)$$

and

$$\mathcal{R} = 4rF/\lambda. \quad (13)$$

Also, the expression for the interference pattern can be written as:

$$I(\rho) = \left(\frac{T}{1 - R^2} \right) \frac{I_0}{1 + (2F/\pi)^2 \sin^2(\delta/2)} \quad (14)$$

Here we have simply made the substitution, $F = \pi R/(1 - R^2)$ in Eq. (4). Note that this expression re-

mains valid regardless of whether the finesse is determined by the mirror reflectivity, or by other factors. When the finesse is limited by a mirror reflectivity whose value is close to unity, we have:

$$F_R = \pi R/(1 - R^2) \approx \pi/2(1 - R). \quad (15)$$

The fringe pattern described by Eq. (14) is shown in Fig. 4 for representative values of the finesse.

In order to record the ultimate instrumental profile in the scanning mode of operation, the detector aperture would be vanishingly small and the resulting instrumental profile would be given by:

$$I(\nu - \nu_0) \simeq \{1/T/(1 - R)\}^2 I_0(\nu) \times \left\{ 1 + \left[\frac{2(\nu - \nu_0)F}{c/4r} \right]^2 \right\}^{-1}. \quad (16)$$

If the detector aperture were increased, there would initially be an increase in the amount of light collected from a finite source, with little decrease in resolving power (assuming perfectly spherical mirrors and confocal spacing). As the aperture was opened further, the amount of light collected would increase less rapidly and the resolving power would begin to decrease—becoming approximately 70% of the resolving power given by Eq. (16) when the radius of the detector aperture attained a value ρ_s given by:

$$\rho_s = (r^2\lambda/F)^{1/2}. \quad (17)$$

We will refer to ρ_s as the *spot size* or *spot radius*; ρ_s is simply the radius of the mirror zone whose resonant frequency is displaced from the axial resonance by an

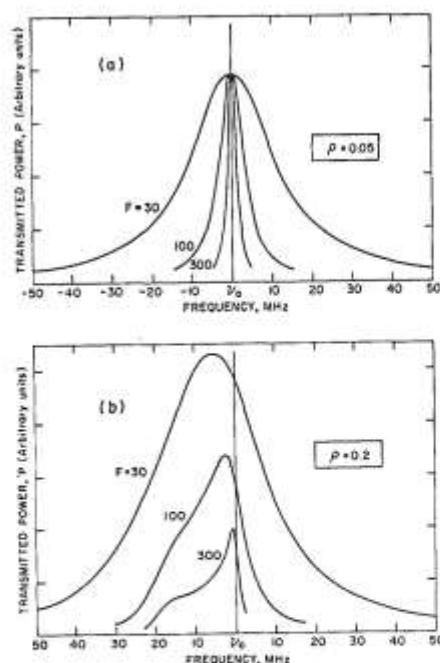


Fig. 5. Calculated FPS instrumental profiles for two different detector aperture radii. These correspond to the spectra which would be recorded using a monochromatic source in the scanning mode of operation ($\epsilon = 0$, $r = 10$ cm). (a) $\rho = 0.05$, (b) $\rho = 0.2$.

amount equal to the minimum resolvable frequency increment $\Delta\nu_m$. The actual instrumental profile that is obtained when using a finite detector aperture is given by:

$$I_\nu(\nu - \nu_0) = 2\pi \int_0^\rho I(\xi) x dx, \quad (18)$$

where

$$\xi = [\nu - \nu_0(1 + x^2/4r^2)]$$

and

$$I(\xi) = \frac{1}{4} \{ (T/(1-R))^2 I_0 \{ 1 + (2F/\pi)^2 \sin^{-2}[\pi\xi/(c/4r)] \} \}^{-1},$$

and where ν_0 is the frequency that would be recorded using a vanishingly small aperture. Note that with a finite aperture, the instrumental profile is no longer centered on ν_0 and is asymmetric. Figure 5 shows computed instrumental profiles for various values of F and ρ , the aperture radius (cf., Fig. 14 in Sec. III).

Other Factors Affecting Instrumental Finesse

We have seen [Eq. (15)] that in the absence of other losses, the instrumental finesse is limited by the reflectivity of the mirrors to a value of approximately $\pi/[2(1-R)]$. In this section we consider the manner in which the finesse is degraded by other factors, namely, irregularities in the surfaces of the mirrors, and diffraction. If we wish, we can associate with each loss mechanism, e.g., mirror transmission or diffraction, a contribution to the lifetime of the resonant cavity. The finesse F_i associated with the i th loss mechanism, is related to the corresponding contribution to the cavity lifetime τ_i by:

$$F_i = \pi c \tau_i / 2r. \quad (19)$$

Hence it is clear that the net instrumental finesse F is related to the individual contributions F_i by:

$$F^{-1} = \sum_i (F_i)^{-1}, \quad (20)$$

so that it is useful and meaningful to consider the individual contributions to the finesse independently.

First we consider the effect of irregularities in the figure of the mirror on the finesse. Without knowledge of the specific nature of these irregularities, it is impossible to be precise in predicting their effect on the finesse. Generally, however, if the mirrors have a *smooth** irregularity on the order of λ/m across the aperture being used, then the figure-limited finesse F_f will be approximately:

$$F_f \approx m/2. \quad (21)$$

Obviously, by reducing the aperture (or diameter of the incident light beam) it is possible to minimize the reduction in instrumental finesse due to plate irregularities. This is indeed a practical expedient in the case of

a spherical Fabry-Perot etalon; in the case of a plane mirror Fabry-Perot etalon, however, the significantly increased diffraction losses that accompany the reduction of the etalon aperture set a limit to the improvement in finesse that can be realized by this technique. Note also that in the case of the plane mirror Fabry-Perot, an angular misalignment of the plates is equivalent to a corresponding plate imperfection. For the spherical Fabry-Perot, this is not the case: an angular misalignment merely redefines the optical axis of the system. With regard to plate irregularities, it is worthwhile pointing out another contrast between the plate-mirror and spherical-mirror etalons. If the mirrors of an FPP have irregularities on the order of $\lambda/2$, the resultant pattern at infinity will be completely washed out. However, since the fringe pattern obtained with an FPS is localized relatively close to the surfaces of the mirrors, a similar mirror figure irregularity will *not* wash out the fringe pattern, but will instead distort it so that the fringes are no longer circular. (These distorted fringes tend to define contours of equal path difference.)

As implied above, diffraction losses are much less in the case of a spherical Fabry-Perot etalon than for its plane mirror counterpart. The rigorous justification of this statement lies in the analytical treatment of confocal resonators given by Boyd and Gordon,⁷ in which they show that for any case of practical interest to us, i.e., those cases where $D^2/4r \gg \lambda$, D being the diameter of the mirror aperture, the diffraction losses for a confocal resonator are orders of magnitude less than for the corresponding plane parallel resonator. The calculation of the exact diffraction loss in a confocal resonator requires a fairly complex analysis in which the incoming radiation field is decomposed into eigenmodes of the cavity, each of which has a different diffraction loss. Absolute minimization of the diffraction losses requires proper mode matching (see Sec. II.D). In this case, when the incoming radiation field has a curvature and amplitude distribution identical to that of the lowest order transverse mode of the confocal resonator, the diffraction loss per pass L_D is approximately given by⁷:

$$L_D \approx 10^{-[5(\rho_0^2/\lambda) + 1]} \quad (22)$$

where ρ_0 is the radius of the mirror aperture. In any case of practical interest, diffraction losses are completely negligible in comparison to other losses, so that diffraction plays no significant role in determining the over-all finesse. For a plane parallel Fabry-Perot etalon, the diffraction limited finesse is approximately given by:

$$F_D(\text{FPP}) \approx D^2/2\lambda d, \quad (23)$$

where d is the separation of the plane mirrors and D is the aperture diameter.

Other types of loss, such as scattering at the mirror surface (which is, of course, taken into account in F_R), can be treated separately very easily. If a small fraction L of the radiation incident on the mirror (or making a transit of the resonator) is lost, then by analogy to

* If the irregularity is not smooth, the loss incurred is more appropriately treated as a scattering loss.

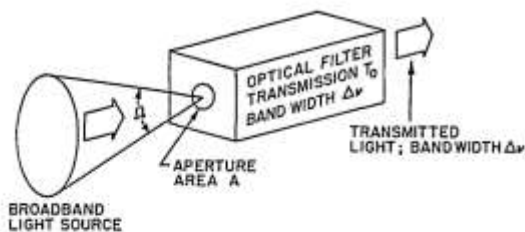


Fig. 6. Generalized picture of a spectrometer or monochrometer.

Eq. (15), the corresponding contribution to the finesse is given by:

$$F_L \sim \pi/2L. \quad (24)$$

To summarize the implications of this section, we can say that for a spherical Fabry-Perot interferometer, in confocal adjustment, the significant factors in determining the finesse and resolving power are the reflectivity of the mirrors and their surface figure. This is in contrast to the case of a plane parallel Fabry-Perot, where diffraction and alignment can make significant contributions to the degradation of finesse and resolving power.

C. Light Gathering Power

1. Introduction

One of the major factors to consider in evaluating any spectrometer is its ability to effectively gather light from an incoherent extended source, filter it with the instrumental bandpass, and transmit it to some radiation detector. In general, the situation can be represented by Fig. 6. Here, the spectrometer is depicted as a bandpass filter: all of the radiation emanating from within a solid angle Ω subtended at an aperture of area A , can be transmitted within the bandpass $\Delta\nu_m$ of the spectrometer. If the transmission of the spectrometer at the center of the bandpass is T_0 and the spectral radiance of the source is N_ν , then the radiant power per unit bandwidth P_ν , transmitted by the spectrometer is given by:

$$P_\nu = N_\nu A \Omega T_0. \quad (25)$$

The product ΩA has come to be known as étendue U of the spectrometer. Thus the easily remembered expression:

$$P = N U T_0. \quad (26)$$

Of course, if the light source under investigation is a laser, it is obvious that most of the emitted power can be put into a beam with a small cross-sectional area and a small divergence. In this case, the étendue of the spectrometer provides a measure of the *alignment tolerance* between the laser beam and spectrometer, rather than being a measure of the spectrometer's light gathering power.

2. Transmission and Étendue of a Spherical Fabry-Perot Interferometer

In Sec. II.A it was pointed out that a single beam of light incident on an FPS gives rise to two transmitted beams, which are generally at a small angle to one another. When both of these transmitted beams are taken into account, the net transmission T_0 at the center of the instrument profile is found from Eq. (4a) and (4b):

$$T_0 = (1 + R^2)(T/[1 - R^2])^2 \approx \frac{1}{2}[T/(1 - R)]^2, \text{ for } R \approx 1. \quad (27)$$

(When the two transmitted beams are precisely aligned, the situation is somewhat different, as discussed in Sec. II.D.) If we define A to be the sum of the absorption and scattering at the mirrors, then $(1 - R) = (T + A)$, so that the peak transmission may be written as:

$$T_0 \approx \frac{1}{2}[1 + (A/T)]^{-2} \quad (28)$$

This function is plotted in Fig. 7, which clearly illustrates the drastic loss in net transmission whenever the absorption-plus-scattering losses become comparable with, or exceed, the transmission loss at the mirror. As a rule, very high reflectivities can be attained only at the expense of increased values of (A/T) , so that it is often necessary in practice to make a compromise between finesse and transmission. This type of compromise is discussed further in Sec. III.

In the last section we found that the ultimate instrumental resolution, which we now call \mathcal{R}_0 , could be obtained only with an infinitesimally small axial aperture. In this case, of course, the étendue is also infinitesimal. A reasonable compromise between spectral resolving power and étendue can be reached by increasing the mirror aperture until the resolving power \mathcal{R} is reduced to a value of approximately $0.7 \mathcal{R}_0$. This, as we have seen, occurs when the mirror apertures have radii of approximately ρ_s . Under this condition, the étendue is given by:

$$U = [\pi\rho_s^2][\pi\rho_s^2/r^2] = \pi^2\lambda/F, \quad (29)$$

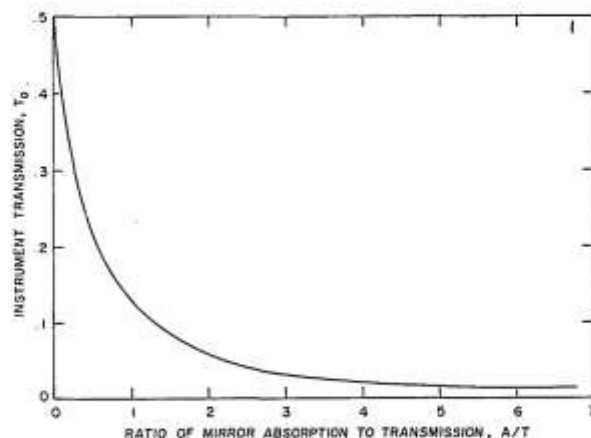


Fig. 7. FPS instrumental transmission as a function of the (absorption:transmission) ratio of the mirror coatings.

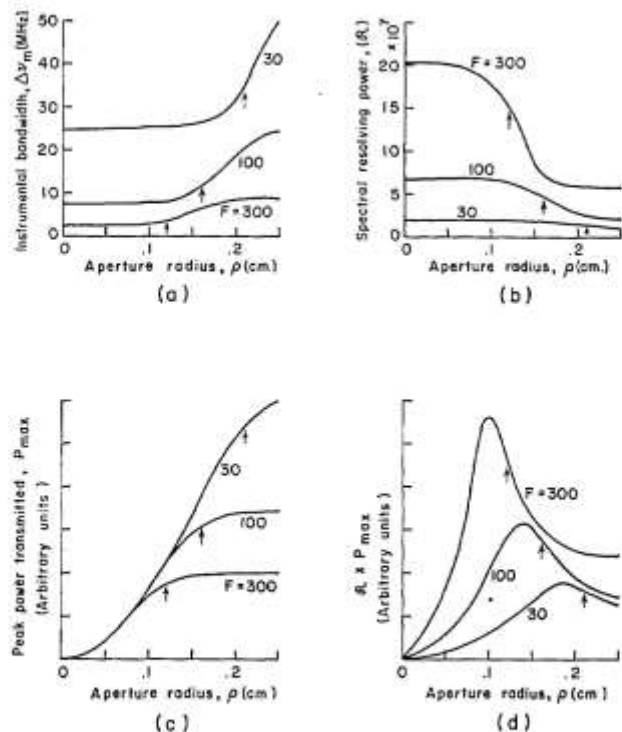


Fig. 8. Computed FPS characteristics as a function of detector aperture radius ρ for different values of F , the finesse. Arrows indicate the value of ρ_s in each case ($\epsilon = 0$, $r = 10$ cm). The maxima in the curves shown in (d) define the aperture radius giving the best compromise between resolving power and peak transmitted power.

where F is the finesse which determines the value of ρ_s according to Eq. (17).

Figure 8 shows computed curves for the instrumental bandwidth, spectral resolving power, peak transmitted power, and the product (peak transmitted power) \times (resolving power), all plotted as a function of aperture radius for finesses of 30, 100, and 300. These curves show that the resolution drops to about $0.7R_0$ when the aperture is opened up to a value of $\rho_s \equiv (\lambda r^3/F)^{1/2}$. Figure (8d), however, shows that the value of ρ which maximizes the product of the spectral resolving power and power transmitted is approximately $0.8\rho_s$. In practice, the most convenient way to quickly attain a useful compromise between resolution and transmitted power is to start with a relatively large aperture and, while observing the scanned spectrum of a narrow band source, to reduce the aperture size until the transmitted power at the peak of a displayed spectral line is reduced by between 20% and 30%. For this technique to be useful, of course, the mirror spacing must be very nearly confocal. This can be accomplished without much difficulty, as described in Sec. III.

3. Comparison of FPS and FPP

As Connes has pointed out, it is a unique characteristic of the FPS, amongst all other types of spectrometers, that, as the resolving power at constant finesse is increased (by increasing the mirror radii and separation),

so also is the étendue.¹ In fact, the quotient \mathcal{R}/U is a constant:

$$(\mathcal{R}/U)_{FPS} \approx 0.7(2F/\pi\lambda)^2. \quad (30)$$

In writing this expression, we accept the 20% to 30% loss in resolution which accompanies the realization of the étendue U . We also assume that, as the mirror radius is increased to realize higher resolving powers, we are able to maintain the required figure of $\approx \lambda/F$ across the central part of the mirror having a radius ρ_s . It is interesting to compare this behavior with that of an FPP. We assume that for an FPP, a net surface figure (including alignment error) of λ/F can be maintained across plates of diameter D , which are separated by a distance d . For this FPP the étendue is $(\pi D^2 \lambda / 4dF)$, and the resolving power is $(2df/\lambda)$, so that it is the product of the resolving power and étendue which remains constant:

$$(U\mathcal{R})_{FPP} \approx 0.7(\pi D^2/2). \quad (31)$$

(The factor of 0.7 again represents the loss in resolving power associated with a useful étendue.) Thus an increase in light gathering power must be paid for by a loss in resolution, and vice versa. The corresponding product for an FPS is given by:

$$(U\mathcal{R})_{FPS} \approx 0.7(4\pi^2 r^2). \quad (32)$$

From this expression we see that by increasing the mirror radius of an FPS the étendue resolution product may be increased indefinitely as long as the mirror figure can be maintained to within λ/F across an aperture of diameter $2\rho_s \equiv 2(\lambda r^3/F)^{1/2}$.

At this point, it should be quite clear that at high resolution, and correspondingly small free spectral range, the FPS excels over the FPP, both in terms of étendue and resolution. As the free spectral range is increased, however, there will be some point at which the FPP will become the better choice in terms of étendue. The specific value of r , the mirror spacing of the FPS, at which this transition occurs depends upon both the desired finesse and the accuracy with which the mirrors of the FPP can be figured and aligned. If we define an angle α to represent the figure-plus-alignment accuracy required to maintain a finesse F , with a plate diameter D :

$$\alpha = (\lambda/FD), \quad (33)$$

then the ratio U_{FPS}/U_{FPP} may be written:

$$U_{FPS}/U_{FPP} = 4rdF^2\alpha^2/\lambda^2, \quad (34)$$

where d is the plate separation of the FPP and where we tacitly assume that the spot size ρ_s on the FPS is small enough so that there is no problem in maintaining the necessary figure of λ/F . If we now require that both the FPP and FPS have the same free spectral range, so that $d = 2r$, then Eq. (34) can be used to find the value of r at which the FPP becomes the better choice with regard to étendue:

$$r^* = (\lambda/\alpha)/2F. \quad (35)$$

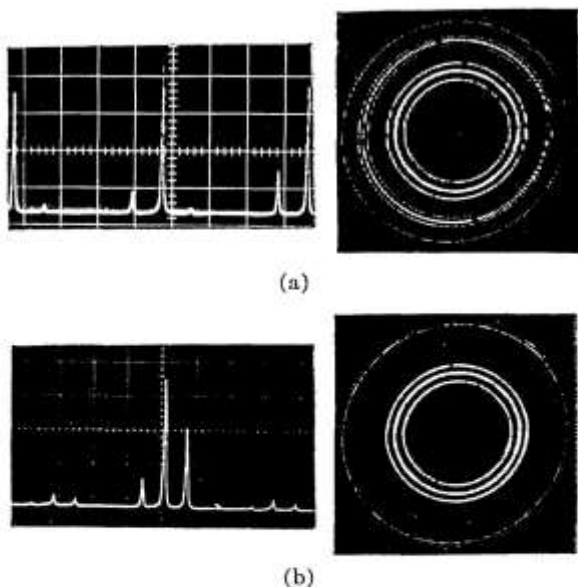


Fig. 9. (a) Scan and fringe displays of an FPS in normal operation. Note the secondary fringe pattern. (b) Scan and fringe displays of a very nearly mode-matched FPS. The alignment of the FPS relative to the source has been adjusted to eliminate the secondary fringe pattern, resulting in a doubling of both the free spectral range and the instrumental transmission. ($\epsilon \sim 20 \mu$, $r = 5$ cm; three-mode laser source.)

For example, if the mirrors of an FPP can be maintained plane and parallel to within a hundredth of a wavelength per cm of aperture, so that (λ/α) is 100, and a finesse of 25 is desired, then an FPP offers the greater étendue up to a mirror spacing of 4 cm. Rather than increasing the FPP mirror spacing beyond 4 cm, one should in principle, switch to an FPS in order to obtain higher resolution and maximum étendue.

D. Mode Analysis of an FPS

The equations derived earlier in this section have been based primarily on a geometrical analysis of a confocal resonator, or FPS. This, as it turns out, is adequate for most purposes. A more rigorous treatment, however, would involve a decomposition of the incident radiation field into eigenmodes of the resonator, as defined (in the curved mirror case) by Boyd and Gordon.⁷ In this section we outline an analysis of this sort and to some extent justify the simpler geometrical approach. We should point out that the aberrations of a confocal spherical mirror resonator, which give rise to the multiple beam interference fringes described earlier, can be conveniently analyzed only by the geometrical approach.

As shown by Boyd and Gordon, the eigenmodes TEM_{mnq} of a confocal resonator are closely approximated by Gaussian-Hermite functions [Ref. 7, Eq. (20)]. The first two subscripts m and n denote the amplitude distribution of the eigenmode on a surface of constant phase, and the third subscript q is the so-

called axial mode number giving the number of axial modes in the intracavity standing wave. For the general case of a resonator made up of two mirrors, radii b_1 and b_2 , separated by a distance d , Boyd and Kogelnik have shown that the resonant frequency associated with a given TEM_{mnq} mode is given by:

$$\nu_{mnq} = (c/2d)\{q + (1/\pi)(1 + m + n) \times \cos^{-1}[(1 - d/b_1)(1 - d/b_2)]^{1/2}\}. \quad (36)$$

We interpret this as follows: an arbitrary quasi-monochromatic field, of frequency ν_0 , which is incident on a curved mirror resonator, is decomposed into a large number of transverse modes TEM_{mn} . Each of these transverse modes will be resonant, i.e., will be transmitted by the high Q cavity, for mirror separations satisfying:

$$d = (c/2\nu_0)\{q + (1 + m + n) \times \cos^{-1}[(1 - d/b_1)(1 - d/b_2)]^{1/2}\}. \quad (37)$$

In general, therefore, a given quasi-monochromatic field will be decomposed into a large number of transverse modes, each of which is resonant for a different mirror separation. In order for a general curved mirror cavity to be useful as a scanning spectrum analyzer (or static filter), the input field must be reduced to a single transverse mode of the cavity, i.e., mode matched, so that the transmission of the cavity, as a function of mirror separation, can be unambiguously interpreted in terms of the frequency content of the input field. This can be accomplished without considerable loss of light only in the case of a laser light source operating in a single transverse mode.

For the special case of a confocal, or near confocal resonator, such as an FPS, Eqs. (36) and (37) become:

$$\nu_{mnq} \approx [c/4(r + \epsilon)][2q + (1 + m + n)], \quad (36a)$$

and

$$(r + \epsilon) \approx (c/4\nu_0)[2q + (1 + m + n)], \quad (37b)$$

where the mirrors have radii r and are separated by $(r + \epsilon) \approx r$. Thus, all transverse modes will resonate at cavity lengths of either,

$$(r + \epsilon) = (c/4\nu_0)(2l + 1); \quad l \text{ an integer, } (m + n) \text{ even,} \quad (38a)$$

or

$$(r + \epsilon) = (c/4\nu_0)(2l); \quad (m + n) \text{ odd.} \quad (38b)$$

If we assume that an arbitrary input field of frequency ν_0 is made up of an approximately equal number of even and odd transverse modes (a good approximation in any instance where mode-matching is not intentionally accomplished), then the cavity will be resonant for:

$$(r + \epsilon) = cl/4\nu_0; \quad l \text{ an integer,} \quad (39)$$

and the multimode free spectral range will be

$$\Delta\nu_f(\text{multimode}) \approx c/4r \quad (40)$$

If, on the other hand, the input field exactly matches a single mode of the cavity, the free spectral range is

$$\Delta\nu_f(\text{single transverse mode}) \simeq c/2r. \quad (41)$$

The transition from multimode to single mode excitation can be observed without undue difficulty, as illustrated in Fig. 9. (Note that the free spectral range increases by a factor of two for both scanning and static fringe modes of use of the FPS.) The tolerance on the alignment of the light beam relative to the axis of the FPS that is required for mode matched operation is on the order of λ/ρ_s , so that it is highly unlikely that this situation would be encountered inadvertently.

Mode matching of an FPS can also be considered from a more direct point of view. We have already mentioned the additional interference pattern arising from an angular misalignment of the two types of rays transmitted by the FPS. It is easy to show that, when these two types of transmitted beams are aligned, they are in phase on axis (assuming $r = m\lambda/2$), just out of phase at the first fringe off axis, in phase again for the second fringe, and so on. Thus the superposition of the two transmitted beams results in constructive interference in every other free spectral range, and destructive interference in the remaining orders—thereby effectively doubling the free spectral range and at the same time doubling the amount of light transmitted at a given resonance (when constructive interference occurs for the transmitted beams, destructive interference occurs for the two reflected beams).

The great advantage of the confocal FPS over a general curved mirror resonator is the freedom from the necessity to mode-match in order to observe a clean spectrum. This, as we have just seen, is due to the frequency degeneracy of even and odd transverse modes of a confocal cavity. It can readily be shown from Eq. (36) that the maximum value of $|\epsilon|$, the departure from exact confocal mirror spacing, which can be tolerated without allowing the TEM_{mn} transverse mode to resonate at an observably different mirror spacing from that at which the TEM_{00} mode is resonant, is given by:

$$|\epsilon|_{\max} = \pi r/2(1 + m + n)F \quad (42)$$

Thus an FPS with $r = 10$ cm and a finesse of 100 will begin to suffer a loss in effective finesse for $(m + n) \approx 100$ when $|\epsilon|$ becomes greater than about 15μ . Thus the variation in the mirror separation which occurs during direct scanning (less than a wavelength) is too small to affect the transverse mode degeneracy. Of course if pressure scanning is employed, it is the wavelength of the light which is changed, not the mirror separation.

III. Experimental Work with the FPS

This section is concerned with the practical aspects of the FPS, including its design and fabrication, alignment procedures, and various modes of operation. A number of applications are illustrated in the latter parts of this section.

A. General Design Considerations

There are three separate aspects of the design problem: (1) the mechanical design; (2) the attainment of high finesse, and (3) the optical layout. Each of these is briefly discussed in the following paragraphs.

1. Mechanical Design

The key mechanical requirements are that the two mirrors be accurately and rigidly fixed relative to each other; that there be a provision for making fine adjustments to the mirror separation (either during or after fabrication); that the optical separation of the mirrors be insensitive to temperature and/or pressure variation; and that the interferometer assembly be mechanically isolated from vibration and acoustic pickup. The requirements for rigidity and freedom from vibration dictate that the mirrors be held in a common structure, rather than mounted, for example, on a lens bench. This, in turn, means that any transducer used for varying the mechanical separation of the mirrors must be an integral part of the interferometer. Mechanical isolation of the rigid interferometer assembly is readily accomplished by mounting it in an outer case using a soft suspension (in the specific designs described later in this section, the outer case could be sharply struck without producing a detectable change in the observed spectrum—indicating a stability in the length of the optical cavity on the order of a one hundredth of a wavelength or better).

Insensitivity to pressure variations can be accomplished only by sealing the container holding the interferometer. This must be done, in any event, if the interferometer is to be pressure scanned. Insensitivity to temperature variations can be achieved both by conventional compensation, in which the expansions of dissimilar materials compensate for one another, and by the use of very low expansion materials. In an interferometer intended to serve as a passive frequency standard, we have combined both methods. As long as this interferometer is at a uniform temperature, its length can be maintained to within one part in 10^8 over a range of a few degrees centigrade.

The fine adjustment of mirror separation can easily be obtained using a well-made threaded mount for one mirror cell. For example, we found that a 12.7-mm diam cell with 16 threads/cm could be manually adjusted with a precision of at least a tenth of a wavelength providing that the mirror separation could be monitored by observing the spectrum from a stable gas laser. (Most gas lasers are far less stable, both mechanically and thermally, than the interferometers described here.) We were pleasantly surprised to find that the same precision of motion could also be obtained with a relatively loose screw fit when the slop was taken up with a thin Teflon tape commercially available as a pipe dope.

2. Attainment of High Finesse

The attainment of high finesse requires that the mirrors be of excellent optical quality and that they be

Table II. Characteristics of Some Multilayer Reflective Coatings

Type	Region of high reflectivity	F	T_0	R
A	6200 Å to 7000 Å	225	0.45	0.993
B	4800 Å to 6900 Å	150	0.35	0.99
C	4900 Å to 6800 Å	180-200	0.02	0.992

coated with high reflectivity multilayer dielectric films. For scanning applications, only the central spot, of radius ρ_s , need satisfy these requirements. If the interferometer is used to observe fringes, however, the mirror figure should be good over a somewhat larger area to ensure that the fringes will be circular. Mirror blanks should be tested against the same master; they generally require final polishing by hand if they are to have the necessary figure—that is to say, if they are to be spherical to within λ/F , where F is the desired finesse. Final evaluation of the mirror figure can only be made after the mirror has been coated and tested as an interferometer component. Not only must the mirror figure be excellent, but the polished surface must be free of microscopic scattering sites if the ultimate in reflectivity is to be realized. This is within the present state of the art, and scattering losses of less than 0.3% are attainable with fused quartz blanks.*

As we suggested in the last section, one is usually forced to make some sort of compromise between finesse, instrumental transmission, and possibly the spectral bandwidth within which the mirrors have high reflectivity. For example, using commercially available multilayer coatings (referred to as types A, B, and C) we were able to obtain the performance summarized in Table II. Type A is a narrow band coating covering a rather restricted spectral range, but offers high finesse combined with excellent transmission. Type B covers a considerably broader portion of the spectrum with fairly high instrumental transmission, but has a somewhat reduced finesse. Type C, on the other hand, has broad band coverage and relatively high finesse, but rather low transmission. By making fairly drastic sacrifices in instrumental transmission, it is probably possible to obtain finessses of up to 500 with commercially available coatings and a passive interferometer. This limitation is not set by available reflectivity, but by attainable mirror figure (or diffraction losses in the case of very short cavities).

3. Optical Layout

By *optical layout* we mean the optical system which brings the light into the interferometer and determines the path of light leaving the interferometer. For a number of reasons we have preferred to make the interferometer mirror blanks of very nearly zero optical

* It is now generally recognized that essentially scatter-free surfaces of excellent figure can be obtained by *continuous* and *extended* (12-36 h) final polishing of fused quartz blanks.

power. This permits the use of mirrors with concentric surfaces, which simplifies fabrication. More importantly though, it means that the interferometer can be used to spectrally filter a narrow collimated beam of light without appreciably affecting the collimation of the beam. If a further optical system is added to the FPS, it should serve to facilitate the alignment of the FPS with the light source, and to get light efficiently through the interferometer and within the instrumental passband. Figure 10 illustrates an optical system which has proved to be convenient and versatile. Consider first an incident collimated beam: lens L_1 brings the incident radiation to focus at the center of the interferometer. (Note that the path of light within the interferometer is just the reverse of the case where the light incident on the interferometer is collimated.) All of the light falling within a central circle of radius $2\rho_d f/r$ on lens L_1 will pass through the detector aperture of radius ρ_d , and will thus be filtered by the instrumental passband. In this mode of operation the FPS can be used as a static or tunable filter, or as a scanning spectrum analyzer. If the incident light is not collimated, there is no significant loss in resolution, but there may be a reduction in the amount of light received by the detector. This holds even for gross departures from collimation in the incident beam of light. The entire system should be free to rotate about the center of L_1 . In this way the incoming beam can be directed at the center of L_1 and then the entire interferometer system can be rotated about this point in order to attain alignment between the incoming beam of light and the axis of the FPS. The detector aperture, which limits the actual instrumental bandpass for incident beams with a large diameter, is located just behind the interferometer.

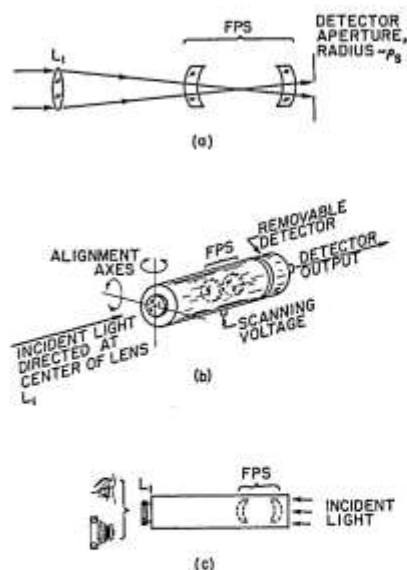


Fig. 10. A versatile FPS instrument. (a) Optical layout showing the FPS etalon, lens L_1 , and detector aperture; (b) arrangement for scanning; (c) arrangement for observing and recording fringe pattern (detector removed).

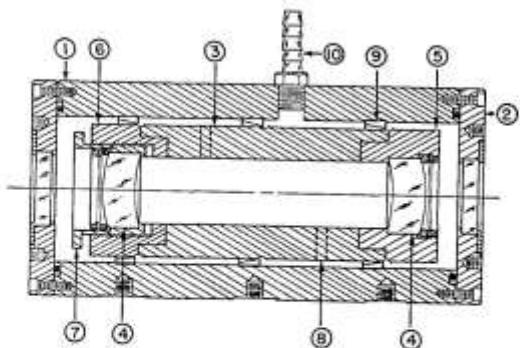


Fig. 11. Schematic of a highly stable fixed mirror FPS etalon: (1) outer case (Al alloy); (2) end plates with windows; (3) Cer-Vit etalon spacer; (4) fused quartz mirrors; (5) fixed mirror cell (Invar); (6), (7) adjustable mirror cell (Invar); (8) ports in etalon spacer; (9) phosphor bronze springs holding etalon; (10) fixture for evacuating chamber and pressure scanning.

This design facilitates the observation of the static fringe pattern. If the detector aperture is removed and a quasi-collimated beam of light is incident on what was the rear of the system, then the fringe pattern will be formed in the focal plane of lens L_1 . Thus an observer, or camera focused on infinity, can readily view the fringe pattern. If the incident beam is diverging, rather than collimated, then the plane of the fringe pattern will be slightly displaced *towards* the lens, and vice versa. A low power focusing telescope is useful both for observing the fringe pattern, and for photographing it. In this mode of operation, the system should be mounted so that it can be rotated about a point near the right-hand interferometer mirror [Fig. 10(c)]. To use the interferometer as a narrow bandpass filter with zero optical power, the lens is simply removed.

In order to eliminate ghost fringe patterns, the rear surfaces of the FPS mirrors, and both surfaces of L_1 , should be antireflection coated.

B. Design of a Static or Pressure Scanned FPS

This design, shown in Fig. 11, is intended primarily to eliminate variation of the axial mirror separation with temperature. This FPS is thus well suited for use as a secondary frequency standard with a long term stability of better than 1 MHz with temperature control of $\pm 1^\circ\text{C}$. This thermal stability is obtained by making the mirror spacer of Cer-Vit* (thermal expansion coefficient no greater than $\pm 0.1 \times 10^{-7}/^\circ\text{C}$), and using the Invar mirror cells thermally to compensate for the residual expansion of the Cer-Vit (this can easily be done since the manufacturers of Cer-Vit routinely supply accurate expansion data for each blank). The quartz mirrors change radius by about a wavelength for a 1°C temperature change, but this introduces a negligible change in the mirror separation, which determines the resonant frequency of the FPS.

* Cer Vit is a low expansion semitransparent glasslike ceramic manufactured by Owens-Illinois.

We have not yet established the lower limit on the frequency stability of this system.

The interferometer assembly is held inside a pressure chamber by means of phosphor-bronze finger-stock springs, which provide adequate mechanical isolation. The pressure chamber can be used for pressure scanning, or it can be partially evacuated and sealed to eliminate effects due to changes in atmospheric pressure.

Applications for this type of interferometer include ultrahigh resolution spectroscopy, and use as a passive feedback component in frequency stabilizing lasers.

C. A Piezo-electrically Scanned FPS System

This instrument is designed along the lines illustrated in Fig. 10, and can be used as a scanning spectrum analyzer, as a tunable narrow bandpass filter with zero optical power, or for direct observation of multiple beam interference fringes. The key element in the instrument is the FPS etalon, which is comprised of a fixed and an adjustable mirror cell, and a thermally compensated rigid spacer tube. The spacer tube includes, as an integral component, a piezo-electric ceramic section which increases in length by about $1.5 \text{ cm} \times 10^{-6} \text{ cm}$ with the application of 50 V across the inner and outer surfaces of the tube (sufficient to scan a complete free spectral range in the visible). The adjustable mirror cell permits the mirror spacing to be easily set to within a fraction of a micron. Further fine adjustment can be accomplished by applying a dc voltage to the scanning voltage terminal; this is the method of tuning in the bandpass-filter mode of operation. Figure 12 shows a cut-away view of the entire instrument.

The FPS etalon is mechanically isolated from the case by a mounting technique using two large silicone rubber O-rings which cushion the etalon from mechanical shocks (see Fig. 12). The outer case can be struck sharply from any direction without noticeably affecting the resonant frequency of the etalon. As shown in Fig.

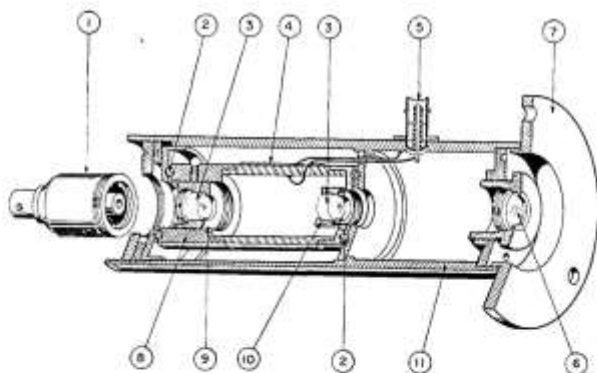


Fig. 12. An FPS spectrum analyzer for scanning or static mode of operation: (1) removable detector (photodiode); (2) soft O-ring for mounting FPS etalon; (3) quartz mirrors ($r = 5 \text{ cm}$); (4) piezo-electric transducer/etalon spacer; (5) scanning voltage terminal; (6) auxiliary lens (focal point is between mirrors); (7) mounting flange; (8), (9) adjustable mirror cell; (10) fixed mirror cell; (11) outer case. (The mirror cells are designed to compensate for the thermal expansion of the etalon spacer.)

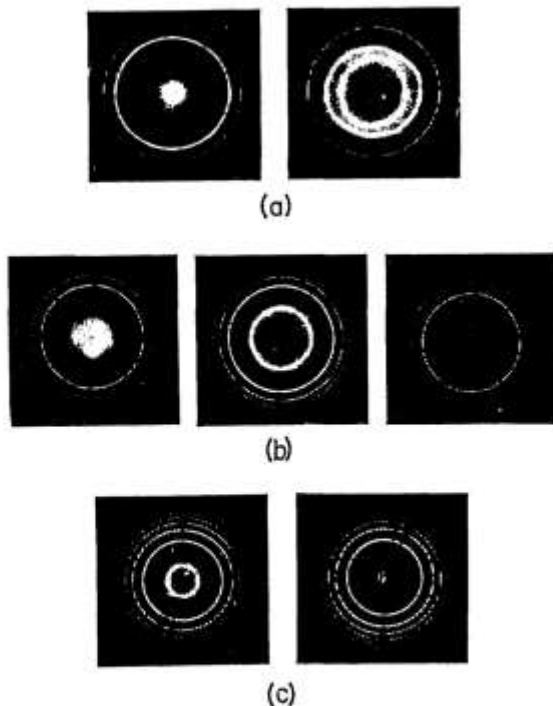


Fig. 13. Typical fringe patterns in the vicinity of confocal separation for a 10-cm FPS. In each case, the source is a single mode He-Ne laser. Variations in the fringe patterns in each horizontal row were obtained by making small changes ($<\lambda/4$) in the mirror separation. (a) $\epsilon = -70 \mu$, (b) $\epsilon = 0$, (c) $\epsilon = 70 \mu$.

10, the lens at one end of the instrument serves either of two functions: to direct an incident beam of radiation into the center of the FPS etalon (scanning or filter modes of operation), or to image the interference fringe pattern at infinity when light is incident on the other end of the instrument (visual or photographic modes of operation). In the scanning mode, a small photodetector is mounted directly behind the FPS. We have used both a silicon photodiode and a photomultiplier as the detector (the majority of the scans shown in Sec. III.E were obtained with a photodiode operating in the photovoltaic mode). Since it is desirable—for ease in alignment—to rotate the entire instrument about the entrance aperture, the mounting flange can be attached at either end of the instrument. This flange then serves to attach the instrument to a mirror-mount which is adjustable in angle.

The mirror radius in the FPS is 5 cm, with a corresponding free spectral range of 1500 MHz.* Using

*Note added in proof: By replacing the 5-cm radius mirrors with 1-cm mirrors, and modifying one mirror cell to provide for a 1-cm mirror separation, we were recently able to extend the free spectral range of this instrument to 7.5 GHz (or 0.09 Å at 6000 Å). Using narrowband mirrors, a finesse in excess of 100 was easily attained with a 0.5-mm detector aperture. This type of instrument has proved useful in examining ion laser spectra. Comparable finesse in an FPP with the same free spectral range is very difficult to obtain.

multilayer dielectric mirrors, we can obtain a finesse of greater than 150 over a spectral range of about 1200 Å, and with an instrumental transmission of 40% to 45% (compared with the maximum of 50% in the nonmode-matched configuration). With careful mode matching, the instrumental transmission goes to 80–90%, the free spectral range becomes 3000 MHz, and the finesse is doubled—leaving the resolving power unchanged. With broadband multilayer mirrors, a finesse of 150 can be maintained from about 4900 Å to 7000 Å, with an instrumental transmission of approximately 25% (or 50% when mode matched). With these mirrors, this instrument has been used for high resolution spectroscopy with argon lasers (4880 Å and 5145 Å), He-Ne lasers (6328 Å) and Q-switched ruby lasers (6943 Å). A variety of experimental data is shown in Sec. III.E.

In the scanning mode, the instrument is very easy to align to the incident beam of light. First of all, the instrument is located so that the incident light beam (preferably, but not necessarily, more or less collimated) falls close to the center of the lens. The axis of the instrument is then roughly aligned with the incident beam. This can be done most conveniently by observing the light that has been reflected from the FPS back towards the source: the reflected beam should be adjusted to lie fairly close to the incident beam. At this point a high resolution scan display can be observed by monitoring the detector output at an oscilloscope. The display is peaked by further small adjustments to the alignment. The scanning voltage is conveniently provided by the sawtooth (or horizontal scan) voltage from the oscilloscope. This voltage will typically scan two or three free spectral ranges, and assures synchronism between the applied scanning voltage and the oscilloscope sweep. Moreover, this technique provides a highly linear display of the optical spectrum at the oscilloscope.

To observe interference fringes, the detector is removed and the incident beam is directed towards the end of the instrument at which the detector was located. The fringe pattern can then be viewed directly through the lens, or an auxiliary telescope can be used. The latter is particularly useful when the incident beam is not collimated, resulting in a displacement of the plane of the fringe pattern away from the focal plane of the lens. The proper alignment of the instrument axis relative to the incident beam of light can be made by observing fringe pattern and making angular adjustments to make the fringes circular. As mentioned earlier, it may be desirable to change the mirror spacing slightly to obtain a more nearly linear display of frequency in the fringe pattern, although this entails a reduction in the realizable spectral resolution (Fig. 14).

D. Alignment Procedures

In assembling and using FPS interferometers, only a few alignments or adjustments are required, and in this section procedures for these are briefly described.

1. Establishing the Confocal Mirror Separation

We have pointed out that optimum performance of an FPS depends critically upon the proper spacing of the mirrors. Connes has described an imaging technique for approximating this adjustment which requires only a small incoherent light source.² If a He-Ne laser is available, the alignment can be made with high precision as follows. First, adjust the mirror separation to within a millimeter or so from knowledge of the mirror radii. Then, set up the FPS etalon so that a quasi-collimated beam from the gas laser is incident on one mirror, and arrange to view the interference fringes which are formed in the vicinity of the central plane of the etalon. The laser beam diameter should be large enough to allow several fringes to be seen. Next, make a fine adjustment of the mirror separation to bring the mirrors *closer together* by a fraction of a wavelength, and observe the resulting change in the central fringe radius. This fine adjustment can usually be made by manually squeezing the etalon. If the mirror separation is *greater* than the confocal separation, the central fringe will become *smaller* in diameter as the mirrors are moved towards each other. If the mirror separation is *less* than the confocal spacing, the central fringe diameter will *increase* as the mirrors are moved towards one another. Figure 13 shows the appearance of the central fringes on either side of exact confocal spacing, as well as at the confocal spacing. As shown in Fig. 13(a), when the mirrors are spaced by slightly less than confocal spacing, there is a zone [radius $(-2e)^{1/2}$] of high dispersion toward which all fringes gravitate as the mirror spacing is slightly reduced (or, equivalently, as the wavelength of the quasi-monochromatic light source is increased). This zone approaches the center of the fringe pattern as the mirror separation is increased, and disappears through the center of the pattern when the confocal spacing is exceeded. The location of this zone is an extremely sensitive indication of the mirror separation, and when the mirrors are exactly confocal it is at the center of the fringe pattern. The radius of this zone, as a function of mirror separation, is shown by the dotted line in Fig. 3.

If the FPS is set up in the scanning mode it is possible to peak up the adjustment of the mirror separation merely by maximizing the amplitude of a displayed laser spectrum while at the same time minimizing the apparent width of individual spectral components. With very little practice it becomes a simple matter to establish confocal separation to within a micron or so using this technique. As the optimum mirror separation is approached, one should also make fine adjustments to the angular alignment—unless a very small diameter beam is used, in which case the spectral display is relatively insensitive to alignment.

2. Selecting the Optimum Detector Aperture

As mentioned earlier, the diameter of the detector aperture [or, equivalently, the diameter of the incident beam: see Fig. 10(a)] serves to define both the actual instrumental bandwidth and the étendue. As a rule,

one seeks a compromise in which a considerable étendue can be attained with only slight sacrifice in resolving power. The curves in Fig. 8(d) show that the optimum compromise occurs when the radius of the detector aperture (assuming it to be located adjacent to the rear interferometer mirror) is just under ρ_s . Figure 14 shows experimental data for the instrument profile of a 10-cm FPS, with a nominal finesse of just over 100, for various detector apertures. In this figure the desirability of using the optimum detector aperture is obvious. For larger apertures, the *peak* transmitted power goes up very little, and the resolution goes down. Note, however, that at larger apertures more *total* light is transmitted: this may be an important consideration in applications involving weak light sources. It is worth pointing out that the finite time constant of a high finesse FPS precludes the use of very high sweep speeds without suffering a loss in resolution—in this case, too, it would make sense to use a somewhat larger detector aperture than normal.

3. Alignment for Mode Matching

There are undoubtedly applications where it might prove useful to extend the free spectral range of an FPS by mode matching. The gain in free spectral range is accompanied by a twofold increase in both finesse and instrumental transmission, so that there is no loss in spectral resolution. There is, however, a very great reduction in the tolerance of the alignment between the FPS axis and the incident light beam, and there is also the restriction that the incoming beam match a lowest order transverse mode of the cavity. This latter restriction is less severe than it might be, due to the degeneracy of a confocal cavity. Unlike a general curved mirror cavity, the position of the beam waist of the lowest order transverse mode is not uniquely de-

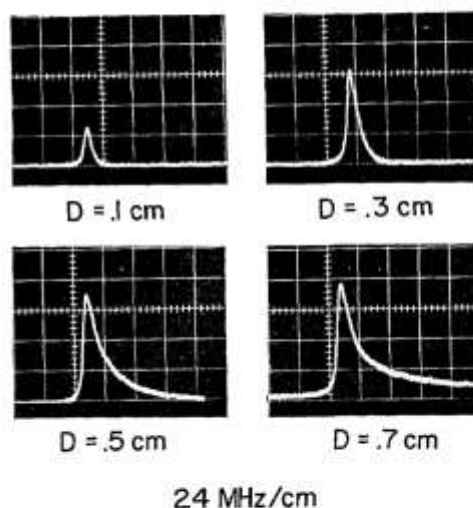


Fig. 14. Observed instrumental profiles for different detector aperture diameters D . Light source was a 1-cm wide collimated single mode laser beam. ($\epsilon \sim 0$; $r = 10$ cm.) The 0.3-cm aperture is clearly the best compromise between signal amplitude and resolution.

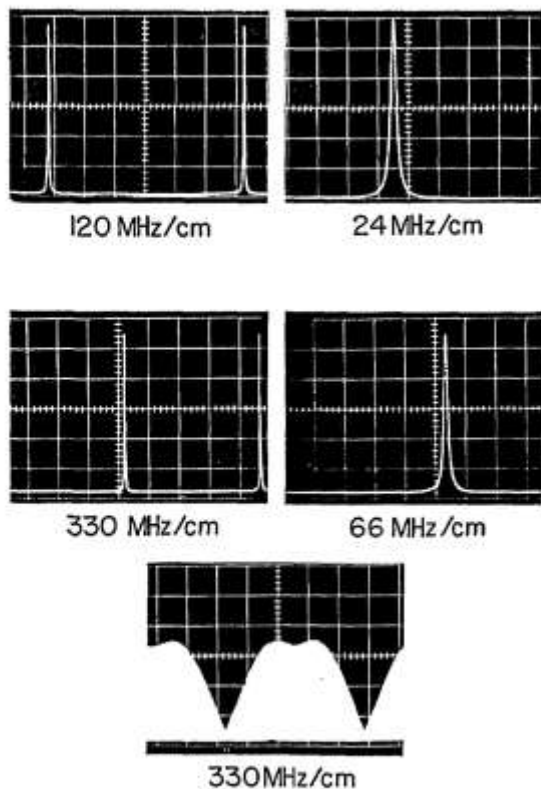


Fig. 15. Spectra of a single mode laser obtained with 5-cm and 10-cm scanning FPS instruments. Top: 10-cm FPS, measured finesse $F \sim 154$; middle: 5-cm (broadband mirrors), $F \sim 148$; bottom: single mode He-Ne gain profile, showing Lamb's dip (see text).

terminated, but can be located anywhere between the two mirrors (the diffraction losses are minimized, however, when the beam waist is at the center of the cavity). This type of confocal cavity degeneracy is particularly clear from the geometrical construction for gaussian mode propagation described by Laues.⁸ Thus, for a confocal laser, the problem of mode matching is largely a problem of aligning the optical axis of the FPS, i.e., the line joining the centers of curvature of the two mirrors, to that of the incoming light beam. Stated in another way, the basic problem is to locate the source (or its image) and both centers of curvature on a single straight line.

The mode matching alignment problem, as just stated, obviously requires both angular and lateral displacements of the FPS—regarding the source as fixed. When the source is at infinity (collimated), however, it is clear that only angular adjustments are required. This simplifies the problem considerably. Using a collimated beam, the procedure is as follows. First, set up the FPS in the same manner used for observing multiple beam interference fringes [Fig. 10(c)]. Then, while viewing the fringe pattern, adjust the angular alignment of the FPS until a two-beam interference pattern of straight fringes can be seen superimposed on the circular fringes [cf., Fig. 9(a)]. Next, make fine adjustments to increase the straight-fringe spacing until it is large compared to the spot size ρ_s , or at least greater

than the detector aperture at the center of an image of the circular fringe pattern. Finally, observe the scan display and touch up the alignment as required. The procedure is somewhat inefficient in that much of the light in the collimated beam fails to reach the detector. Note that the alignment precision is approximately λ/ρ_s and thus requires interferometric stability between the source and the FPS.

As an alternate procedure, one can use the technique described by Fork *et al.* for mode matching to a general curved mirror cavity.⁹ Also, we have found that with practice one can set up the FPS in the normal scanning mode and then hunt for the mode-matched condition by making small lateral and angular adjustments while observing the scan display. As the proper alignment is approached, the spectral display in every other free spectral range is slightly increased in amplitude, while the remaining portion of the display is decreased in amplitude. This hunting procedure is not very reliable, and generally takes longer than the alignment described above.

E. Some Experimental Results

One of the first characteristics of an FPS instrument which one would like to determine experimentally is its instrumental bandpass or, equivalently, its finesse. This is conveniently accomplished by observing the spectrum of a relatively stable gas laser, whose individual spectral components are generally orders of magnitude narrower than one could hope to observe directly. Figure 15 shows spectra of a stable single mode He-Ne laser which were obtained with 5-cm and 10-cm scanning FPS instruments of the type described in Sec. III.C. The 5-cm FPS had broadband mirrors (4800 Å to 6900 Å), while the 10-cm FPS had conventional narrowband mirrors peaked at approximately 6500 Å. The finesse in both cases was about 150. The scanning voltage was supplied directly from the oscilloscope's horizontal sweep, and the duration of each sweep was 10 msec. Also shown in Fig. 15 is the gain profile of the single mode He-Ne laser, clearly showing Lamb's dip and thereby the collision-broadened homogeneous linewidth in He-Ne (this gain profile was obtained by slowly changing the laser cavity length and integrating the displayed spectrum with a storage oscilloscope).

We also found that it was a simple matter to indirectly determine the instrumental linewidth by making a direct measurement of the FPS cavity lifetime τ :

$$\tau = 2rF/\pi c = (2\pi\Delta\nu_m)^{-1}. \quad (43)$$

This lifetime could be observed with fair precision by using a 10-nsec Q -switched laser pulse as a realizable approximation to a temporal delta function, and detecting the transmission of the FPS as a function of time with a fast phototube and scope. The resultant trace was very nearly an exponential decay, and gave results in good agreement with other measurements. Note that it is not necessary that the Q -switched pulse have a narrow spectrum, although the alignment between the laser beam and FPS must be good.

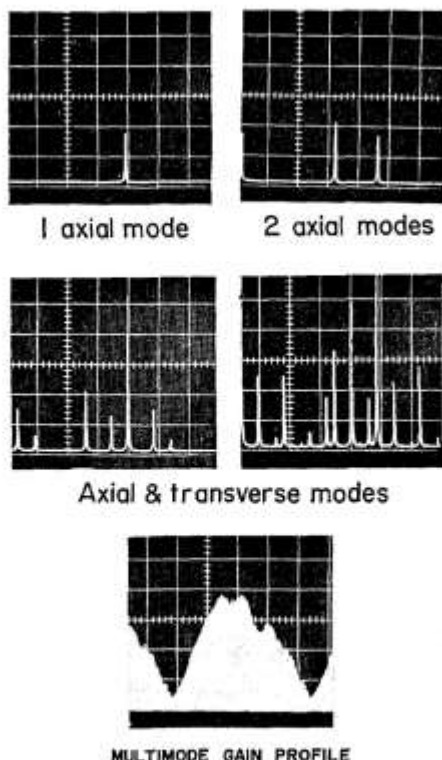


Fig. 16. Spectra of an adjustable multimode He-Ne gas laser. Various numbers of modes were excited by adjusting the laser mirrors. The 5-cm FPS shown in Fig. 12 was used. 330 MHz/cm.

Figure 16 shows the spectra which were obtained using an inexpensive commercially available He-Ne laser which could be operated in one or many transverse and axial modes by adjusting the mirror alignment. This figure clearly shows the ability of the FPS to record the spectra of higher order transverse modes (only by observing the laser spectrum can very weak higher order transverse modes be detected). The gain profile shows a raggedness due to competition effects between different modes, and an asymmetry due to the presence of more than one isotope of neon in the He-Ne mixture. The spectra shown in Fig. 16 were all obtained with a 5-cm FPS with a free spectral range of 1500 MHz (or approximately 0.02 Å at 6328 Å).

The fringe patterns shown in Fig. 17(a) and (b) show the spectra of a 60-cm He-Ne laser operating in three axial modes, with just the TEM_{00} transverse mode [see Fig. 17(a)], and with both TEM_{00} and TEM_{01} transverse modes [see Fig. 17(b)]. These spectra were obtained with the same instrument used in obtaining the spectra shown in Fig. 16, although a different laser was used. The mirror separation was approximately 50 μ in excess of confocal, resulting in a lower radial dispersion near the center of the pattern than would otherwise be obtained. Figure 17(c) shows the spectrum of a Q-switched laser operating in a single mode (TEM_{00}), and was obtained with a 10-cm FPS in exact confocal adjustment. The anomalously large recorded linewidth (>200 MHz) is due to a continuous

frequency drift during the evolution of the 10-nsec Q-switched laser pulse. The origin of the frequency drift has not been clearly established, but it is power dependent and approaches zero near threshold for the Q-switched ruby laser.

In many instances it is desirable to make a precise determination of the separation of two spectral lines or of the width of a single line, from a photograph of an FPS fringe pattern. This requires an exact knowledge of both the magnification M of the fringe pattern in the photograph and the departure from confocal separation ϵ . If the two spectral lines in question give rise to fringes of radii ρ_1 and ρ_2 in the photograph of the fringe pattern (both in the same free spectral range), then it is straightforward to show that their frequencies differ by:

$$\Delta\nu \equiv (\nu_2 - \nu_1) = (\bar{\nu}/4r^4)[(\rho_2^4 - \rho_1^4)M^{-4} + 4r\epsilon(\rho_2^2 - \rho_1^2)M^{-2}] \quad (44)$$

where $\bar{\nu}$ is the mean optical frequency. By the same token, if a single spectral component gives rise to fringes of radii ρ_1 , ρ_2 , and ρ_3 in adjacent free spectral ranges (corresponding to spectral lines of known frequency difference, $c/4r$), then the equation above can be used to solve for both M and ϵ in terms of ρ_1 , ρ_2 , ρ_3 , and r (the mirror radius).

IV. Summary

We have found the spherical Fabry-Perot interferometer to be an extremely versatile high resolution spectroscopic tool. It is particularly well suited, because of its high resolution and limited, free spectral range, to the study of laser and laser-derived, e.g., stimulated and spontaneous scattering of laser light, light sources. It can readily be adapted for pressure or

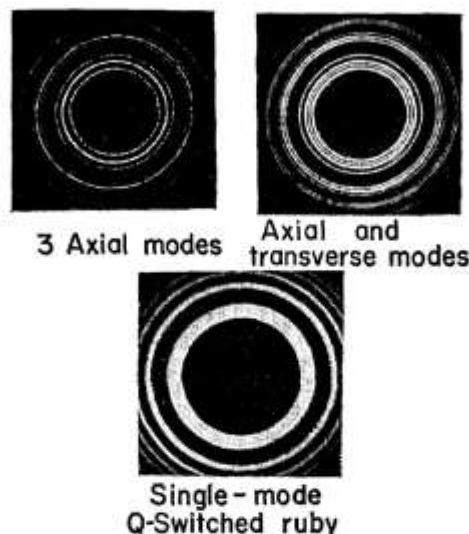


Fig. 17. Top left: spectrum of a He-Ne gas laser operating in three axial modes and the TEM_{00} transverse mode. ($\epsilon \sim 20 \mu$, $r = 5$ cm, free spectral range 1500 MHz). Top right: same as above, but with an additional TEM_{01} mode in oscillation. Bottom: spectrum of a 10-nsec single mode pulse from a Q-switched ruby laser (see text). ($\epsilon \sim 0$, $r = 10$ cm, free spectral range 750 MHz).

mechanical scanning, fringe display, or tunable narrow band filtering. The important limitations of an FPS are its relatively narrow free spectral range (generally less than a few thousand megahertz), and the inability to vary the free spectral range attainable with a given pair of mirrors. Some of the advantages of an FPS over other types of optical spectrum analyzers are listed below.

(a) Ease in attaining high finesse—thereby taking advantage of the high reflectivities now available with commercially available dielectric coatings.

(b) Ease of alignment: once the initial mirror separation is set, no further adjustments are required. The only alignment required is that of the entire FPS etalon relative to the light source, and this alignment is not critical.

(c) High étendue (light gathering power) without sacrifice in spectral resolution.

(d) Large acceptance angle when used as an optical filter ($\Omega \approx 4\pi(\lambda/rF)^2$ sr).

(e) The transverse mode degeneracy of the confocal cavity obviates the necessity for mode matching.

(f) Versatility: a single FPS instrument can be designed to serve in three modes of operation, i.e., scanning, fringe display, and optical filtering.

Using readily available mirror coatings, passive FPS interferometers of reasonable length (50 cm) can easily resolve down to a fraction of a megahertz and, if properly stabilized and thermally compensated, can provide convenient and portable secondary optical wavelength standards. In addition to spectroscopic applications, we plan to use FPS instruments as optical FM discriminators, and as passive elements in laser frequency stabilization servo loops.

Appendix I. Normalized Equations for FPS

In illustrating the performance of an FPS with the calculated curves shown in various figures, we chose to use specific values for the pertinent parameters r , ϵ , λ , and ρ . This was done, rather than using dimensionless normalized parameters, so the reader could get an idea of the actual values of these parameters in a typical case: namely, $r = 10$ cm and $\lambda = 6250$ Å ($\nu = 4.8 \times 10^{14}$ Hz).

If we wish, we can define normalized dimensionless variables; $r_n = r/\lambda$, $\epsilon_n = \epsilon/\lambda$, and $\rho_n = \rho/\lambda$, so that the normalized fringe radii are given by:

$$(\rho_n^4 r_n^2) + (4\epsilon_n \rho_n^2 / r_n^2) = (m - \xi), \quad (A1)$$

where ξ is the fractional order of interference on axis. The spot size has a normalized radius,

$$(\rho_s)_n = (r_n^2 / F)^{1/2}. \quad (A2)$$

With these equations, it is straightforward to convert the calculated curves to normalized curves which apply to any set of system parameters. As an alternative, we list below recipes for converting the calculated curves so that they may be used with different values of r and/or λ . (The distances r_0 and λ_0 are 10 cm and 6.25×10^{-5} cm, respectively.)

Figure 3. If the mirror radii are each $r = ar_0$, and if $\lambda = b\lambda_0$, then: (i) change each value of ρ to $\rho' = \rho a^2$, and (ii) change each value of m , the order of interference relative to the order on axis, to $m' = m/(ab)$, (iii) The ϵ axis remains unchanged. [Note that the curve defining ρ_s corresponds to $m = (1/F)$.]

Figure 4. If $r = ar_0$ and $\lambda = b\lambda_0$, then change ρ to $\rho' = a^2 b^2 \rho$.

Figure 5. If $r = ar_0$ and $\lambda = b\lambda_0$, then: (i) change ρ to $\rho' = a^2 b^2 \rho$, and (ii) change $(\nu - \nu_0)$ to $(\nu - \nu_0)' = (\nu - \nu_0)/a$.

Figure 8. Same as Fig. 4.

References

1. P. Connes, *Rev. Opt.* **35**, 37 (1956).
2. P. Connes, *J. Phys. Radium* **19**, 262 (1958).
3. P. Connes, in *Quantum Electronics and Coherent Light*, P. A. Miles, Ed. (Academic Press, Inc., New York, 1964), p. 198ff.
4. W. H. Steel, *Interferometry* (Cambridge University Press, Cambridge, 1967), p. 123.
5. K. M. Baird and G. R. Hanes, in *Applied Optics and Optical Engineering*, R. Kingslake, Ed. (Academic Press, Inc., New York, 1967), Vols. 4 and 5, p. 350.
6. R. L. Fork, D. R. Herriott, and H. Kogelnik, *Appl. Opt.* **3**, 1471 (1964).
7. G. D. Boyd and J. P. Gordon, *Bell Sys. Tech. J.* **40**, 453 (1961).
8. P. Laures, *Appl. Opt.* **6**, 747 (1967).



John S. Gailey is sales manager—technical optics in the Optical Products Department of Corning Glass Works.

Laser Beams and Resonators

H. KOGELNIK AND T. LI

Abstract—This paper is a review of the theory of laser beams and resonators. It is meant to be tutorial in nature and useful in scope. No attempt is made to be exhaustive in the treatment. Rather, emphasis is placed on formulations and derivations which lead to basic understanding and on results which bear practical significance.

1. INTRODUCTION

THE COHERENT radiation generated by lasers or masers operating in the optical or infrared wavelength regions usually appears as a beam whose transverse extent is large compared to the wavelength. The resonant properties of such a beam in the resonator structure, its propagation characteristics in free space, and its interaction behavior with various optical elements and devices have been studied extensively in recent years. This paper is a review of the theory of laser beams and resonators. Emphasis is placed on formulations and derivations which lead to basic understanding and on results which are of practical value.

Historically, the subject of laser resonators had its origin when Dicke [1], Prokhorov [2], and Schawlow and Townes [3] independently proposed to use the Fabry-Perot interferometer as a laser resonator. The modes in such a structure, as determined by diffraction effects, were first calculated by Fox and Li [4]. Boyd and Gordon [5], and Boyd and Kogelnik [6] developed a theory for resonators with spherical mirrors and approximated the modes by wave beams. The concept of electromagnetic wave beams was also introduced by Goubau and Schwering [7], who investigated the properties of sequences of lenses for the guided transmission of electromagnetic waves. Another treatment of wave beams was given by Pierce [8]. The behavior of Gaussian laser beams as they interact with various optical structures has been analyzed by Goubau [9], Kogelnik [10], [11], and others.

The present paper summarizes the various theories and is divided into three parts. The first part treats the passage of paraxial rays through optical structures and is based on geometrical optics. The second part is an analysis of laser beams and resonators, taking into account the wave nature of the beams but ignoring diffraction effects due to the finite size of the apertures. The third part treats the resonator modes, taking into account aperture diffraction effects. Whenever applicable, useful results are presented in the forms of formulas, tables, charts, and graphs.

Manuscript received July 12, 1966.

H. Kogelnik is with Bell Telephone Laboratories, Inc., Murray Hill, N. J.

T. Li is with Bell Telephone Laboratories, Inc., Holmdel, N. J.

2. PARAXIAL RAY ANALYSIS

A study of the passage of paraxial rays through optical resonators, transmission lines, and similar structures can reveal many important properties of these systems. One such "geometrical" property is the stability of the structure [6], another is the loss of unstable resonators [12]. The propagation of paraxial rays through various optical structures can be described by ray transfer matrices. Knowledge of these matrices is particularly useful as they also describe the propagation of Gaussian beams through these structures; this will be discussed in Section 3. The present section describes briefly some ray concepts which are useful in understanding laser beams and resonators, and lists the ray matrices of several optical systems of interest. A more detailed treatment of ray propagation can be found in textbooks [13] and in the literature on laser resonators [14].

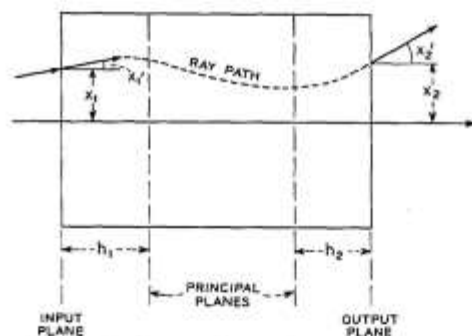


Fig. 1. Reference planes of an optical system. A typical ray path is indicated.

2.1 Ray Transfer Matrix

A paraxial ray in a given cross section ($z = \text{const}$) of an optical system is characterized by its distance x from the optic (z) axis and by its angle or slope x' with respect to that axis. A typical ray path through an optical structure is shown in Fig. 1. The slope x' of paraxial rays is assumed to be small. The ray path through a given structure depends on the optical properties of the structure and on the input conditions, i.e., the position x_1 and the slope x_1' of the ray in the input plane of the system. For paraxial rays the corresponding output quantities x_2 and x_2' are linearly dependent on the input quantities. This is conveniently written in the matrix form

$$\begin{vmatrix} x_2 \\ x_2' \end{vmatrix} = \begin{vmatrix} A & B \\ C & D \end{vmatrix} \begin{vmatrix} x_1 \\ x_1' \end{vmatrix} \quad (1)$$

TABLE I
RAY TRANSFER MATRICES OF SIX ELEMENTARY OPTICAL STRUCTURES

NO	OPTICAL SYSTEM	RAY TRANSFER MATRIX
1		$\begin{vmatrix} 1 & d \\ 0 & 1 \end{vmatrix}$
2		$\begin{vmatrix} 1 & 0 \\ -1/f & 1 \end{vmatrix}$
3		$\begin{vmatrix} 1 & d \\ -1/f & 1-d/f \end{vmatrix}$
4		$\begin{vmatrix} 1 - d_2/f_1 & d_1 + d_2 - d_1 d_2/f_1 \\ -1/f_1 - 1/f_2 + d_2/f_1 f_2 & 1 - d_1/f_1 - d_2/f_2 - d_1 d_2/f_1 f_2 \end{vmatrix}$
5		$\begin{vmatrix} \cos d \sqrt{n_2/n_0} & 1/\sqrt{n_0 n_2} \sin d \sqrt{n_2/n_0} \\ -\sqrt{n_0 n_2} \sin d \sqrt{n_2/n_0} & \cos d \sqrt{n_2/n_0} \end{vmatrix}$
6		$\begin{vmatrix} 1 & d/n \\ 0 & 1 \end{vmatrix}$

where the slopes are measured positive as indicated in the figure. The $ABCD$ matrix is called the ray transfer matrix. Its determinant is generally unity

$$AD - BC = 1. \quad (2)$$

The matrix elements are related to the focal length f of the system and to the location of the principal planes by

$$f = -\frac{1}{C}$$

$$h_1 = \frac{D - 1}{C} \quad (3)$$

$$h_2 = \frac{A - 1}{C}$$

where h_1 and h_2 are the distances of the principal planes from the input and output planes as shown in Fig. 1.

In Table I there are listed the ray transfer matrices of six elementary optical structures. The matrix of No. 1 describes the ray transfer over a distance d . No. 2 describes the transfer of rays through a thin lens of focal length f . Here the input and output planes are immediately to the left and right of the lens. No. 3 is a combination of the first two. It governs rays passing first over a distance d and then through a thin lens. If the sequence is reversed the diagonal elements are interchanged. The matrix of No. 4 describes the rays passing through two structures of the No. 3 type. It is obtained by matrix multiplication. The ray transfer matrix for a lenslike medium of length d is given in No. 5. In this medium the refractive index varies quadratically with the distance r from the optic axis.

$$n = n_0 - \frac{1}{2} n_2 r^2. \quad (4)$$

An index variation of this kind can occur in laser crystals and in gas lenses. The matrix of a dielectric material of index n and length d is given in No. 6. The matrix is referred to the surrounding medium of index 1 and is computed by means of Snell's law. Comparison with No. 1 shows that for paraxial rays the effective distance is shortened by the optically denser material, while, as is well known, the "optical distance" is lengthened.

2.2 Periodic Sequences

Light rays that bounce back and forth between the spherical mirrors of a laser resonator experience a periodic focusing action. The effect on the rays is the same as in a periodic sequence of lenses [15] which can be used as an optical transmission line. A periodic sequence of identical optical systems is schematically indicated in Fig. 2. A single element of the sequence is characterized by its $ABCD$ matrix. The ray transfer through n consecutive elements of the sequence is described by the n th power of this matrix. This can be evaluated by means of Sylvester's theorem

$$\begin{vmatrix} A & B \\ C & D \end{vmatrix}^n = \frac{1}{\sin^n \Theta} \quad (5)$$

$$\begin{vmatrix} A \sin n\Theta - \sin(n-1)\Theta & B \sin n\Theta \\ C \sin n\Theta & D \sin n\Theta - \sin(n-1)\Theta \end{vmatrix}$$

where

$$\cos \Theta = \frac{1}{2}(A + D). \quad (6)$$

Periodic sequences can be classified as either *stable* or *unstable*. Sequences are stable when the trace $(A+D)$ obeys the inequality

$$-1 < \frac{1}{2}(A + D) < 1. \quad (7)$$

Inspection of (5) shows that rays passing through a stable sequence are periodically refocused. For unstable systems, the trigonometric functions in that equation become hyperbolic functions, which indicates that the rays become more and more dispersed the further they pass through the sequence.

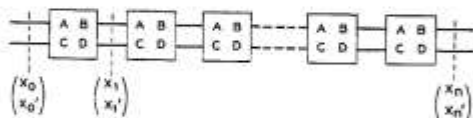


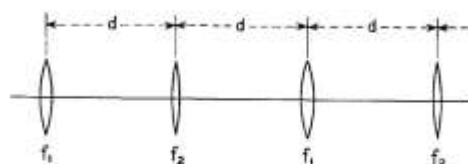
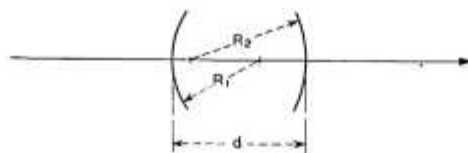
Fig. 2. Periodic sequence of identical systems, each characterized by its $ABCD$ matrix.

2.3 Stability of Laser Resonators

A laser resonator with spherical mirrors of unequal curvature is a typical example of a periodic sequence that can be either stable or unstable [6]. In Fig. 3 such a resonator is shown together with its dual, which is a sequence of lenses. The ray paths through the two structures are the same, except that the ray pattern is folded in the resonator and unfolded in the lens sequence. The focal lengths f_1 and f_2 of the lenses are the same as the focal lengths of the mirrors, i.e., they are determined by the radii of curvature R_1 and R_2 of the mirrors ($f_1 = R_1/2$, $f_2 = R_2/2$). The lens spacings are the same as the mirror spacing d . One can choose, as an element of the periodic sequence, a spacing followed by one lens plus another spacing followed by the second lens. The $ABCD$ matrix of such an element is given in No. 4 of Table I. From this one can obtain the trace, and write the stability condition (7) in the form

$$0 < \left(1 - \frac{d}{R_1}\right) \left(1 - \frac{d}{R_2}\right) < 1. \quad (8)$$

To show graphically which type of resonator is stable and which is unstable, it is useful to plot a stability diagram on which each resonator type is represented by a point. This is shown in Fig. 4 where the parameters d/R_1 and d/R_2 are drawn as the coordinate axes; unstable systems are represented by points in the shaded areas. Various resonator types, as characterized by the relative positions of the centers of curvature of the mirrors, are indicated in the appropriate regions of the diagram. Also entered as alternate coordinate axes are the parameters g_1 and g_2 which play an important role in the diffraction theory of resonators (see Section 4).



$$R_1 = 2f_1, \quad R_2 = 2f_2$$

Fig. 3. Spherical-mirror resonator and the equivalent sequence of lenses.

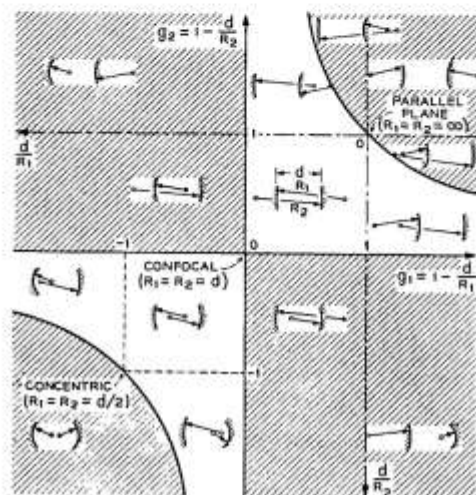


Fig. 4. Stability diagram. Unstable resonator systems lie in shaded regions.

3. WAVE ANALYSIS OF BEAMS AND RESONATORS

In this section the wave nature of laser beams is taken into account, but diffraction effects due to the finite size of apertures are neglected. The latter will be discussed in Section 4. The results derived here are applicable to optical systems with "large apertures," i.e., with apertures that intercept only a negligible portion of the beam power. A theory of light beams or "beam waves" of this kind was first given by Boyd and Gordon [5] and by Goubau and Schwering [7]. The present discussion follows an analysis given in [11].

3.1 Approximate Solution of the Wave Equation

Laser beams are similar in many respects to plane waves; however, their intensity distributions are not uniform, but are concentrated near the axis of propagation and their phase fronts are slightly curved. A field component or potential u of the coherent light satisfies the scalar wave equation

$$\nabla^2 u + k^2 u = 0 \quad (9)$$

where $k = 2\pi/\lambda$ is the propagation constant in the medium.

For light traveling in the z direction one writes

$$u = \psi(x, y, z) \exp(-jkz) \quad (10)$$

where ψ is a slowly varying complex function which represents the differences between a laser beam and a plane wave, namely: a nonuniform intensity distribution, expansion of the beam with distance of propagation, curvature of the phase front, and other differences discussed below. By inserting (10) into (9) one obtains

$$\frac{\partial^2 \psi}{\partial x^2} + \frac{\partial^2 \psi}{\partial y^2} - 2jk \frac{\partial \psi}{\partial z} = 0 \quad (11)$$

where it has been assumed that ψ varies so slowly with z that its second derivative $\partial^2 \psi / \partial z^2$ can be neglected.

The differential equation (11) for ψ has a form similar to the time dependent Schrödinger equation. It is easy to see that

$$\psi = \exp \left\{ -j \left(P + \frac{k}{2q} r^2 \right) \right\} \quad (12)$$

is a solution of (11), where

$$r^2 = x^2 + y^2. \quad (13)$$

The parameter $P(z)$ represents a complex phase shift which is associated with the propagation of the light beam, and $q(z)$ is a complex beam parameter which describes the Gaussian variation in beam intensity with the distance r from the optic axis, as well as the curvature of the phase front which is spherical near the axis. After insertion of (12) into (11) and comparing terms of equal powers in r one obtains the relations

$$q' = 1 \quad (14)$$

and

$$P' = -\frac{j}{q} \quad (15)$$

where the prime indicates differentiation with respect to z . The integration of (14) yields

$$q_2 = q_1 + z \quad (16)$$

which relates the beam parameter q_2 in one plane (output plane) to the parameter q_1 in a second plane (input plane) separated from the first by a distance z .

3.2 Propagation Laws for the Fundamental Mode

A coherent light beam with a Gaussian intensity profile as obtained above is not the only solution of (11), but is perhaps the most important one. This beam is often called the "fundamental mode" as compared to the higher order modes to be discussed later. Because of its importance it is discussed here in greater detail.

For convenience one introduces two real beam parameters R and w related to the complex parameter q by

$$\frac{1}{q} = \frac{1}{R} - j \frac{\lambda}{\pi w^2}. \quad (17)$$

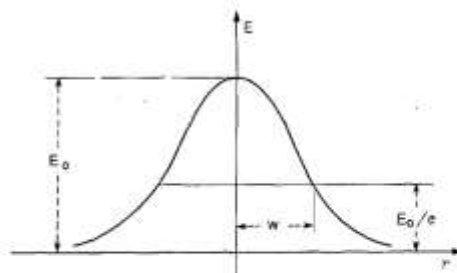


Fig. 5. Amplitude distribution of the fundamental beam.

When (17) is inserted in (12) the physical meaning of these two parameters becomes clear. One sees that $R(z)$ is the radius of curvature of the wavefront that intersects the axis at z , and $w(z)$ is a measure of the decrease of the field amplitude E with the distance from the axis. This decrease is Gaussian in form, as indicated in Fig. 5, and w is the distance at which the amplitude is $1/e$ times that on the axis. Note that the intensity distribution is Gaussian in every beam cross section, and that the width of that Gaussian intensity profile changes along the axis. The parameter w is often called the beam radius or "spot size," and $2w$, the beam diameter.

The Gaussian beam contracts to a minimum diameter $2w_0$ at the beam waist where the phase front is plane. If one measures z from this waist, the expansion laws for the beam assume a simple form. The complex beam parameter at the waist is purely imaginary

$$q_0 = j \frac{\pi w_0^2}{\lambda} \quad (18)$$

and a distance z away from the waist the parameter is

$$q = q_0 + z = j \frac{\pi w_0^2}{\lambda} + z. \quad (19)$$

After combining (19) and (17) one equates the real and imaginary parts to obtain

$$w^2(z) = w_0^2 \left[1 + \left(\frac{\lambda z}{\pi w_0^2} \right)^2 \right] \quad (20)$$

and

$$R(z) = z \left[1 + \left(\frac{\pi w_0^2}{\lambda z} \right)^2 \right]. \quad (21)$$

Figure 6 shows the expansion of the beam according to (20). The beam contour $w(z)$ is a hyperbola with asymptotes inclined to the axis at an angle

$$\theta = \frac{\lambda}{\pi w_0}. \quad (22)$$

This is the far-field diffraction angle of the fundamental mode.

Dividing (21) by (20), one obtains the useful relation

$$\frac{\lambda z}{\pi w_0^2} = \frac{\pi w^2}{\lambda R} \quad (23)$$

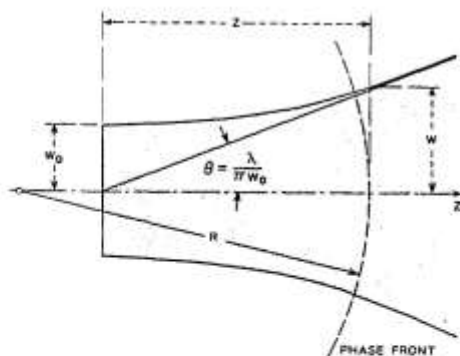


Fig. 6. Contour of a Gaussian beam.

which can be used to express w_0 and z in terms of w and R :

$$w_0^2 = w^2 / \left[1 + \left(\frac{\pi w^2}{\lambda R} \right)^2 \right] \quad (24)$$

$$z = R / \left[1 + \left(\frac{\lambda R}{\pi w^2} \right)^2 \right] \quad (25)$$

To calculate the complex phase shift a distance z away from the waist, one inserts (19) into (15) to get

$$P' = -\frac{j}{q} = -\frac{j}{z + j(\pi w_0^2/\lambda)} \quad (26)$$

Integration of (26) yields the result

$$jP(z) = \ln[1 - j(\lambda z/\pi w_0^2)] \\ = \ln \sqrt{1 + (\lambda z/\pi w_0^2)^2} - j \operatorname{arc} \tan(\lambda z/\pi w_0^2). \quad (27)$$

The real part of P represents a phase shift difference Φ between the Gaussian beam and an ideal plane wave, while the imaginary part produces an amplitude factor w_0/w which gives the expected intensity decrease on the axis due to the expansion of the beam. With these results for the fundamental Gaussian beam, (10) can be written in the form

$$u(r, z) = \frac{w_0}{w} \cdot \exp \left\{ -j(kz - \Phi) - r^2 \left(\frac{1}{w^2} + \frac{jk}{2R} \right) \right\} \quad (28)$$

where

$$\Phi = \operatorname{arc} \tan(\lambda z/\pi w_0^2). \quad (29)$$

It will be seen in Section 3.5 that Gaussian beams of this kind are produced by many lasers that oscillate in the fundamental mode.

3.3 Higher Order Modes

In the preceding section only one solution of (11) was discussed, i.e., a light beam with the property that its intensity profile in every beam cross section is given by the same function, namely, a Gaussian. The width of this Gaussian distribution changes as the beam propagates along its axis. There are other solutions of (11) with sim-

ilar properties, and they are discussed in this section. These solutions form a complete and orthogonal set of functions and are called the "modes of propagation." Every arbitrary distribution of monochromatic light can be expanded in terms of these modes. Because of space limitations the derivation of these modes can only be sketched here.

a) *Modes in Cartesian Coordinates:* For a system with a rectangular (x, y, z) geometry one can try a solution for (11) of the form

$$\psi = g\left(\frac{x}{w}\right) \cdot h\left(\frac{y}{w}\right) \cdot \exp \left\{ -j \left[P + \frac{k}{2q} (x^2 + y^2) \right] \right\} \quad (30)$$

where g is a function of x and z , and h is a function of y and z . For real g and h this postulates mode beams whose intensity patterns scale according to the width $2w(z)$ of a Gaussian beam. After inserting this trial solution into (11) one arrives at differential equations for g and h of the form

$$\frac{d^2 H_m}{dx^2} - 2x \frac{dH_m}{dx} + 2mH_m = 0. \quad (31)$$

This is the differential equation for the Hermite polynomial $H_m(x)$ of order m . Equation (11) is satisfied if

$$g \cdot h = H_m \left(\sqrt{2} \frac{x}{w} \right) H_n \left(\sqrt{2} \frac{y}{w} \right) \quad (32)$$

where m and n are the (transverse) mode numbers. Note that the same pattern scaling parameter $w(z)$ applies to modes of all orders.

Some Hermite polynomials of low order are

$$\begin{aligned} H_0(x) &= 1 \\ H_1(x) &= x \\ H_2(x) &= 4x^2 - 2 \\ H_3(x) &= 8x^3 - 12x. \end{aligned} \quad (33)$$

Expression (28) can be used as a mathematical description of higher order light beams, if one inserts the product $g \cdot h$ as a factor on the right-hand side. The intensity pattern in a cross section of a higher order beam is, thus, described by the product of Hermite and Gaussian functions. Photographs of such mode patterns are shown in Fig. 7. They were produced as modes of oscillation in a gas laser oscillator [16]. Note that the number of zeros in a mode pattern is equal to the corresponding mode number, and that the area occupied by a mode increases with the mode number.

The parameter $R(z)$ in (28) is the same for all modes, implying that the phase-front curvature is the same and changes in the same way for modes of all orders. The phase shift Φ , however, is a function of the mode numbers. One obtains

$$\Phi(m, n; z) = (m + n + 1) \operatorname{arc} \tan(\lambda z/\pi w_0^2). \quad (34)$$

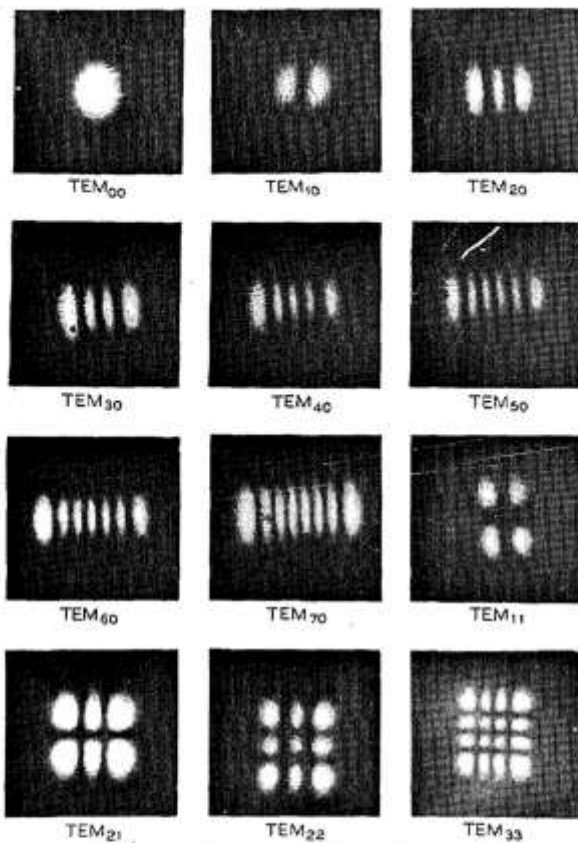


Fig. 7. Mode patterns of a gas laser oscillator (rectangular symmetry).

This means that the phase velocity increases with increasing mode number. In resonators this leads to differences in the resonant frequencies of the various modes of oscillation.

b) *Modes in Cylindrical Coordinates:* For a system with a cylindrical (r, ϕ, z) geometry one uses a trial solution for (11) of the form

$$\psi = g\left(\frac{r}{w}\right) \cdot \exp\left\{-j\left(P + \frac{k}{2q}r^2 + l\phi\right)\right\}. \quad (35)$$

After some calculation one finds

$$g = \left(\sqrt{2} \frac{r}{w}\right)^l \cdot L_p^l\left(2 \frac{r^2}{w^2}\right) \quad (36)$$

where L_p^l is a generalized Laguerre polynomial, and p and l are the radial and angular mode numbers. $L_p^l(x)$ obeys the differential equation

$$x \frac{d^2 L_p^l}{dx^2} + (l+1-x) \frac{dL_p^l}{dx} + pL_p^l = 0. \quad (37)$$

Some polynomials of low order are

$$\begin{aligned} L_0^l(x) &= 1 \\ L_1^l(x) &= l+1-x \\ L_2^l(x) &= \frac{1}{2}(l+1)(l+2) - (l+2)x + \frac{1}{2}x^2. \end{aligned} \quad (38)$$

As in the case of beams with a rectangular geometry, the beam parameters $w(z)$ and $R(z)$ are the same for all cylindrical modes. The phase shift is, again, dependent on the mode numbers and is given by

$$\Phi(p, l; z) = (2p + l + 1) \arctan(\lambda z / \pi w_0^2). \quad (39)$$

3.4 Beam Transformation by a Lens

A lens can be used to focus a laser beam to a small spot, or to produce a beam of suitable diameter and phase-front curvature for injection into a given optical structure. An ideal lens leaves the transverse field distribution of a beam mode unchanged, i.e., an incoming fundamental Gaussian beam will emerge from the lens as a fundamental beam, and a higher order mode remains a mode of the same order after passing through the lens. However, a lens does change the beam parameters $R(z)$ and $w(z)$. As these two parameters are the same for modes of all orders, the following discussion is valid for all orders; the relationship between the parameters of an incoming beam (labeled here with the index 1) and the parameters of the corresponding outgoing beam (index 2) is studied in detail.

An ideal thin lens of focal length f transforms an incoming spherical wave with a radius R_1 immediately to the left of the lens into a spherical wave with the radius R_2 immediately to the right of it, where

$$\frac{1}{R_2} = \frac{1}{R_1} - \frac{1}{f}. \quad (40)$$

Figure 8 illustrates this situation. The radius of curvature is taken to be positive if the wavefront is convex as viewed from $z = \infty$. The lens transforms the phase fronts of laser beams in exactly the same way as those of spherical waves. As the diameter of a beam is the same immediately to the left and to the right of a *thin* lens, the q -parameters of the incoming and outgoing beams are related by

$$\frac{1}{q_2} = \frac{1}{q_1} - \frac{1}{f}, \quad (41)$$

where the q 's are measured at the lens. If q_1 and q_2 are measured at distances d_1 and d_2 from the lens as indicated in Fig. 9, the relation between them becomes

$$q_2 = \frac{(1 - d_2/f)q_1 + (d_1 + d_2 - d_1 d_2/f)}{-(q_1/f) + (1 - d_1/f)}. \quad (42)$$

This formula is derived using (16) and (41).

More complicated optical structures, such as gas lenses, combinations of lenses, or thick lenses, can be thought of as composed of a series of thin lenses at various spacings. Repeated application of (16) and (41) is, therefore, sufficient to calculate the effect of complicated structures on the propagation of laser beams. If the $ABCD$ matrix for the transfer of paraxial rays through the structure is known, the q parameter of the output beam can be calculated from

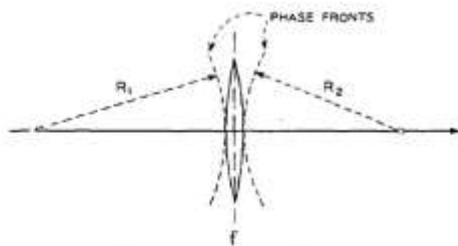


Fig. 8. Transformation of wavefronts by a thin lens.

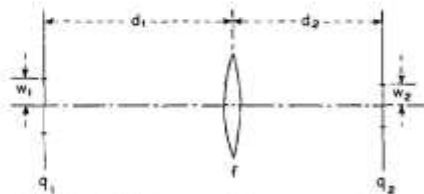


Fig. 9. Distances and parameters for a beam transformed by a thin lens.

$$q_2 = \frac{Aq_1 + B}{Cq_1 + D} \quad (43)$$

This is a generalized form of (42) and has been called the *ABCD* law [10]. The matrices of several optical structures are given in Section II. The *ABCD* law follows from the analogy between the laws for laser beams and the laws obeyed by the spherical waves in geometrical optics. The radius of the spherical waves R obeys laws of the same form as (16) and (41) for the complex beam parameter q . A more detailed discussion of this analogy is given in [11].

3.5 Laser Resonators (Infinite Aperture)

The most commonly used laser resonators are composed of two spherical (or flat) mirrors facing each other. The stability of such "open" resonators has been discussed in Section 2 in terms of paraxial rays. To study the *modes* of laser resonators one has to take account of their wave nature, and this is done here by studying wave beams of the kind discussed above as they propagate back and forth between the mirrors. As aperture diffraction effects are neglected throughout this section, the present discussion applies only to stable resonators with mirror apertures that are large compared to the spot size of the beams.

A mode of a resonator is defined as a self-consistent field configuration. If a mode can be represented by a wave beam propagating back and forth between the mirrors, the beam parameters must be the same after one complete return trip of the beam. This condition is used to calculate the mode parameters. As the beam that represents a mode travels in both directions between the mirrors it forms the axial standing-wave pattern that is expected for a resonator mode.

A laser resonator with mirrors of equal curvature is shown in Fig. 10 together with the equivalent unfolded system, a sequence of lenses. For this symmetrical structure it is sufficient to postulate self-consistency for one transit of the resonator (which is equivalent to one full period of the lens sequence), instead of a complete return

trip. If the complex beam parameter is given by q_1 , immediately to the right of a particular lens, the beam parameter q_2 , immediately to the right of the next lens, can be calculated by means of (16) and (41) as

$$\frac{1}{q_2} = \frac{1}{q_1 + d} - \frac{1}{f} \quad (44)$$

Self-consistency requires that $q_1 = q_2 = q$, which leads to a quadratic equation for the beam parameter q at the lenses (or at the mirrors of the resonator):

$$\frac{1}{q^2} + \frac{1}{fq} + \frac{1}{fd} = 0 \quad (45)$$

The roots of this equation are

$$\frac{1}{q} = -\frac{1}{2f} (\pm) j \sqrt{\frac{1}{fd} - \frac{1}{4f^2}} \quad (46)$$

where only the root that yields a real beamwidth is used. (Note that one gets a real beamwidth for stable resonators only.)

From (46) one obtains immediately the real beam parameters defined in (17). One sees that R is equal to the radius of curvature of the mirrors, which means that the mirror surfaces are coincident with the phase fronts of the resonator modes. The width $2w$ of the fundamental mode is given by

$$w^2 = \left(\frac{\lambda R}{\pi}\right) / \sqrt{2 \frac{R}{d} - 1} \quad (47)$$

To calculate the beam radius w_0 in the center of the resonator where the phase front is plane, one uses (23) with $z = d/2$ and gets

$$w_0^2 = \frac{\lambda}{2\pi} \sqrt{d(2R - d)} \quad (48)$$

The beam parameters R and w describe the modes of all orders. But the phase velocities are different for the different orders, so that the resonant conditions depend on the mode numbers. Resonance occurs when the phase shift from one mirror to the other is a multiple of π . Using (28) and (34) this condition can be written as

$$kd - 2(m + n + 1) \arctan(\lambda d / 2\pi w_0^2) = \pi(q + 1) \quad (49)$$

where q is the number of nodes of the axial standing-wave pattern (the number of half wavelengths is $q+1$),¹ and m and n are the rectangular mode numbers defined in Section 3.3. For the modes of circular geometry one obtains a similar condition where $(2p+l+1)$ replaces $(m+n+1)$.

The fundamental beat frequency ν_0 , i.e., the frequency spacing between successive longitudinal resonances, is given by

$$\nu_0 = c/2d \quad (50)$$

¹ This q is not to be confused with the complex beam parameter.

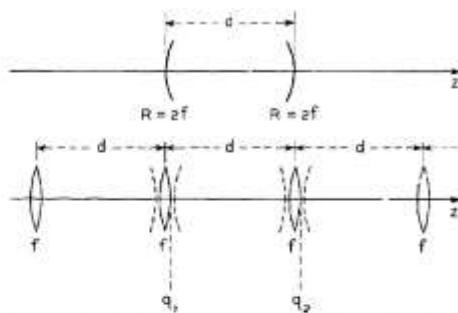


Fig. 10. Symmetrical laser resonator and the equivalent sequence of lenses. The beam parameters, q_1 and q_2 , are indicated.

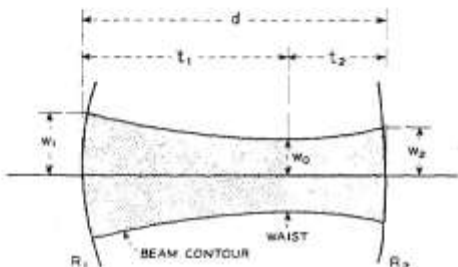


Fig. 11. Mode parameters of interest for a resonator with mirrors of unequal curvature.

where c is the velocity of light. After some algebraic manipulations one obtains from (49) the following formula for the resonant frequency ν of a mode

$$\nu/\nu_0 = (q+1) + \frac{1}{\pi} (m+n+1) \arccos(1-d/R). \quad (51)$$

For the special case of the confocal resonator ($d=R=b$), the above relations become

$$w^2 = \lambda b/\pi, \quad w_0^2 = \lambda b/2\pi; \\ \nu/\nu_0 = (q+1) + \frac{1}{2}(m+n+1). \quad (52)$$

The parameter b is known as the confocal parameter.

Resonators with mirrors of unequal curvature can be treated in a similar manner. The geometry of such a resonator where the radii of curvature of the mirrors are R_1 and R_2 is shown in Fig. 11. The diameters of the beam at the mirrors of a stable resonator, $2w_1$ and $2w_2$, are given by

$$w_1^4 = (\lambda R_1/\pi)^2 \frac{R_2 - d}{R_1 - d} \frac{d}{R_1 + R_2 - d} \\ w_2^4 = (\lambda R_2/\pi)^2 \frac{R_1 - d}{R_2 - d} \frac{d}{R_1 + R_2 - d}. \quad (53)$$

The diameter of the beam waist $2w_0$, which is formed either inside or outside the resonator, is given by

$$w_0^4 = \left(\frac{\lambda}{\pi}\right)^2 \frac{d(R_1 - d)(R_2 - d)(R_1 + R_2 - d)}{(R_1 + R_2 - 2d)^2}. \quad (54)$$

The distances t_1 and t_2 between the waist and the mirrors, measured positive as shown in the figure, are

$$t_1 = \frac{d(R_2 - d)}{R_1 + R_2 - 2d} \\ t_2 = \frac{d(R_1 - d)}{R_1 + R_2 - 2d}. \quad (55)$$

The resonant condition is

$$\nu/\nu_0 = (q+1) + \frac{1}{\pi} (m+n+1) \\ \arccos \sqrt{(1-d/R_1)(1-d/R_2)} \quad (56)$$

where the square root should be given the sign of $(1-d/R_1)$, which is equal to the sign of $(1-d/R_2)$ for a stable resonator.

There are more complicated resonator structures than the ones discussed above. In particular, one can insert a lens or several lenses between the mirrors. But in every case, the unfolded resonator is equivalent to a periodic sequence of identical optical systems as shown in Fig. 2. The elements of the $ABCD$ matrix of this system can be used to calculate the mode parameters of the resonator. One uses the $ABCD$ law (43) and postulates self-consistency by putting $q_1 = q_2 = q$. The roots of the resulting quadratic equation are

$$\frac{1}{q} = \frac{D-A}{2B} \pm \frac{j}{2B} \sqrt{4-(A+D)^2}, \quad (57)$$

which yields, for the corresponding beam radius w ,

$$w^2 = (2\lambda B/\pi) / \sqrt{4-(A+D)^2}. \quad (58)$$

3.6 Mode Matching

It was shown in the preceding section that the modes of laser resonators can be characterized by light beams with certain properties and parameters which are defined by the resonator geometry. These beams are often injected into other optical structures with different sets of beam parameters. These optical structures can assume various physical forms, such as resonators used in scanning Fabry-Perot interferometers or regenerative amplifiers, sequences of dielectric or gas lenses used as optical transmission lines, or crystals of nonlinear dielectric material employed in parametric optics experiments. To match the modes of one structure to those of another one must transform a given Gaussian beam (or higher order mode) into another beam with prescribed properties. This transformation is usually accomplished with a thin lens, but other more complex optical systems can be used. Although the present discussion is devoted to the simple case of the thin lens, it is also applicable to more complex systems, provided one measures the distances from the principal planes and uses the combined focal length f of the more complex system.

The location of the waists of the two beams to be transformed into each other and the beam diameters at the waists are usually known or can be computed. To match the beams one has to choose a lens of a focal length

f that is larger than a characteristic length f_0 defined by the two beams, and one has to adjust the distances between the lens and the two beam waists according to rules derived below.

In Fig. 9 the two beam waists are assumed to be located at distances d_1 and d_2 from the lens. The complex beam parameters at the waists are purely imaginary; they are

$$q_1 = j\pi w_1^2/\lambda, \quad q_2 = j\pi w_2^2/\lambda \quad (59)$$

where $2w_1$ and $2w_2$ are the diameters of the two beams at their waists. If one inserts these expressions for q_1 and q_2 into (42) and equates the imaginary parts, one obtains

$$\frac{d_1 - f}{d_2 - f} = \frac{w_1^2}{w_2^2} \quad (60)$$

Equating the real parts results in

$$(d_1 - f)(d_2 - f) = f^2 - f_0^2 \quad (61)$$

where

$$f_0 = \pi w_1 w_2 / \lambda \quad (62)$$

Note that the characteristic length f_0 is defined by the waist diameters of the beams to be matched. Except for the term f_0^2 , which goes to zero for infinitely small wavelengths, (61) resembles Newton's imaging formula of geometrical optics.

Any lens with a focal length $f > f_0$ can be used to perform the matching transformation. Once f is chosen, the distances d_1 and d_2 have to be adjusted to satisfy the matching formulas [10]

$$d_1 = f \pm \frac{w_1}{w_2} \sqrt{f^2 - f_0^2},$$

$$d_2 = f \pm \frac{w_2}{w_1} \sqrt{f^2 - f_0^2} \quad (63)$$

These relations are derived by combining (60) and (61). In (63) one can choose either both plus signs or both minus signs for matching.

It is often useful to introduce the confocal parameters b_1 and b_2 into the matching formulas. They are defined by the waist diameters of the two systems to be matched

$$b_1 = 2\pi w_1^2/\lambda, \quad b_2 = 2\pi w_2^2/\lambda \quad (64)$$

Using these parameters one gets for the characteristic length f_0

$$f_0^2 = \frac{1}{4} b_1 b_2 \quad (65)$$

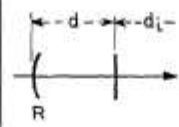
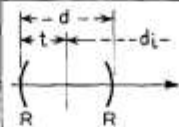
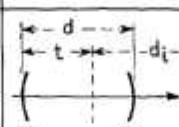
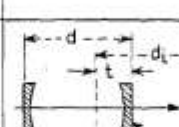
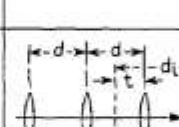
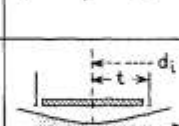
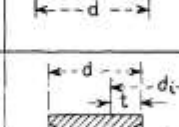
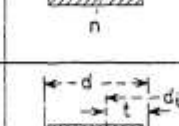
and for the matching distances

$$d_1 = f \pm \frac{1}{2} b_1 \sqrt{(f^2/f_0^2) - 1},$$

$$d_2 = f \pm \frac{1}{2} b_2 \sqrt{(f^2/f_0^2) - 1} \quad (66)$$

Note that in this form of the matching formulas, the wavelength does not appear explicitly.

Table II lists, for quick reference, formulas for the two important parameters of beams that emerge from various

NO	OPTICAL SYSTEM	$\frac{1}{2} b = \pi w_0^2/\lambda$	t
1		$\sqrt{d(R-d)}$	-
2		$\frac{1}{2} \sqrt{d(2R-d)}$	$\frac{1}{2} d$
3		$\frac{\sqrt{d(R_1-d)(R_2-d)(R_1+R_2-d)}}{R_1+R_2-2d}$	$\frac{d(R_2-d)}{R_1+R_2-2d}$
4		$\frac{R \sqrt{d(2R-d)}}{2R+d(n^2-1)}$	$\frac{ndR}{2R+d(n^2-1)}$
5		$\frac{1}{2} \sqrt{d(4f-d)}$	$\frac{1}{2} d$
6		$\frac{1}{2} d$	$\frac{1}{2} d$
7		$\frac{d}{2n}$	$\frac{d}{2n}$
8		$\frac{nR \sqrt{d(2R-d)}}{2n^2R-d(n^2-1)}$	$\frac{dR}{2n^2R-d(n^2-1)}$

optical structures commonly encountered. They are the confocal parameter b and the distance t which gives the waist location of the emerging beam. System No. 1 is a resonator formed by a flat mirror and a spherical mirror of radius R . System No. 2 is a resonator formed by two equal spherical mirrors. System No. 3 is a resonator formed by mirrors of unequal curvature. System No. 4

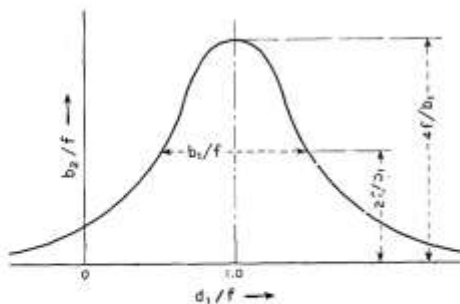


Fig. 12. The confocal parameter b_2 as a function of the lens-waist spacing d_1 .

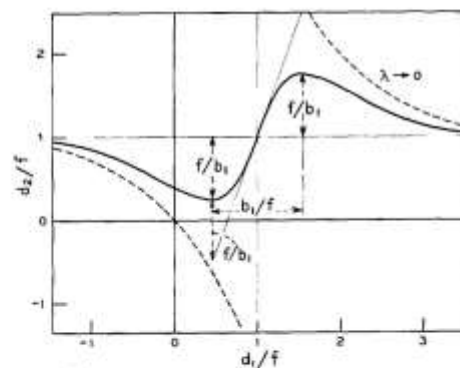


Fig. 13. The waist spacing d_2 as a function of the lens-waist spacing d_1 .

is, again, a resonator formed by two equal spherical mirrors, but with the reflecting surfaces deposited on plano-concave optical plates of index n . These plates act as negative lenses and change the characteristics of the emerging beam. This lens effect is assumed not present in Systems Nos. 2 and 3. System No. 5 is a sequence of thin lenses of equal focal lengths f . System No. 6 is a system of two irises with equal apertures spaced at a distance d . Shown are the parameters of a beam that will pass through both irises with the least possible beam diameter. This is a beam which is "confocal" over the distance d . This beam will also pass through a tube of length d with the optimum clearance. (The tube is also indicated in the figure.) A similar situation is shown in System No. 7, which corresponds to a beam that is confocal over the length d of optical material of index n . System No. 8 is a spherical mirror resonator filled with material of index n , or an optical material with curved end surfaces where the beam passing through it is assumed to have phase fronts that coincide with these surfaces.

When one designs a matching system, it is useful to know the accuracy required of the distance adjustments. The discussion below indicates how the parameters b_2 and d_2 change when b_1 and f are fixed and the lens spacing d_1 to the waist of the input beam is varied. Equations (60) and (61) can be solved for b_2 with the result [9]

$$b_2/f = \frac{b_1/f}{(1 - d_1/f)^2 + (b_1/2f)^2} \quad (67)$$

This means that the parameter b_2 of the beam emerging from the lens changes with d_1 according to a Lorentzian functional form as shown in Fig. 12. The Lorentzian is centered at $d_1=f$ and has a width of b_1 . The maximum value of b_2 is $4f^2/b_1$.

If one inserts (67) into (60) one gets

$$1 - d_2/f = \frac{1 - d_1/f}{(1 - d_1/f)^2 + (b_1/2f)^2} \quad (68)$$

which shows the change of d_2 with d_1 . The change is reminiscent of a dispersion curve associated with a Lorentzian as shown in Fig. 13. The extrema of this curve occur at the halfpower points of the Lorentzian. The slope of the curve at $d_1=f$ is $(2f/b_1)^2$. The dashed curves in the figure correspond to the geometrical optics imaging relation between d_1 , d_2 , and f [20].

3.7 Circle Diagrams

The propagation of Gaussian laser beams can be represented graphically on a circle diagram. On such a diagram one can follow a beam as it propagates in free space or passes through lenses, thereby affording a graphic solution of the mode matching problem. The circle diagrams for beams are similar to the impedance charts, such as the Smith chart. In fact there is a close analogy between transmission-line and laser-beam problems, and there are analog electric networks for every optical system [17].

The first circle diagram for beams was proposed by Collins [18]. A dual chart was discussed in [19]. The basis for the derivation of these charts are the beam propagation laws discussed in Section 3.2. One combines (17) and (19) and eliminates q to obtain

$$\left(\frac{\lambda}{\pi w^2} + j \frac{1}{R}\right) \left(\frac{\pi w_0^2}{\lambda} - jz\right) = 1. \quad (69)$$

This relation contains the four quantities w , R , w_0 , and z which were used to describe the propagation of Gaussian beams in Section 3.2. Each pair of these quantities can be expressed in complex variables W and Z :

$$W = \frac{\lambda}{\pi w^2} + j \frac{1}{R}$$

$$Z = \frac{\pi w_0^2}{\lambda} - jz = b/2 - jz, \quad (70)$$

where b is the confocal parameter of the beam. For these variables (69) defines a conformal transformation

$$W = 1/Z. \quad (71)$$

The two dual circle diagrams are plotted in the complex planes of W and Z , respectively. The W -plane diagram [18] is shown in Fig. 14 where the variables $\lambda/\pi w^2$ and $1/R$ are plotted as axes. In this plane the lines of constant $b/2 = \pi w_0^2/\lambda$ and the lines of constant z of the Z plane appear as circles through the origin. A beam is represented by a circle of constant b , and the beam parameters w and R at a distance z from the beam waist can be easily read

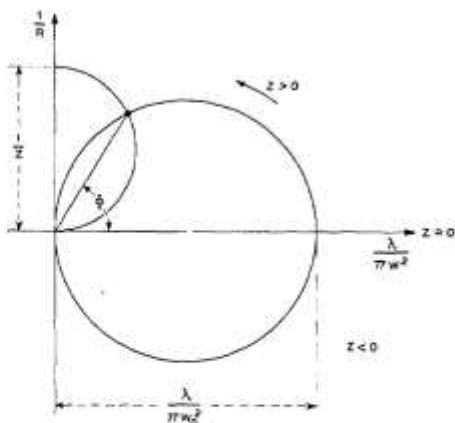


Fig. 14. Geometry for the W -plane circle diagram.

such transformation makes it possible to use the Smith chart for determining complex mismatch coefficients for Gaussian beams [20]. Other circle diagrams include those for optical resonators [21] which allow the graphic determination of certain parameters of the resonator modes.

4. LASER RESONATORS (FINITE APERTURE)

4.1 General Mathematical Formulation

In this section aperture diffraction effects due to the finite size of the mirrors are taken into account; these effects were neglected in the preceding sections. There, it was mentioned that resonators used in laser oscillators usually take the form of an open structure consisting of a pair of mirrors facing each other. Such a structure with finite mirror apertures is intrinsically lossy and, unless energy is supplied to it continuously, the electromagnetic field in it will decay. In this case a mode of the resonator is a *slowly decaying* field configuration whose relative distribution does not change with time [4]. In a laser oscillator the active medium supplies enough energy to overcome the losses so that a steady-state field can exist. However, because of nonlinear gain saturation the medium will exhibit less gain in those regions where the field is high than in those where the field is low, and so the oscillating modes of an active resonator are expected to be somewhat different from the decaying modes of the passive resonator. The problem of an active resonator filled with a saturable-gain medium has been solved recently [22], [23], and the computed results show that if the gain is not too large the resonator modes are essentially unperturbed by saturation effects. This is fortunate as the results which have been obtained for the passive resonator can also be used to describe the active modes of laser oscillators.

The problem of the open resonator is a difficult one and a rigorous solution is yet to be found. However, if certain simplifying assumptions are made, the problem becomes tractable and physically meaningful results can be obtained. The simplifying assumptions involve essentially the quasi-optic nature of the problem; specifically, they are 1) that the dimensions of the resonator are large compared to the wavelength and 2) that the field in the resonator is substantially transverse electromagnetic (TEM). So long as those assumptions are valid, the Fresnel-Kirchhoff formulation of Huygens' principle can be invoked to obtain a pair of integral equations which relate the fields of the two opposing mirrors. Furthermore, if the mirror separation is large compared to mirror dimensions and if the mirrors are only slightly curved, the two orthogonal Cartesian components of the vector field are essentially uncoupled, so that separate scalar equations can be written for each component. The solutions of these scalar equations yield resonator modes which are uniformly polarized in one direction. Other polarization configurations can be constructed from the uniformly polarized modes by linear superposition.

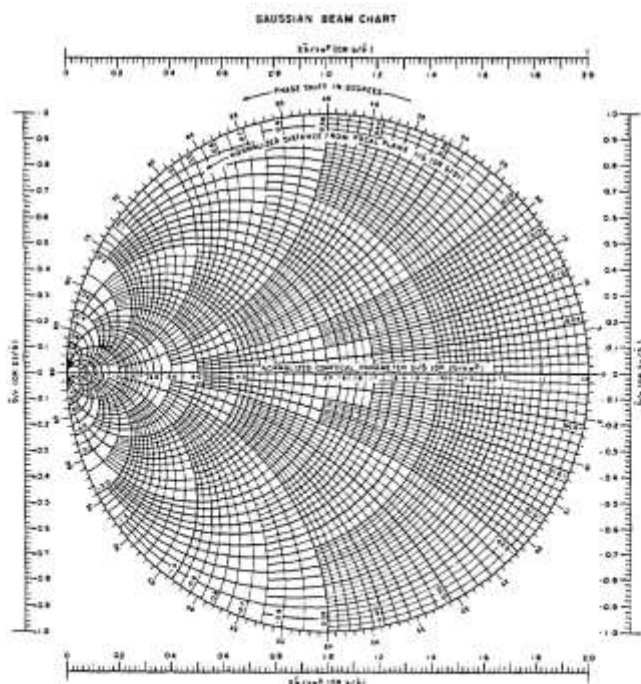


Fig. 15. The Gaussian beam chart. Both W -plane and Z -plane circle diagram are combined into one.

from the diagram. When the beam passes through a lens the phase front is changed according to (40) and a new beam is formed, which implies that the incoming and outgoing beams are connected in the diagram by a vertical line of length $1/f$. The angle ϕ shown in the figure is equal to the phase shift experienced by the beam as given by (29); this is easily shown using (23).

The dual diagram [19] is plotted in the Z plane. The sets of circles in both diagrams have the same form, and only the labeling of the axes and circles is different. In Fig. 15 both diagrams are unified in one chart. The labels in parentheses correspond to the Z -plane diagram, and b is a normalizing parameter which can be arbitrarily chosen for convenience.

One can plot various other circle diagrams which are related to the above by conformal transformations. One

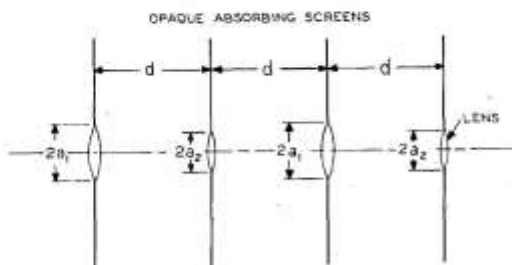
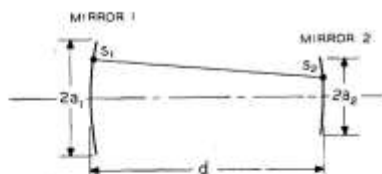


Fig. 16. Geometry of a spherical-mirror resonator with finite mirror apertures and the equivalent sequence of lenses set in opaque absorbing screens.

In deriving the integral equations, it is assumed that a traveling TEM wave is reflected back and forth between the mirrors. The resonator is thus analogous to a transmission medium consisting of apertures or lenses set in opaque absorbing screens (see Fig. 16). The fields at the two mirrors are related by the equations [24]

$$\begin{aligned} \gamma^{(1)} E^{(1)}(s_1) &= \int_{S_2} K^{(2)}(s_1, s_2) E^{(2)}(s_2) dS_2 \\ \gamma^{(2)} E^{(2)}(s_2) &= \int_{S_1} K^{(1)}(s_2, s_1) E^{(1)}(s_1) dS_1 \end{aligned} \quad (72)$$

where the integrations are taken over the mirror surfaces S_2 and S_1 , respectively. In the above equations the subscripts and superscripts one and two denote mirrors one and two; s_1 and s_2 are symbolic notations for transverse coordinates on the mirror surface, e.g., $s_1 = (x_1, y_1)$ and $s_2 = (x_2, y_2)$ or $s_1 = (r_1, \phi_1)$ and $s_2 = (r_2, \phi_2)$; $E^{(1)}$ and $E^{(2)}$ are the relative field distribution functions over the mirrors; $\gamma^{(1)}$ and $\gamma^{(2)}$ give the attenuation and phase shift suffered by the wave in transit from one mirror to the other; the kernels $K^{(1)}$ and $K^{(2)}$ are functions of the distance between s_1 and s_2 and, therefore, depend on the mirror geometry; they are equal [$K^{(1)}(s_2, s_1) = K^{(2)}(s_1, s_2)$] but, in general, are not symmetric [$K^{(1)}(s_2, s_1) \neq K^{(1)}(s_1, s_2)$, $K^{(2)}(s_1, s_2) \neq K^{(2)}(s_2, s_1)$].

The integral equations given by (72) express the field at each mirror in terms of the reflected field at the other; that is, they are single-transit equations. By substituting one into the other, one obtains the double-transit or round-trip equations, which state that the field at each mirror must reproduce itself after a round trip. Since the kernel for each of the double-transit equations is symmetric [24], it follows [25] that the field distribution functions corresponding to the different mode orders are orthogonal over their respective mirror surfaces; that is

$$\begin{aligned} \int_{S_1} E_m^{(1)}(s_1) E_n^{(1)}(s_1) dS_1 &= 0, \quad m \neq n \\ \int_{S_2} E_m^{(2)}(s_2) E_n^{(2)}(s_2) dS_2 &= 0, \quad m \neq n \end{aligned} \quad (73)$$

where m and n denote different mode orders. It is to be noted that the orthogonality relation is non-Hermitian and is the one that is generally applicable to lossy systems.

4.2 Existence of Solutions

The question of the existence of solutions to the resonator integral equations has been the subject of investigation by several authors [26]–[28]. They have given rigorous proofs of the existence of eigenvalues and eigenfunctions for kernels which belong to resonator geometries commonly encountered, such as those with parallel-plane and spherically curved mirrors.

4.3 Integral Equations for Resonators with Spherical Mirrors

When the mirrors are spherical and have rectangular or circular apertures, the two-dimensional integral equations can be separated and reduced to one-dimensional equations which are amenable to solution by either analytical or numerical methods. Thus, in the case of rectangular mirrors [4]–[6], [24], [29], [30], the one-dimensional equations in Cartesian coordinates are the same as those for infinite-strip mirrors; for the x coordinate, they are

$$\begin{aligned} \gamma_z^{(1)} u^{(1)}(x_1) &= \int_{-a_2}^{a_2} K(x_1, x_2) u^{(2)}(x_2) dx_2 \\ \gamma_z^{(2)} u^{(2)}(x_2) &= \int_{-a_1}^{a_1} K(x_1, x_2) u^{(1)}(x_1) dx_1 \end{aligned} \quad (74)$$

where the kernel K is given by

$$\begin{aligned} K(x_1, x_2) &= \sqrt{\frac{j}{\lambda d}} \\ &\cdot \exp \left\{ -\frac{jk}{2d} (g_1 x_1^2 + g_2 x_2^2 - 2x_1 x_2) \right\}. \end{aligned} \quad (75)$$

Similar equations can be written for the y coordinate, so that $E(x, y) = u(x)v(y)$ and $\gamma = \gamma_x \gamma_y$. In the above equation a_1 and a_2 are the half-widths of the mirrors in the x direction, d is the mirror spacing, k is $2\pi/\lambda$, and λ is the wavelength. The radii of curvature of the mirrors R_1 and R_2 are contained in the factors

$$\begin{aligned} g_1 &= 1 - \frac{d}{R_1} \\ g_2 &= 1 - \frac{d}{R_2}. \end{aligned} \quad (76)$$

For the case of circular mirrors [4], [31], [32] the equations are reduced to the one-dimensional form by using

cylindrical coordinates and by assuming a sinusoidal azimuthal variation of the field; that is, $E(r, \phi) = R_l(r)e^{-j\ell\phi}$. The radial distribution functions $R_l^{(1)}$ and $R_l^{(2)}$ satisfy the one-dimensional integral equations:

$$\begin{aligned} \gamma_l^{(1)} R_l^{(1)}(r_1) \sqrt{r_1} &= \int_0^{a_2} K_l(r_1, r_2) R_l^{(2)}(r_2) \sqrt{r_2} dr_2 \\ \gamma_l^{(2)} R_l^{(2)}(r_2) \sqrt{r_2} &= \int_0^{a_1} K_l(r_1, r_2) R_l^{(1)}(r_1) \sqrt{r_1} dr_1 \end{aligned} \quad (77)$$

where the kernel K_l is given by

$$\begin{aligned} K_l(r_1, r_2) &= \frac{j^{\ell+1}}{d} J_\ell \left(k \frac{r_1 r_2}{d} \right) \sqrt{r_1 r_2} \\ &\cdot \exp \left\{ -\frac{j\ell k}{2d} (g_1 r_1^2 + g_2 r_2^2) \right\} \end{aligned} \quad (78)$$

and J_ℓ is a Bessel function of the first kind and ℓ th order. In (77), a_1 and a_2 are the radii of the mirror apertures and d is the mirror spacing; the factors g_1 and g_2 are given by (76).

Except for the special case of the confocal resonator [5] ($g_1 = g_2 = 0$), no exact analytical solution has been found for either (74) or (77), but approximate methods and numerical techniques have been employed with success for their solutions. Before presenting results, it is appropriate to discuss two important properties which apply in general to resonators with spherical mirrors; these are the properties of "equivalence" and "stability."

4.4 Equivalent Resonator Systems

The equivalence properties [24], [33] of spherical-mirror resonators are obtained by simple algebraic manipulations of the integral equations. First, it is obvious that the mirrors can be interchanged without affecting the results; that is, the subscripts and superscripts one and two can be interchanged. Second, the diffraction loss and the intensity pattern of the mode remain invariant if both g_1 and g_2 are reversed in sign; the eigenfunctions E and the eigenvalues γ merely take on complex conjugate values. An example of such equivalent systems is that of parallel-plane ($g_1 = g_2 = 1$) and concentric ($g_1 = g_2 = -1$) resonator systems.

The third equivalence property involves the Fresnel number N and the stability factors G_1 and G_2 , where

$$\begin{aligned} N &= \frac{a_1 a_2}{\lambda d} \\ G_1 &= g_1 \frac{a_1}{a_2} \\ G_2 &= g_2 \frac{a_2}{a_1} \end{aligned} \quad (79)$$

If these three parameters are the same for any two resonators, then they would have the same diffraction loss, the

same resonant frequency, and mode patterns that are scaled versions of each other. Thus, the equivalence relations reduce greatly the number of calculations which are necessary for obtaining the solutions for the various resonator geometries.

4.5 Stability Condition and Diagram

Stability of optical resonators has been discussed in Section 2 in terms of geometrical optics. The stability condition is given by (8). In terms of the stability factors G_1 and G_2 , it is

$$0 < G_1 G_2 < 1$$

or

$$0 < g_1 g_2 < 1. \quad (80)$$

Resonators are stable if this condition is satisfied and unstable otherwise.

A stability diagram [6], [24] for the various resonator geometries is shown in Fig. 4 where g_1 and g_2 are the coordinate axes and each point on the diagram represents a particular resonator geometry. The boundaries between stable and unstable (shaded) regions are determined by (80), which is based on geometrical optics. The fields of the modes in stable resonators are more concentrated near the resonator axes than those in unstable resonators and, therefore, the diffraction losses of unstable resonators are much higher than those of stable resonators. The transition, which occurs near the boundaries, is gradual for resonators with small Fresnel numbers and more abrupt for those with large Fresnel numbers. The origin of the diagram represents the confocal system with mirrors of equal curvature ($R_1 = R_2 = d$) and is a point of lowest diffraction loss for a given Fresnel number. The fact that a system with minor deviations from the ideal confocal system may become unstable should be borne in mind when designing laser resonators.

4.6 Modes of the Resonator

The transverse field distributions of the resonator modes are given by the eigenfunctions of the integral equations. As yet, no exact analytical solution has been found for the general case of arbitrary G_1 and G_2 , but approximate analytical expressions have been obtained to describe the fields in stable spherical-mirror resonators [5], [6]. These approximate eigenfunctions are the same as those of the optical beam modes which are discussed in Section 2; that is, the field distributions are given approximately by Hermite-Gaussian functions for rectangular mirrors [5], [6], [34], and by Laguerre-Gaussian functions for circular mirrors [6], [7]. The designation of the resonator modes is given in Section 3.5. (The modes are designated as TEM_{mnq} for rectangular mirrors and $TEM_{p\ell q}$ for circular mirrors.) Figure 7 shows photographs of some of the rectangular mode patterns of a

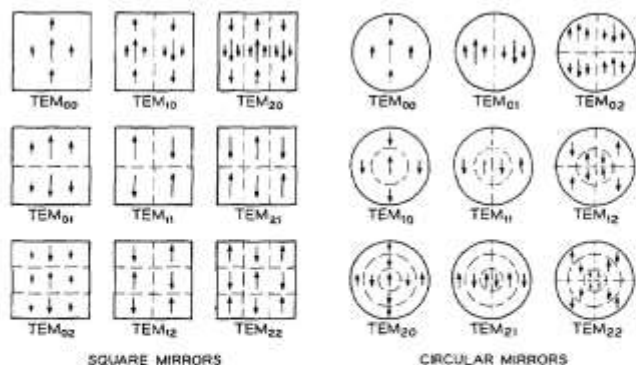


Fig. 17. Linearly polarized resonator mode configurations for square and circular mirrors.

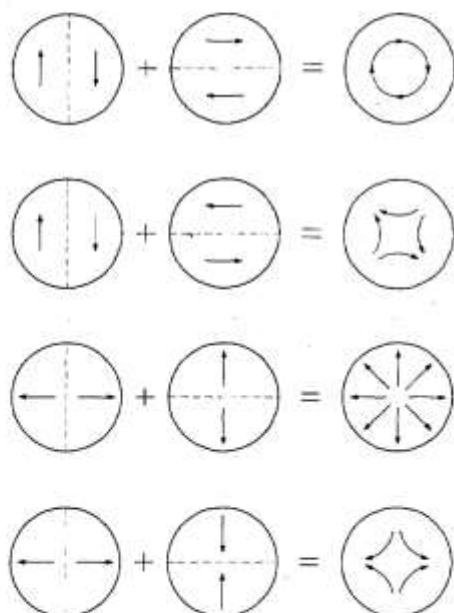


Fig. 18. Synthesis of different polarization configurations from the linearly polarized TEM_{01} mode.

laser. Linearly polarized mode configurations for square mirrors and for circular mirrors are shown in Fig. 17. By combining two orthogonally polarized modes of the same order, it is possible to synthesize other polarization configurations; this is shown in Fig. 18 for the TEM_{01} mode.

Field distributions of the resonator modes for any value of G could be obtained numerically by solving the integral equations either by the method of successive approximations [4], [24], [31] or by the method of kernel expansion [30], [32]. The former method of solution is equivalent to calculating the transient behavior of the resonator when it is excited initially with a wave of arbitrary distribution. This wave is assumed to travel back and forth between the mirrors of the resonator, undergoing changes from transit to transit and losing energy by diffraction. After many transits a quasi steady-state condition is attained where the fields for successive transits

differ only by a constant multiplicative factor. This steady-state relative field distribution is then an eigenfunction of the integral equations and is, in fact, the field distribution of the mode that has the lowest diffraction loss for the symmetry assumed (e.g., for even or odd symmetry in the case of infinite-strip mirrors, or for a given azimuthal mode index number l in the case of circular mirrors); the constant multiplicative factor is the eigenvalue associated with the eigenfunction and gives the diffraction loss and the phase shift of the mode. Although this simple form of the iterative method gives only the lower order solutions, it can, nevertheless, be modified to yield higher order ones [24], [35]. The method of kernel expansion, however, is capable of yielding both low-order and high-order solutions.

Figures 19 and 20 show the relative field distributions of the TEM_{00} and TEM_{01} modes for a resonator with a pair of identical, circular mirrors ($N=1$, $a_1=a_2$, $g_1=g_2=g$) as obtained by the numerical iterative method. Several curves are shown for different values of g , ranging from zero (confocal) through one (parallel-plane) to 1.2 (convex, unstable). By virtue of the equivalence property discussed in Section 4.4, the curves are also applicable to resonators with their g values reversed in sign, provided the sign of the ordinate for the phase distribution is also reversed. It is seen that the field is most concentrated near the resonator axis for $g=0$ and tends to spread out as $|g|$ increases. Therefore, the diffraction loss is expected to be the least for confocal resonators.

Figure 21 shows the relative field distributions of some of the low order modes of a Fabry-Perot resonator with (parallel-plane) circular mirrors ($N=10$, $a_1=a_2$, $g_1=g_2=1$) as obtained by a modified numerical iterative method [35]. It is interesting to note that these curves are not very smooth but have small wiggles on them, the number of which are related to the Fresnel number. These wiggles are entirely absent for the confocal resonator and appear when the resonator geometry is unstable or nearly unstable. Approximate expressions for the field distributions of the Fabry-Perot resonator modes have also been obtained by various analytical techniques [36], [37]. They are represented to first order, by sine and cosine functions for infinite-strip mirrors and by Bessel functions for circular mirrors.

For the special case of the confocal resonator ($g_1=g_2=0$), the eigenfunctions are self-reciprocal under the finite Fourier (infinite-strip mirrors) or Hankel (circular mirrors) transformation and exact analytical solutions exist [5], [38]-[40]. The eigenfunctions for infinite-strip mirrors are given by the prolate spheroidal wave functions and, for circular mirrors, by the generalized prolate spheroidal or hyperspheroidal wave functions. For large Fresnel numbers these functions can be closely approximated by Hermite-Gaussian and Laguerre-Gaussian functions which are the eigenfunctions for the beam modes.

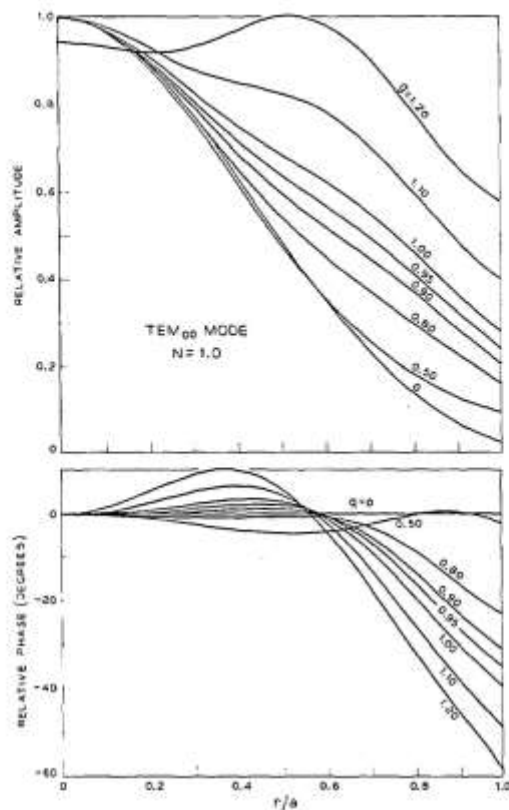


Fig. 19. Relative field distributions of the TEM_{00} mode for a resonator with circular mirrors ($N=1$).

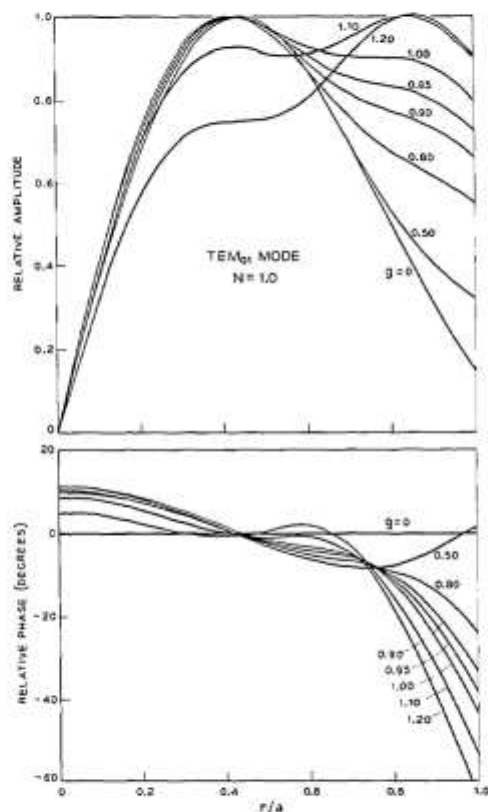


Fig. 20. Relative field distributions of the TEM_{01} mode for a resonator with circular mirrors ($N=1$).

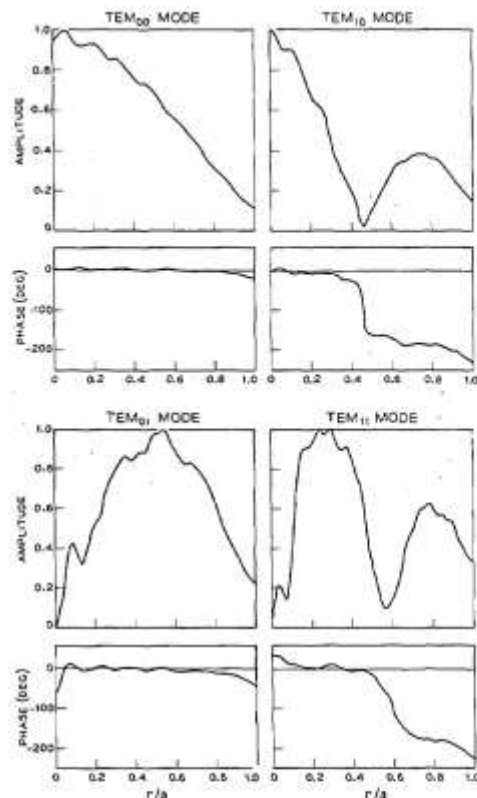


Fig. 21. Relative field distributions of four of the low order modes of a Fabry-Perot resonator with (parallel-plane) circular mirrors ($N=10$).

4.7 Diffraction Losses and Phase Shifts

The diffraction loss α and the phase shift β for a particular mode are important quantities in that they determine the Q and the resonant frequency of the resonator for that mode. The diffraction loss is given by

$$\alpha = 1 - |\gamma|^2 \quad (81)$$

which is the fractional energy lost per transit due to diffraction effects at the mirrors. The phase shift is given by

$$\beta = \text{angle of } \gamma \quad (82)$$

which is the phase shift suffered (or enjoyed) by the wave in transit from one mirror to the other, in addition to the geometrical phase shift which is given by $2\pi d/\lambda$. The eigenvalue γ in (81) and (82) is the appropriate γ for the mode under consideration. If the total resonator loss is small, the Q of the resonator can be approximated by

$$Q = \frac{2\pi d}{\lambda \alpha_t} \quad (83)$$

where α_t , the total resonator loss, includes losses due to diffraction, output coupling, absorption, scattering, and other effects. The resonant frequency ν is given by

$$\nu/\nu_0 = (q + 1) + \beta/\pi \quad (84)$$

where q , the longitudinal mode order, and ν_0 , the fundamental beat frequency, are defined in Section 3.5.

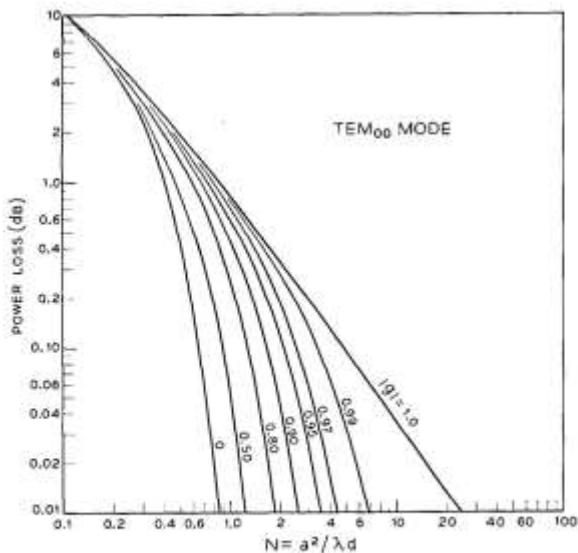


Fig. 22. Diffraction loss per transit (in decibels) for the TEM_{00} mode of a stable resonator with circular mirrors.

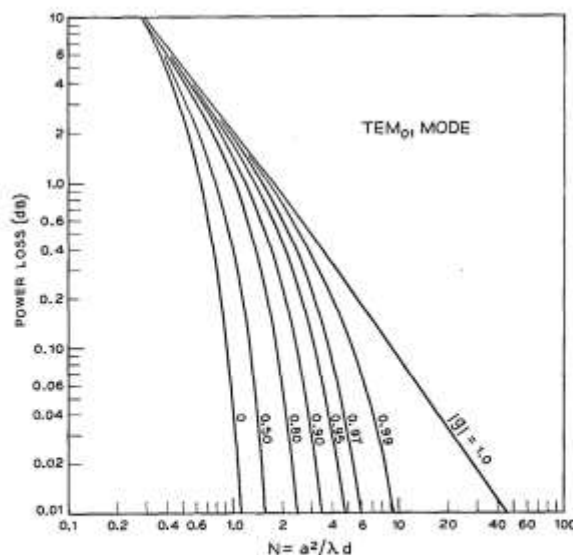


Fig. 23. Diffraction loss per transit (in decibels) for the TEM_{01} mode of a stable resonator with circular mirrors.

The diffraction losses for the two lowest order (TEM_{00} and TEM_{01}) modes of a stable resonator with a pair of identical, circular mirrors ($a_1 = a_2$, $g_1 = g_2 = g$) are given in Figs. 22 and 23 as functions of the Fresnel number N and for various values of g . The curves are obtained by solving (77) numerically using the method of successive approximations [31]. Corresponding curves for the phase shifts are shown in Figs. 24 and 25. The horizontal portions of the phase shift curves can be calculated from the formula

$$\begin{aligned} \beta &= (2p + l + 1) \arccos \sqrt{g_1 g_2} \\ &= (2p + l + 1) \arccos g, \quad \text{for } g_1 = g_2 \end{aligned} \quad (85)$$

which is equal to the phase shift for the beam modes derived in Section 3.5. It is to be noted that the loss curves are applicable to both positive and negative values of g

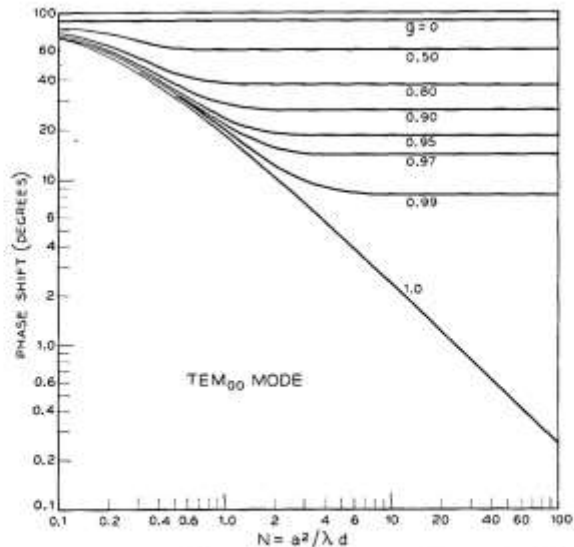


Fig. 24. Phase shift per transit for the TEM_{00} mode of a stable resonator with circular mirrors.

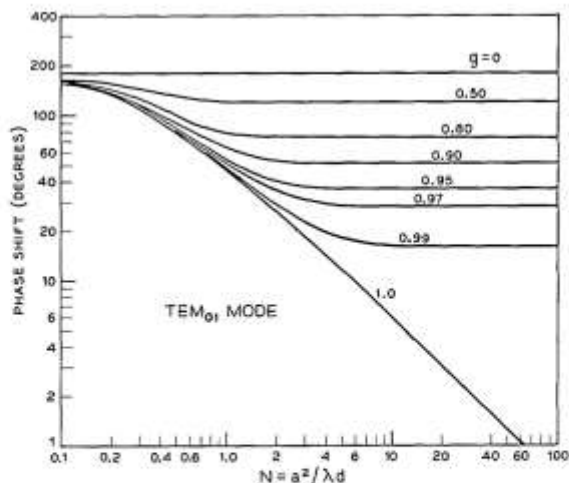


Fig. 25. Phase shift per transit for the TEM_{01} mode of a stable resonator with circular mirrors.

while the phase-shift curves are for positive g only; the phase shift for negative g is equal to 180 degrees minus that for positive g .

Analytical expressions for the diffraction loss and the phase shift have been obtained for the special cases of parallel-plane ($g = 1.0$) and confocal ($g = 0$) geometries when the Fresnel number is either very large (small diffraction loss) or very small (large diffraction loss) [36], [38], [39], [41], [42]. In the case of the parallel-plane resonator with circular mirrors, the approximate expressions valid for large N , as derived by Vainshtein [36], are

$$\alpha = 8\kappa_{pt} \frac{\delta(M + \delta)}{[(M + \delta)^2 + \delta^2]^2} \quad (86)$$

$$\beta = \left(\frac{M}{4\delta}\right) \alpha \quad (87)$$

where $\delta=0.824$, $M=\sqrt{8\pi N}$, and κ_{pl} is the $(p+1)$ th zero of the Bessel function of order l . For the confocal resonator with circular mirrors, the corresponding expressions are [39]

$$\alpha = \frac{2\pi(8\pi N)^{2p+l+1}e^{-4\pi N}}{p!(p+l+1)!} \left[1 + O\left(\frac{1}{2\pi N}\right) \right] \quad (88)$$

$$\beta = (2p+l+1) \frac{\pi}{2} \quad (89)$$

Similar expressions exist for resonators with infinite-strip or rectangular mirrors [36], [39]. The agreement between the values obtained from the above formulas and those from numerical methods is excellent.

The loss of the lowest order (TEM₀₀) mode of an unstable resonator is, to first order, independent of the mirror size or shape. The formula for the loss, which is based on geometrical optics, is [12]

$$\alpha = 1 \pm \frac{1 - \sqrt{1 - (g_1 g_2)^{-1}}}{1 + \sqrt{1 - (g_1 g_2)^{-1}}} \quad (90)$$

where the plus sign in front of the fraction applies for g values lying in the first and third quadrants of the stability diagram, and the minus sign applies in the other two quadrants. Loss curves (plotted vs. N) obtained by solving the integral equations numerically have a ripply behavior which is attributable to diffraction effects [24], [43]. However, the average values agree well with those obtained from (90).

5. CONCLUDING REMARKS

Space limitations made it necessary to concentrate the discussion of this article on the basic aspects of laser beams and resonators. It was not possible to include such interesting topics as perturbations of resonators, resonators with tilted mirrors, or to consider in detail the effect of nonlinear, saturating host media. Also omitted was a discussion of various resonator structures other than those formed of spherical mirrors, e.g., resonators with corner cube reflectors, resonators with output holes, or fiber resonators. Another important, but omitted, field is that of mode selection where much research work is currently in progress. A brief survey of some of these topics is given in [44].

REFERENCES

- [1] R. H. Dicke, "Molecular amplification and generation systems and methods," U. S. Patent 2 851 652, September 9, 1958.
- [2] A. M. Prokhorov, "Molecular amplifier and generator for submillimeter waves," *JETP (USSR)*, vol. 34, pp. 1658-1659, June 1958; *Sov. Phys. JETP*, vol. 7, pp. 1140-1141, December 1958.
- [3] A. L. Schawlow and C. H. Townes, "Infrared and optical masers," *Phys. Rev.*, vol. 29, pp. 1940-1949, December 1958.
- [4] A. G. Fox and T. Li, "Resonant modes in an optical maser," *Proc. IRE (Correspondence)*, vol. 48, pp. 1904-1905, November 1960; "Resonant modes in a maser interferometer," *Bell Sys. Tech. J.*, vol. 40, pp. 453-488, March 1961.
- [5] G. D. Boyd and J. P. Gordon, "Confocal multimode resonator for millimeter through optical wavelength masers," *Bell Sys. Tech. J.*, vol. 40, pp. 489-508, March 1961.
- [6] G. D. Boyd and H. Kogelnik, "Generalized confocal resonator theory," *Bell Sys. Tech. J.*, vol. 41, pp. 1347-1369, July 1962.

- [7] G. Goubau and F. Schermer, "On the guided propagation of electromagnetic wave beams," *IRE Trans. on Antennas and Propagation*, vol. AP-9, pp. 248-256, May 1961.
- [8] J. R. Pierce, "Modes in sequences of lenses," *Proc. Nat'l Acad. Sci.*, vol. 47, pp. 1808-1813, November 1961.
- [9] G. Goubau, "Optical relations for coherent wave beams," in *Electromagnetic Theory and Antennas*. New York: Macmillan, 1963, pp. 907-918.
- [10] H. Kogelnik, "Imaging of optical mode—Resonators with internal lenses," *Bell Sys. Tech. J.*, vol. 44, pp. 455-494, March 1965.
- [11] —, "On the propagation of Gaussian beams of light through lenslike media including those with a loss or gain variation," *Appl. Opt.*, vol. 4, pp. 1562-1569, December 1965.
- [12] A. E. Siegman, "Unstable optical resonators for laser applications," *Proc. IEEE*, vol. 53, pp. 277-287, March 1965.
- [13] W. Brower, *Matrix Methods in Optical Instrument Design*. New York: Benjamin, 1964. E. L. O'Neill, *Introduction to Statistical Optics*. Reading, Mass.: Addison-Wesley, 1963.
- [14] M. Bertolotti, "Matrix representation of geometrical properties of laser cavities," *Nuovo Cimento*, vol. 32, pp. 1242-1257, June 1964. V. P. Bykov and L. A. Vainshtein, "Geometrical optics of open resonators," *JETP (USSR)*, vol. 47, pp. 508-517, August 1964. B. Macke, "Laser cavities in geometrical optics approximation," *J. Phys. (Paris)*, vol. 26, pp. 104A-112A, March 1965. W. K. Kahn, "Geometric optical derivation of formula for the variation of the spot size in a spherical mirror resonator," *Appl. Opt.*, vol. 4, pp. 758-759, June 1965.
- [15] J. R. Pierce, *Theory and Design of Electron Beams*. New York: Van Nostrand, 1954, p. 194.
- [16] H. Kogelnik and W. W. Rigrod, "Visual display of isolated optical-resonator modes," *Proc. IRE (Correspondence)*, vol. 50, p. 220, February 1962.
- [17] G. A. Deschamps and P. E. Mast, "Beam tracing and applications," in *Proc. Symposium on Quasi-Optics*. New York: Polytechnic Press, 1964, pp. 379-395.
- [18] S. A. Collins, "Analysis of optical resonators involving focusing elements," *Appl. Opt.*, vol. 3, pp. 1263-1275, November 1964.
- [19] T. Li, "Dual forms of the Gaussian beam chart," *Appl. Opt.*, vol. 3, pp. 1315-1317, November 1964.
- [20] T. S. Chu, "Geometrical representation of Gaussian beam propagation," *Bell Sys. Tech. J.*, vol. 45, pp. 287-299, February 1966.
- [21] J. P. Gordon, "A circle diagram for optical resonators," *Bell Sys. Tech. J.*, vol. 43, pp. 1826-1827, July 1964. M. J. Offerhaus, "Geometry of the radiation field for a laser interferometer," *Philips Res. Rept.*, vol. 19, pp. 520-523, December 1964.
- [22] H. Statz and C. L. Tang, "Problem of mode deformation in optical masers," *J. Appl. Phys.*, vol. 36, pp. 1816-1819, June 1965.
- [23] A. G. Fox and T. Li, "Effect of gain saturation on the oscillating modes of optical masers," *IEEE J. of Quantum Electronics*, vol. QE-2, p. lxii, April 1966.
- [24] —, "Modes in a maser interferometer with curved and tilted mirrors," *Proc. IEEE*, vol. 51, pp. 80-89, January 1963.
- [25] F. B. Hildebrand, *Methods of Applied Mathematics*. Englewood Cliffs, N. J.: Prentice Hall, 1952, pp. 412-413.
- [26] D. J. Newman and S. P. Morgan, "Existence of eigenvalues of a class of integral equations arising in laser theory," *Bell Sys. Tech. J.*, vol. 43, pp. 113-126, January 1964.
- [27] J. A. Cochran, "The existence of eigenvalues for the integral equations of laser theory," *Bell Sys. Tech. J.*, vol. 44, pp. 77-88, January 1965.
- [28] H. Hochstadt, "On the eigenvalue of a class of integral equations arising in laser theory," *SIAM Rev.*, vol. 8, pp. 62-65, January 1966.
- [29] D. Gloge, "Calculations of Fabry-Perot laser resonators by scattering matrices," *Arch. Elect. Ubertrag.*, vol. 18, pp. 197-203, March 1964.
- [30] W. Streifer, "Optical resonator modes—rectangular reflectors of spherical curvature," *J. Opt. Soc. Am.*, vol. 55, pp. 868-877, July 1965.
- [31] T. Li, "Diffraction loss and selection of modes in maser resonators with circular mirrors," *Bell Sys. Tech. J.*, vol. 44, pp. 917-932, May-June, 1965.
- [32] J. C. Heurtley and W. Streifer, "Optical resonator modes—

circular reflectors of spherical curvature," *J. Opt. Soc. Am.*, vol. 55, pp. 1472-1479, November 1965.

[33] J. P. Gordon and H. Kogelnik, "Equivalence relations among spherical mirror optical resonators," *Bell Sys. Tech. J.*, vol. 43, pp. 2873-2886, November 1964.

[34] F. Schwering, "Reiterative wave beams of rectangular symmetry," *Arch. Elect. Übertrag.*, vol. 15, pp. 555-564, December 1961.

[35] A. G. Fox and T. Li, to be published.

[36] L. A. Vainshtein, "Open resonators for lasers," *JETP (USSR)*, vol. 44, pp. 1050-1067, March 1963; *Sov. Phys. JETP*, vol. 17, pp. 709-719, September 1963.

[37] S. R. Barone, "Resonances of the Fabry-Perot laser," *J. Appl. Phys.*, vol. 34, pp. 831-843, April 1963.

[38] D. Slepian and H. O. Pollak, "Prolate spheroidal wave functions, Fourier analysis and uncertainty—I," *Bell Sys. Tech. J.*, vol. 40, pp. 43-64, January 1961.

[39] D. Slepian, "Prolate spheroidal wave functions, Fourier anal-

ysis and uncertainty—IV: Extensions to many dimensions; generalized prolate spheroidal functions," *Bell Sys. Tech. J.*, vol. 43, pp. 3009-3057, November 1964.

[40] J. C. Heurtley, "Hyperspheroidal functions—optical resonators with circular mirrors," in *Proc. Symposium on Quasi-Optics*. New York: Polytechnic Press, 1964, pp. 367-375.

[41] S. R. Barone and M. C. Newstein, "Fabry-Perot resonances at small Fresnel numbers," *Appl. Opt.*, vol. 3, p. 1194, October 1964.

[42] L. Bergstein and H. Schachter, "Resonant modes of optic cavities of small Fresnel numbers," *J. Opt. Soc. Am.*, vol. 55, pp. 1226-1233, October 1965.

[43] A. G. Fox and T. Li, "Modes in a maser interferometer with curved mirrors," in *Proc. Third International Congress on Quantum Electronics*. New York: Columbia University Press, 1964, pp. 1263-1270.

[44] H. Kogelnik, "Modes in optical resonators," in *Lasers*, A. K. Levine, Ed. New York: Dekker, 1966.

Modes, Phase Shifts, and Losses of Flat-Roof Open Resonators

P. F. CHECCACCI, ANNA CONSORTINI, AND ANNAMARIA SCHEGGI

Abstract—The integral equation of a "flat-roof resonator" is solved by the Fox and Li method of iteration in a number of particular cases.

Mode patterns, phase shifts, and power losses are derived. A good overall agreement is found with the approximate theory previously developed by Toraldo di Francia.

Some experimental tests carried out on a microwave model give a further confirmation of the theoretical predictions.

I. INTRODUCTION

A PARTICULAR type of open resonator terminated by roof reflectors with very small angles, the so-called "flat-roof resonator" (Fig. 1) was recently described by Toraldo di Francia [1].

The mathematical approach consisted in considering the solutions of the wave equation (for the electric or magnetic field) in the two halves of a complete "diamond cavity" whose normal cross section is shown in Fig. 2, ignoring the fact that the reflectors are finite.

The two half-cavities were referred to cylindrical coordinates centered at G and H , respectively, and solutions were given in terms of high-order cylindrical waves. The field in the two half-cavities was matched over the median

Manuscript received May 4, 1966. The research reported here was supported in part by the Air Force Cambridge Research Laboratories through the European Office of Aerospace Research (OAR), U. S. Air Force, under Contract AF 61(052)-871.

The authors are with the Centro Microonde, Consiglio Nazionale delle Ricerche, Florence, Italy.

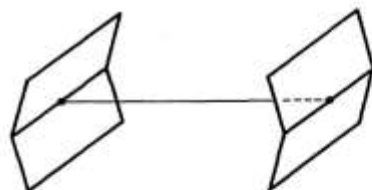


Fig. 1. The flat-roof resonator.

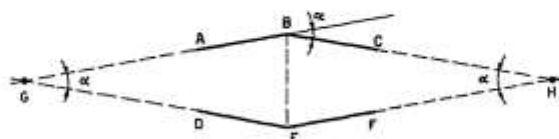


Fig. 2. The diamond cavity.

plane BE by simply requiring that this plane coincide with a node or an antinode. Obviously the α angle of the roof must be so small that the curvature of the nodal or antinodal surfaces can be neglected. Due to the high order of the cylindrical waves, the field in the central region of the cavity approaches the form of a standing wave between the two roof reflectors, while it decays so rapidly from the central region toward the vertices G and H , that the absence of the complete metal walls of the diamond outside the resonator will have very little importance. This treatment, although approximate, allowed the author to understand how the resonator actually worked

SA200-Series Scanning Fabry Perot Interferometer



DESCRIPTION:

The SA200 is a high finesse Spectrum Analyzer used to examine the fine structures of the spectral characteristics of CW lasers. The spectrum analyzer consists of a confocal cavity that contains two high reflectivity mirrors; by varying the mirror separation with a piezoelectric transducer the cavity acts as a very narrow band-pass filter. Knowing the free spectral range of the SA200 allows the time-base of an oscilloscope to be calibrated to facilitate quantitative measurements of a laser line shape.

SPECIFICATIONS:

Free Spectral Range¹ (FSR) Measured in milliseconds:	
FWHM Measured in microseconds:	
(FSR/FWHM)	
Actual Calculated Finesse:	
Maximum Input Voltage:	150V
Free Spectral Range:	1.5GHz
Minimum Finesse:	>200
Resolution:	7.5MHz
Outer Housing Material:	Black Anodized Aluminum
Fabry Perot Cavity Material²:	Low thermal expansion Invar ®
Dimensions:	Ø 2" Flange Total Length: 5.85"

¹ FSR is set by the length of the confocal cavity and is given by: $FSR=c/4d$. Where d= the radius of curvature of the mirrors; in this case d=50mm. (see drawing on next page)

² A thermal design balances the small coefficient of thermal expansion of the Invar body with the negative coefficient of thermal expansion of the piezo actuators.

SA210-Series Scanning Fabry Perot Interferometer



DESCRIPTION:

The SA210 is a high finesse Spectrum Analyzer used to examine the fine structures of the spectral characteristics of CW lasers. The spectrum analyzer consists of a confocal cavity that contains two high reflectivity mirrors; by varying the mirror separation with a piezoelectric transducer the cavity acts as a very narrow band-pass filter. Knowing the free spectral range of the SA210 allows the time-base of an oscilloscope to be calibrated to facilitate quantitative measurements of a laser line shape.

SPECIFICATIONS:

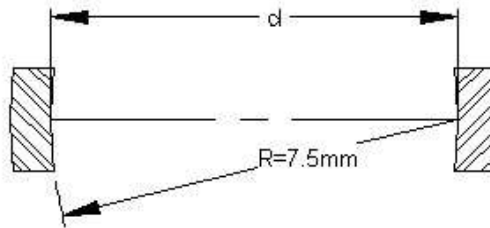
Free Spectral Range¹ (FSR) Measured in milliseconds:	
FWHM Measured in microseconds:	
(FSR/FWHM)	
Actual Calculated Finesse:	

¹ FSR is set by the length of the confocal cavity and is given by: $FSR=c/4d$. Where d = the radius of curvature of the mirrors; in this case $d=7.5\text{mm}$. (see drawing on next page).

Maximum Input Voltage:	150V
Free Spectral Range:	10GHz
Minimum Finesse:	>150
Resolution:	> 67MHz
Outer Housing Material:	Black Anodized Aluminum
Fabry Perot Cavity Material¹:	Low thermal expansion Invar ®
Dimensions:	Ø 1" Flange Total Length: 2.93"

Confocal Cavity Configuration

Mirrors shown below are AR coated on the outer surfaces and HR coated on the inner surfaces.



$$\text{FSR} = c/4d$$

Other mirror sets are available for this instrument:

- 350nm - 535nm
- 535nm - 820nm
- 820nm - 1275nm
- 1275nm - 2000nm
- 1800nm - 2500nm

SETUP:

- Knowing the FSR of the SA210 allows the time-base of an oscilloscope to be calibrated to facilitate quantitative measurements of laser line shape. With a resolution of 67MHz, the fine structure resulting from multiple longitudinal modes of a laser line can be resolved. Note: A saw tooth wave (0-20V) would provide approximately 2 Free Spectral Ranges.
- The SA210 should be mounted, so that it can be easily adjusted. It is recommended that Thorlabs 1inch Kinematic Mount **KM100** be used to mount the interferometer at the 1-inch diameter flange.
- The apparent beam size should be approximately 1mm. It is recommended that a fold mirror be used to direct the beam into the Fabry-Perot interferometer. A lens with focal length of 100mm can be used, with the focus set roughly at the center of the housing, approximately 25mm in from the flange.
- The maximum voltage on the piezo (ramp in) is not to exceed 150V.

¹ A thermal design balances the small coefficient of thermal expansion of the Invar body with the negative coefficient of thermal expansion of the piezo actuators.

- If the detector is connected directly to the scope, a 5kΩ terminator is needed. Offset adjustment (SA201) is used to center the output on the scope.

OPERATION:

To set up the SA210-Series Fabry-Perot you should first mount the unit into a tip/tilt mirror mount (Thorlabs part# KM100). Attach all of the connection according the drawing on page 4. Next you should remove the detector from the back of the unit and mount it in it's own mount, this will aid in the initial alignment. Then close the input iris and center your beam on the iris opening. Leave the back iris completely open and start to scan the unit. Now using the tip/tilt adjustment until the beam is center through the body of the SA210. Adjust the scope gain to maximum sensitivity, position the detector close to the rear opening and slowly close the back iris as you correct the 2 angular adjustments on the mirror mount. Once the beam is centered you can the replace the detector on the main body and start to use the unit for measurements.

OVER VIEW:

Free Spectral Range

To scan the spectra of the laser beam entering the Scanning Fabry-Perot interferometer small displacement is applied to one of the cavity mirror mounted on piezoelectric transducers. This operation is done by fine tuning the ramp voltage applied to the Piezoelectric elements using the controller SA201. When the mirror spacing becomes equal to an integral number of half the wavelength of the laser, constructive interferences occur. That spectral response of the signal can be visualized with a scope. A series of periodical peaks appear on the screen of the scope. The distance between consecutive peaks is called the free spectral range (FSR) of the instrument.

From a users perspective a confocal cavity has a FSR that is given by $c/4d$ instead of $c/2d$ as would be the case for a plano-plano cavity; the factor of 2 in the denominator can be understood by inspecting the ray trace shown below in Figure II. Note that a ray entering the cavity at a height 'h' parallel to the optical axis of the cavity makes a triangular figure eight pattern as it traverses the cavity. From this pattern it is clear that the ray makes four reflections from the cavity mirrors instead of the two that would result in a plano-plano cavity. Hence the total round-trip path through the cavity is given as $4d$ instead of $2d$.

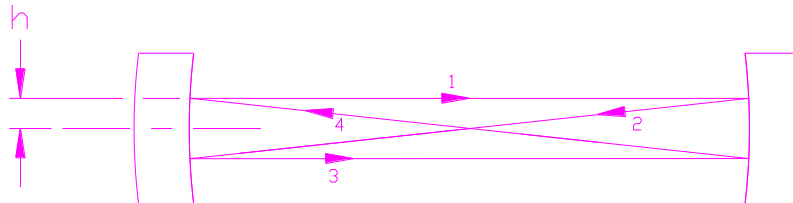


Figure II

Figure II: This figure shows a simplified ray-trace for a ray entering the cavity at height 'h'. The curvature of the mirrors 'R' and the separation being set precisely to 'R' ensures that the input ray is imaged back onto itself after traveling a distance of approximately 4R.

Additionally, in this configuration if a paraxial ray is traced through the system as shown in figure II, it is apparent that in the confocal configuration each mirror serves to image the other mirror back onto itself so that a ray entering the cavity will, after four traverses of the cavity, fall back onto itself, (note that the focal length of a spherical mirror is $R/2$). This imaging of the beam back onto itself greatly simplifies the alignment of the cavity; just align your input to within

a few tenths of a millimeter of the center of the mirror set and restrict your input angles to less than a few degrees. The SA200 series interferometer has two iris diaphragms that simplify this alignment requirement.

Finesse

The finesse of the Scanning Fabry-Perot interferometer is a quantity which characterizes the ability of the interferometer to resolve closely spaced spectral features, it defines the resolution of the instrument. For an infinitely narrow input spectrum, the finesse determines the width of the measured spectrum.

High finesse means high resolution capability, high finesse is obtained by increasing the reflectivity of the cavity mirrors. However, high reflective mirrors reduce the transmission of the interferometer.

In a typical application the SA210 Interferometer is used in conjunction with a signal generator and an oscilloscope, as shown below in figure III. A signal generator (Thorlabs SA201 Fabry-Perot Controller is used for generating the required scan signals for obtaining the data in this document) that can produce either a triangle or saw-tooth wave with an adjustable frequency (5 to 50 Hz), an adjustable amplitude (15 to 40 volts), and an adjustable offset. The signal generator is used to repetitively scan the length of the cavity by $\lambda/4$ in order to sweep through one FSR of the interferometer. An oscilloscope is typically used to view the spectrum and make quantified measurements of spectral features.

Recommended Set-up

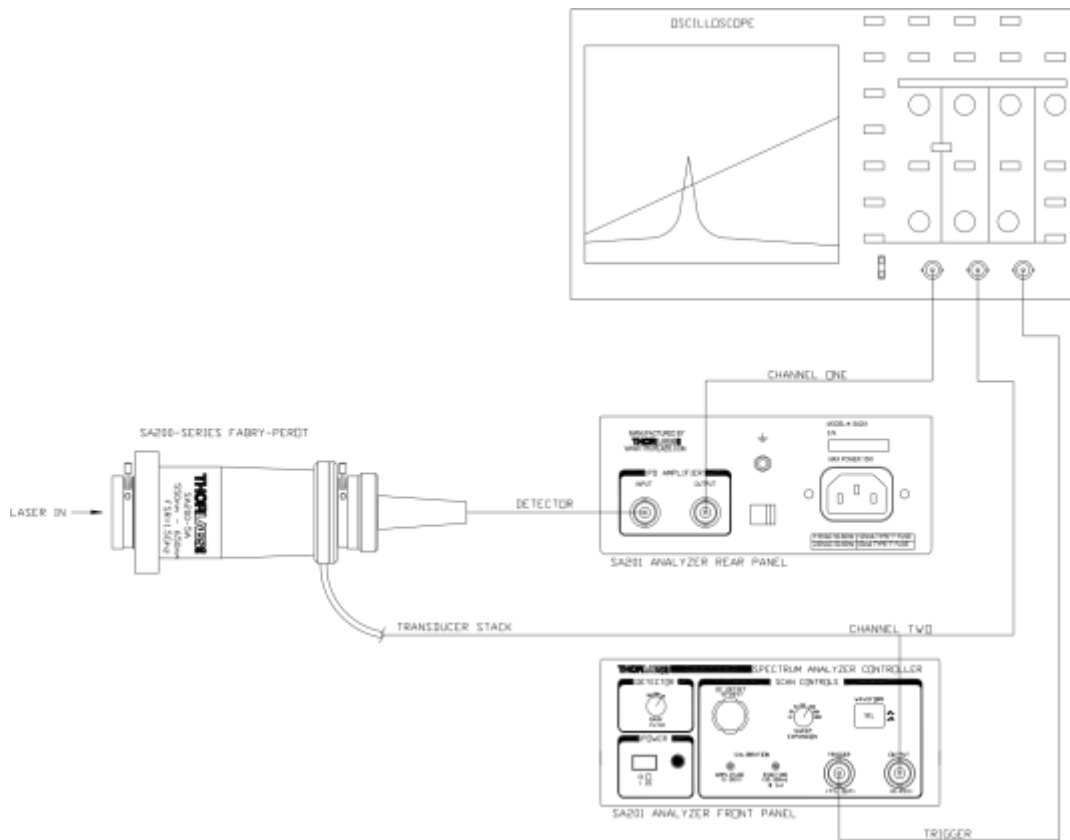


Figure III

Figure III: This figure shows a schematic diagram of a typical setup that is used to measure the spectrum of a laser source. Please note that for this device to be useful the linewidth of the source must be less than the FSR of the interferometer.

SPECTRUM ANALYZER CONTROLLER AND OTHER ACCESSORIES:

- The **SA201** controller generates a voltage ramp, which is used to scan the separation between the two cavity mirrors. A photodiode is used to monitor transmission of the cavity. Using the output sync signal from the controller, an oscilloscope can be used to display the spectrum of the input laser. The controller provides adjustment of the ramp voltage (0 to 20V) and scan-time (1ms to 5s) to allow the user to choose the scan range and speed. An offset control is provided to allow the spectrum displayed on the oscilloscope to be shifted right or left, zoom capability provides up to 100X increase in spectral resolution. • Thorlabs' **KM100**, 1" kinematic mount can be used to mount the SA210 Scanning Fabry Perot Interferometer.

TECHNICAL SUPPORT:

For further questions, or if you suspect a problem with your SA210, please contact Tech Support. An Applications Engineer will gladly assist you.

SA201

Spectrum Analyzer Controller Operating Manual



Related Products



Model	Description
SA200-5A	525 – 650nm Scanning Fabry Perot
SA200-6A	650 – 800nm Scanning Fabry Perot
SA200-7A	780 – 930 nm Scanning Fabry Perot
SA200-9A	900 – 1100nm Scanning Fabry Perot
SA200-12A	1250 – 1400nm Scanning Fabry Perot
SA200-14A	1450 – 1625nm Scanning Fabry Perot

Table of Contents

- WEEE STATEMENT3

- SECTION 1.0: SPECIFICATIONS4
 - PHYSICAL FEATURES:4
 - POWER SUPPLY:4
 - OUTPUT CHARACTERISTICS:4
 - TRIGGER CHARACTERISTICS:5
 - PHOTO DIODE AMPLIFIER CHARACTERISTICS:5
 - SA200-5A, 6A, AND 7A DETECTOR CHARACTERISTICS:5
 - SA200-9A, 12A, AND 14A DETECTOR CHARACTERISTICS:5

- SECTION 2: OVERVIEW6

- SECTION 3: PARTS LIST6

- SECTION 4: DESCRIPTION7
 - DETECTOR GAIN ADJUSTMENT (1)7
 - DC OFFSET CONTROL (2)7
 - SWEEP EXPANSION CONTROL (3)7
 - WAVEFORM CONTROL (4)7
 - POWER SWITCH (5)7
 - POWER ON INDICATOR (6)7
 - AMPLITUDE CONTROL (7)8
 - RISETIME CONTROL (8)8
 - TRIGGER OUTPUT BNC (9)8
 - OUTPUT BNC (10)8
 - GROUND PLUG (11)9
 - AC INPUT CONNECTOR (12)9
 - PD AMPLIFIER INPUT BNC (13)9
 - PD AMPLIFIER OUTPUT BNC (14)9
 - VOLTAGE SELECTOR SWITCH (15)9
 - PD BLANKING CIRCUIT10

- SECTION 5: MAINTENANCE AND TROUBLESHOOTING10
 - MATERIALS NEEDED10
 - FUSE REPLACEMENT10
 - SELECTING THE LINE VOLTAGE11
 - CLEANING11
 - TECHNICAL SUPPORT11

- APPENDIX A: RECOMMENDED SETUP11

Waste Electrical and Electronic Equipment Directive

As required by the WEEE (Waste Electrical and Electronic Equipment Directive) of the European Community and the corresponding national laws, Thorlabs offers all end users in the EC the possibility to return “end of life” units without incurring disposal charges.

This offer is valid for Thorlabs electrical and electronic equipment

- sold after August 13th 2005
- marked correspondingly with the crossed out “wheelie bin” logo (see fig. 1)
- sold to a company or institute within the EC
- currently owned by a company or institute within the EC
- still complete, not disassembled and not contaminated

As the WEEE directive applies to self contained operational electrical and electronic products, this “end of life” take back service does not refer to other Thorlabs products, such as

- pure OEM products, that means assemblies to be built into a unit by the user (e.g. OEM laser drivercards)
- components
- mechanics and optics
- left over parts of units disassembled by the user (PCB's, housings etc.).

If you wish to return a Thorlabs unit for waste recovery, please contact Thorlabs or your nearest dealer for further information.

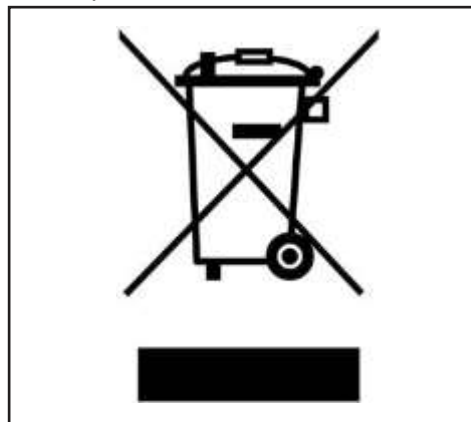
Waste treatment on your own responsibility

If you do not return an “end of life” unit to Thorlabs, you must hand it to a company specialized in waste recovery. Do not dispose of the unit in a litter bin or at a public waste disposal site.

Ecological background

It is well known that WEEE pollutes the environment by releasing toxic products during decomposition. The aim of the European RoHS directive is to reduce the content of toxic substances in electronic products in the future.

The intent of the WEEE directive is to enforce the recycling of WEEE. A controlled recycling of end of live products will thereby avoid negative impacts on the environment.



Crossed out “wheelie bin” symbol

Section 1.0 Specifications

Physical Features:

Dimensions (W x H x D): 5.8" x 2.8" x 12.5" (147mm x 71mm x 317.5mm)
Input and Output Connectors: BNC's
Offset Control: 10-turn Potentiometer
Amplitude Control: 10-turn Trim pot
Risetime Control: 10-turn Trim pot
Sweep Expansion Control: 7-Position Rotary Switch
Photodiode Gain Control: 3-Position Rotary Switch
Waveform Select: Pushbutton w/ illuminated indicators
PD Amp. Features: Blanking with Sawtooth Waveform Falling Edge
Operating Temperature: 10°C to 40°C
Storage Temperature: 0°C to 85°C

Power Supply:

Supply Type: Linear
Voltage Selection: Switch Selectable between 115 / 230V_{AC}
Input Voltage: 100 / 115 / 230V_{AC}
Line Frequency: 50 – 60Hz
Input Power: 15W max
Fuse Ratings: 125mA @ 100 / 115V_{AC}
63mA @ 230V_{AC}
Fuse Type: Slow Blow Type 'T'

Output Characteristics:

Waveform: Sawtooth / Triangle
Default Waveform: Sawtooth
Sawtooth Fall Time: 1ms typ.
Output Voltage Range: 1 to 45V (offset + amplitude)
Max Supply Current ¹: 15mA
Short Circuit Current ²: 26mA max.
Short Circuit Duration²: Continuous
Offset Adj. Range: 0 to 15V_{DC}
Amplitude Adj. Range: 1 to 30V
Risetime Adj. Range ³: 0.01 to 0.1s @ 1X Sweep Exp.
1 to 10s @ 100X Sweep Exp.
Sweep Expansion Settings: 1X, 2X, 5X, 10X, 20X, 50X, 100X
Sweep Scale Error ⁴: +/- 0.5%
Output Noise ⁵: 1mV_{RMS} (~6.6mV_{PP})

Section 1.0 Specifications *continued*

Trigger Characteristics:

Trigger Output Voltage:	TTL levels
VOH (RL = 50W):	2V min.
VOL (RL = 50W):	0.5V max.
Trigger Load Impedance:	50W / Hi-Z
Trigger Rising Edge ⁶ :	Ramp Start
Trigger Falling Edge ⁶ :	Ramp Midpoint

Photo Diode Amplifier Characteristics:

Gain Steps:	0, 10, 20dB
Transimpedance Gain (Hi-Z):	10K, 100K, 1M V/A
Transimpedance Gain (50Ω) ⁷ :	5K, 50K, 500K V/A
Gain Error ⁷ :	+/- 0.1% @ 10K (+/- 0.12%) +/- 0.12% @ 100K (+/- 0.15%) +/- 0.14% @ 1M (+/- 0.3%)
Output Impedance:	50Ω
Load Impedance:	50Ω / Hi-Z
Output Voltage (Hi-Z load):	0-10V min.
Output Voltage (50Ω load):	0-5V min.
Max Output Current ⁸ :	100mA
Bandwidth ⁸ :	250KHz
Noise (RMS) ⁸ :	<0.1mV @ 10K 0.2mV @ 100K 1.5mV @ 1M
Offset ⁸ :	+/- 1mV @ 10K +/- 5mV @ 100K +/- 20mV @ 1M

SA200-5A, 6A, and 7A Detector Characteristics:

Detector:	Silicon
Active Area:	13mm ² (3.6 x 3.6mm)
Spectral Range:	400 to 1100nm
Junction Cap (0V Bias):	110pF typ.
NEP (@ 980nm):	1.2 x 10 ⁻¹⁴ W/√Hz

SA200-9A, 12A, and 14A Detector Characteristics:

Detector:	InGaAs
Active Diameter:	φ1mm
Spectral Range:	700 to 1700nm
Junction Cap (0V Bias):	120pF (80pF typ.)
NEP (@ 980nm):	1 x 10 ⁻¹⁴ W/√Hz

Section 1.0
Specifications *continued*

Notes:

1. Achieved during the sawtooth waveform fall time. This is calculated by $I \text{ (mA)} = C_{\text{piezo}} \text{ (}\mu\text{F)} \times \Delta V_{\text{max}} / \Delta t_{\text{fall}}$
2. The output drive amplifier will current limit the load to 26mA max. Although the unit may operate continuously under these conditions, it is not recommended since the unit will heat up causing stress to the electronics.
3. The risetime adjustment range for each sweep setting is as follows:
Risetime Adj. Range = (0.01 x sweep expansion setting) to (0.1 x sweep expansion setting).
4. Defined as the scaling error between 1X and any other gain settings (ex. 2X +/- 0.5%).
5. Measures with SA200 series scanning head connected to output.
6. 'Ramp' refers to the rising, or scanning, edge of the 'Output' waveform.
7. The gain error does not apply when using a 50Ω load since the user-installed output terminator will probably have a resistance tolerance greater than the gain errors above. Also note that the 50W output series resistance is 49.9W +/-1%. This will also factor into gain error when using a 50Ω load.
8. Test performed with a 50Ω terminator and a 6' (~1.8m) 50Ω coax cable.

Section 2.0 Overview

The SA201 is specifically designed to control Thorlabs SA200 Series Fabry Perot Interferometers. The controller generates a voltage ramp, which is used to scan the separation between the two cavity mirrors. The controller provides adjustment of the ramp voltage and scan time, allowing the user to choose the scan range and speed. An offset control is provided to allow the spectrum displayed on the oscilloscope to be shifted right or left. Another convenient feature of the controller is a zoom capability that provides a 1X, 2X, 5X, 10X, 20X, 50X and 100X increase in the spectral display resolution. The output TTL level trigger allows the user to externally trigger an oscilloscope on either the beginning or midpoint of the ramp waveform.

The SA201 also includes a high precision photodetector amplifier circuit used to monitor the transmission of the cavity. The amplifier provides an adjustable transimpedance gain of 10K, 100K, and 1M V/A when driving a high impedance load, such as an oscilloscope. Using the output sync signal from the controller, an oscilloscope can be used to display the spectrum of the input laser. The detector circuitry incorporates a blanking circuit, which disables the photodiode response during the falling edge of the sawtooth waveform.

Section 3.0 Parts List

Below is a list of all components shipped with the SA201 Spectrum Analyzer Controller.

- ⑩ SA201 Spectrum Analyzer Controller
- ⑩ Operating Manual
- ⑩ US Power Supply Line Cord
- ⑩ 63mA Fuse for use at 230VAC operation (125mA fuse installed in unit)

The following items are sold separately:

- ⑩ SA200-5A: 525-650nm Scanning Fabry Perot with Silicon Photodetector
- ⑩ SA200-6A: 650-800nm Scanning Fabry Perot with Silicon Photodetector
- ⑩ SA200-7A: 780-930nm Scanning Fabry Perot with Silicon Photodetector
- ⑩ SA200-9A: 900-1100nm Scanning Fabry Perot with InGaAs Photodetector
- ⑩ SA200-12A: 1250-1400nm Scanning Fabry Perot with InGaAs Photodetector
- ⑩ SA200-14A: 1450-1625nm Scanning Fabry Perot with InGaAs Photodetector

Section 4.0 Descriptions

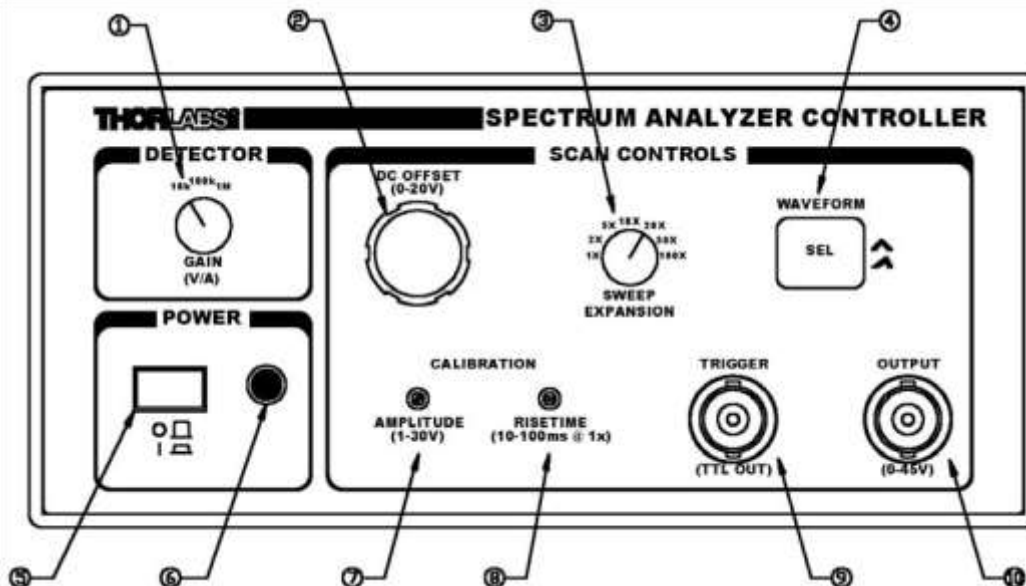


Figure 1- SA201 Front Panel

Detector Gain Adjustment (1)

The SA201 includes a built in photodiode amplifier circuit. This amplifier is designed specifically to operate with the detector provided with the SA200 series Fabry Perot Interferometer, allowing the user to monitor the transmission of the cavity. While any photodetector may be connected to the amplifier the specifications, listed in Section 1, apply only to detectors supplied with the SA200 series. The amplifier provides a transimpedance gain (current to voltage gain) of 10K, 100K, and 1M V/A while driving a Hi-Z load, such as an oscilloscope. For better noise and performance characteristics it is recommended that a 50Ω coax cable with a 50Ω terminating resistor be used. The Photodetector input and output BNC's are located on the rear panel.

DC Offset Control (2)

The DC Offset provides a continuously adjustable offset voltage over the range of 0 to 15V using a 10-turn potentiometer. This offset adds directly to the ramp signal. The DC offset control is used to adjust the waveform from left to right across an oscilloscope viewing window, without affecting the calibration of the cavity.

Sweep Expansion Control (3)

The sweep expansion provides a zoom capability to increase the spectral display resolution by a factor of 1x, 2x, 5x, 10x, 20x, 50x, and 100x. This is achieved by scaling the ramp rise time by the sweep expansion.

Waveform Control (4)

The SA201 allows the user to select between a sawtooth and triangular waveform. The sawtooth waveform is desirable for most applications, however the triangle waveform is useful for cavity alignment. The SA201 will default to the sawtooth waveform during the system power-up. To change the waveform, simply press the 'WAVEFORM SEL' button. The selected waveform is indicated by the illuminated symbol to the right of the waveform select button.

Power Switch (5)

The power switch is used to toggle the unit on and off.

Power On Indicator (6)

The power on LED will light when the unit is powered up.

Section 4.0 Descriptions *continued*

Amplitude Control (7)

The amplitude control allows the user to adjust the ramp amplitude from 1 to 30V peak to peak using a 10-turn trimpot. Note, the ramp signal is added to the DC offset. This means that when the offset is set to 0V, the ramp will start at 0V and increase to the amplitude limit setting. The amplitude is used to determine how far the mirror will be scanned, or to set the spectral range of the optical head.

Risetime Control (8)

The risetime control allows the user to continuously adjust the scan rate from 0.01ms to 0.1ms using a 10-turn trimpot. Note, the risetime setting may be scaled by the sweep expansion setting. For example: If the scan rate is set to 0.05s and the sweep expansion is adjusted from 1x to 100x then the scan rate will adjust to 5s. The scaling error is typically less than +/-0.5%, providing excellent measurement capabilities.

Trigger Output BNC (9)

This trigger output signal may be used to externally trigger the oscilloscope. The trigger is capable of driving 50Ω terminated cables, as well as Hi Z loads such as oscilloscopes. The trigger will provide an edge on the beginning and middle of the scanning ramp. See Figure 2 below.

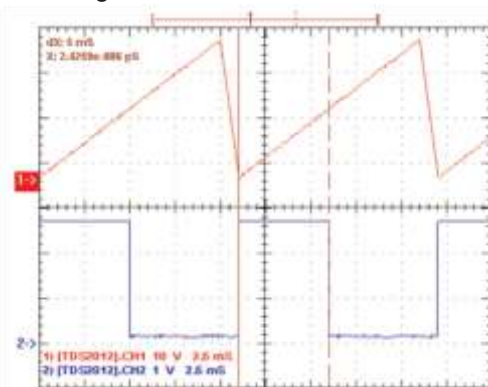


Figure 2, Trigger Logic

Output BNC (10)

The output BNC is used to drive the SA200 scanning piezos from 1V to 45V. The output is capable of driving 0.6μF piezo loads at a ramp rate of 1ms over the full voltage range. The output current is internally limited to prevent damage to the output drive. Note: the output performance specifications assume a Thorlabs Fabry Perot Interferometer module is connected.

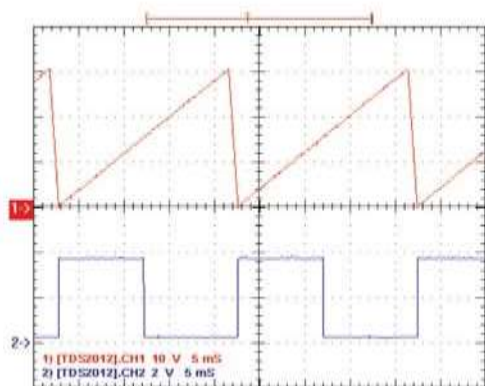


Figure 3, Sawtooth Waveform

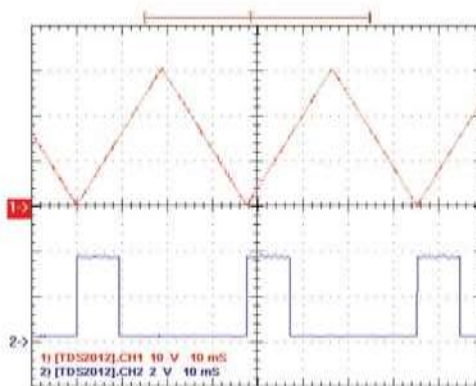


Figure 4, Triangle Waveform

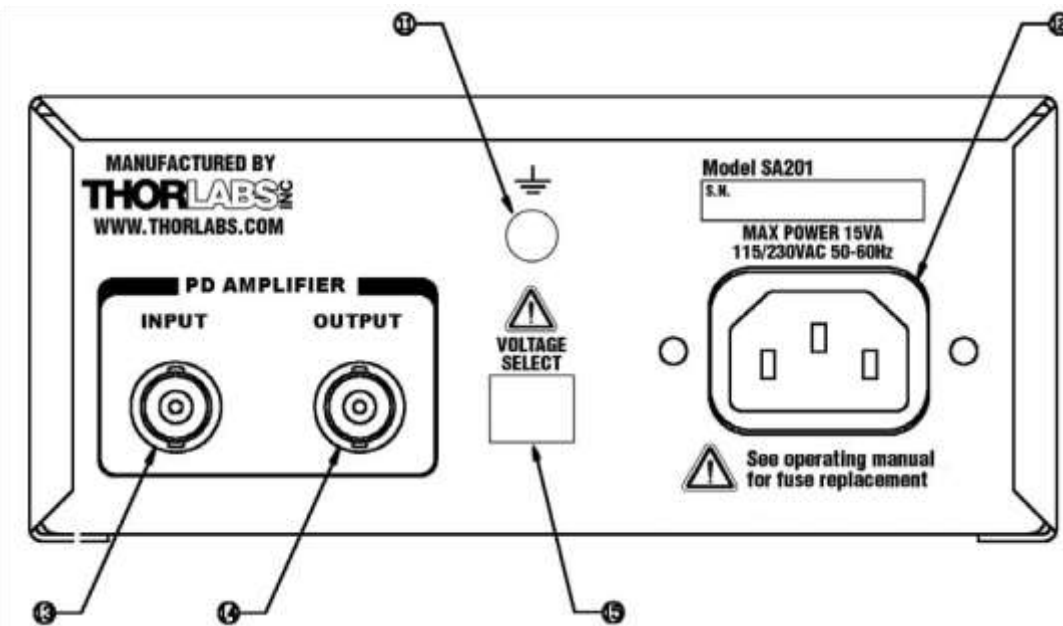


Figure 5- SA201 Rear Panel

Ground Plug (11)

This ground plug is for use as a general-purpose ground connection. It is connected directly to the earth ground connection of the input power plug.

AC Input Connector (12)

This is the line voltage input connection. IMPORTANT: The unit is configured for 100 / 115VAC, 50-60Hz from the factory. To operate at 230VAC see Section 5.

PD Amplifier Input BNC (13)

This input BNC is used to interface the photodetector, provided with the SA200 scanning heads, to the amplifier circuit. The photodiode amplifier is configured to operate with the Thorlabs supplied photo detectors; however it is possible to operate user supplied photo detectors. To do so, the BNC center contact must be connected to the photo detector cathode and the BNC shell must be connected to the photodiode anode (unbiased operation). If a biased detector is to be used the BNC shell must be connected to the bias ground and the bias voltage must be negative for the circuit to operate properly.

PD Amplifier Output BNC (14)

This BNC is the amplifier output and may be connected directly to an oscilloscope to view the cavity spectrum. The amplifier gain will be set using the front panel 'DETECTOR' control knob. The amplifier output includes a 50Ω series resistor to minimize noise when operating with a 50Ω coax cable. For best results, a 50Ω load resistor is recommended at the oscilloscope. Note, the amplifier gain will be halved with a 50Ω load connected.

Voltage Selector Switch (15)

The voltage selector switch allows the user to select the input line voltage they will be operating the system at. The factory default setting is 100 / 115V_{AC} as shown in figure 2. To operate at 230V_{AC}, this switch will have to be moved to the 230V position. The line fuse will also need to be changed to properly protect the unit. See section 5 for detailed instructions.

Section 4.0 Descriptions

continued

PD Blanking Circuit

The detector amplifier includes a blanking circuit, which blocks any photo detector response during the falling edge of the sawtooth waveform. This is very useful when triggering on the photo diode spectral response, because unwanted signals while the cavity resets will be removed. The blanking is not available when using the triangle waveform, since it is useful to see the rising and falling response overlapped during system alignment. This feature may be disabled as described below:

1. Important – Disconnect the scanning head or any piezo device from the SA201 output.
2. Important – Disconnect the power cord. Do not open the unit if the power cord is connected.
3. Remove the two screws securing the enclosure cover with a Phillips head screwdriver. The screws are located on the bottom side, rear corners of the unit. Do not lose the screws.
4. Carefully remove the cover by sliding toward the rear of the unit.
5. Locate the JP3 header. It is positioned in front of the heat sink and will have a shorting jumper on pin 1.
6. Remove the shorting jumper and place across (Shorting) the JP3 pins to disable the blanking circuit. The default setting will be blanking enabled. The jumper will not be shorting the pins.
7. Replace the enclosure cover and secure with the enclosure screws.

Section 5.0 Maintenance & Troubleshooting



DANGER! – The Thorlabs Spectrum Analyzer Controller, SA201, must be powered off, unplugged from the AC input source, and disconnected from any piezo elements prior to replacing the fuse or removal of the cover. Failure to do so may cause **SERIOUS INJURY** to the user, since high voltages exist within the unit.

WARNUNG! - Sicherheitsanweisungen für den Thorlabs Spectrum Analyzer Controller (SA201).

Bevor die Sicherung gewechselt oder die Gehäuseabdeckung entfernt werden darf, muß das Gerät abgeschaltet und das Spannungsversorgungskabel von der Netzspannung getrennt werden. Das nicht befolgen dieser Anweisungen, kann zu lebensgefährlichen Verletzungen führen, da das Gerät intern unter Hochspannung steht.

Materials Needed

- SA201 Operating Manual – The most recent version of this operating manual will be available on Thorlabs website.
- 63mA Type 'T' Slow Blow Fuse – The 63mA fuse is required for 230V operation only. Thorlabs supplies a 63mA fuse with all of its SA201 units and must be installed when operating at 230VAC.
- 125mA Type 'T' Slow Blow Fuse – The 125mA fuse is installed from the factory. This must be installed when operating the unit at 100 / 115VAC.
- Phillips Head Screwdriver (#2 Preferred) – We do not recommend using electrically powered screwdrivers.

Fuse Replacement

1. Important – Disconnect the scanning head or any piezo device from the SA201 output.
2. Important – Disconnect the power cord. Do not open the unit if the power cord is connected.
3. Remove the two screws securing the enclosure cover with a Phillips head screwdriver. The screws are located on the bottom side, rear corners of the unit. Do not lose the screws.
4. Carefully remove the cover by sliding toward the rear of the unit.
5. Locate the fuse box between the input line voltage connector and the transformer.
6. Remove the fuse cover and slide the old fuse out.
7. Install the new fuse into the fuse cover and place back into the fuse box. (125mA @ 100/115V_{AC} and 63mA @ 230V_{AC})
8. Replace the enclosure cover and secure with the enclosure screws.



Selecting the Line Voltage



1. Important – Replace the line fuse as described above.
2. Locate the voltage selector switch on the rear panel. See Figure 5 leader 15.
3. Switch to the appropriate line voltage.
4. Install the appropriate line cord and turn the unit on.

Cleaning

The SA201 should only be cleaned with a soft cloth and a mild soap detergent or isopropyl alcohol. Do not use a solvent-based cleaner.

Technical Support

You may use any of the following methods to contact Thorlabs in case of difficulty or if you have questions regarding the SA201.

www.thorlabs.com

Thorlabs web site will have up to date application notes and frequently asked questions regarding our products.

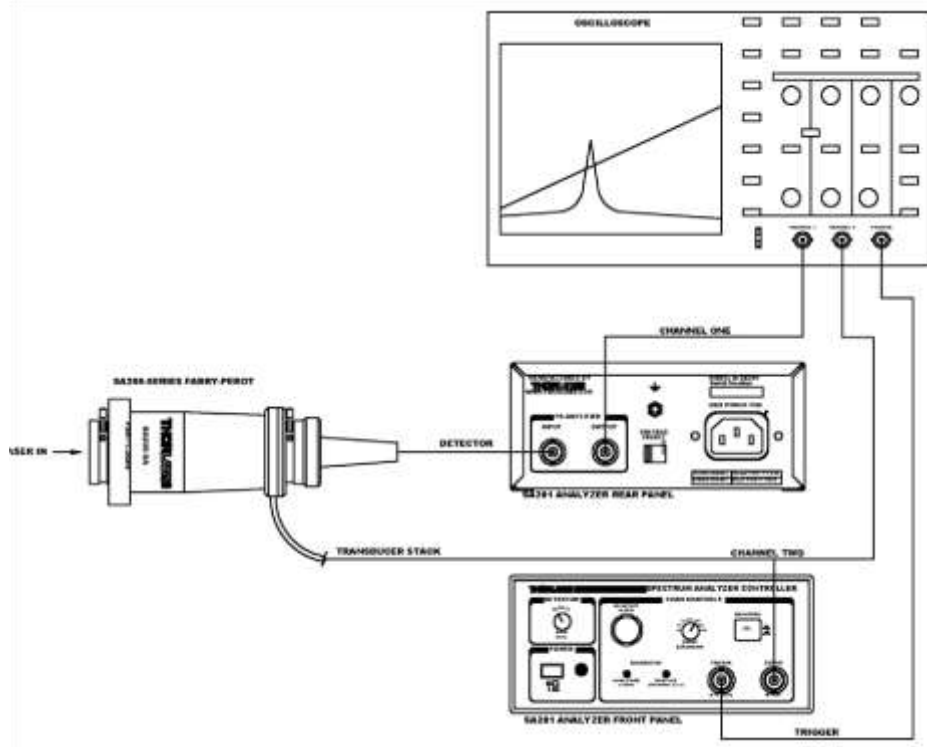
Techsupport@thorlabs.com

Send a detailed email message and one of our application engineers will respond promptly (within 1 business day).

Mail:

Thorlabs, Inc.
435 Route 206N
Newton, NJ 07860
Phone: (973) 579-7227
Fax: (973) 300-3600

Appendix A: Recommended Setup



S120C Compact Photodiode Power Head with Silicon Detector

The S120C power head is designed for general purpose optical power measurements. The head is optimized for small thickness to fit in tight spaces. The high sensitive photodiode with large active area in combination with an absorptive ND filter enables power measurements up to 50 mW in freespace and fiber-based applications. A removable annular IR viewing target allows conveniently centering the measured beam to the active area of the photo-diode. The target absorbs light from 400 to 640nm and 800 to 1700nm.

The S120C housing includes a threaded input in axis with the light input aperture that is compatible with any number of Thorlabs 1" threaded accessories. This allows convenient mounting of external optics, fiber adapters, light filters, and apertures. A 8-32 threaded mounting hole is provided to accommodate posts and post holders (a M4 adapter for metric posts is included).

The S120C is compatible with the new Thorlabs PM100D and PM100A consoles. A non-volatile memory in the sensor connector contains sensor information data and the NIST and PTB traceable calibration data.

Technical Specifications

Detector Type	Silicon Photodiode
Wavelength Range	400 - 1100 nm
Optical Power Working Range	50 nW – 50 mW
Max Average Power Density	20 W/cm ²
Max Pulse Energy	20 µJ
Linearity	± 0.5%
Resolution ¹⁾	1nW
Measurement Uncertainty ²⁾	±3% 451 – 1000 nm ±5% 400 – 450 nm, 1001 – 1100 nm
Typical Application	Low Power Lasers
Laser Types	Diode, Diode Arrays, He-Ne, Dye, Ion Lasers (Ar ⁺ , Kr ⁺)
Coating /Diffuser	Absorptive ND (Schott NG3)
Cooling	Convection
Head Temperature Measurement	Themistor 4.7kΩ
Console Compatibility	PM100D, PM100A
Response Time	< 1 µs
Sensor Dimensions	Ø30.5 mm x 12.7 mm
Active Detector Area	9.7 mm x 9.7 mm
Input Aperture	Ø9.5 mm
Cable Length	1.5 m
Connector	Sub-D 9p male

¹⁾ Measured with PM100D console in bandwidth low setting.

²⁾ Including uniformity failure

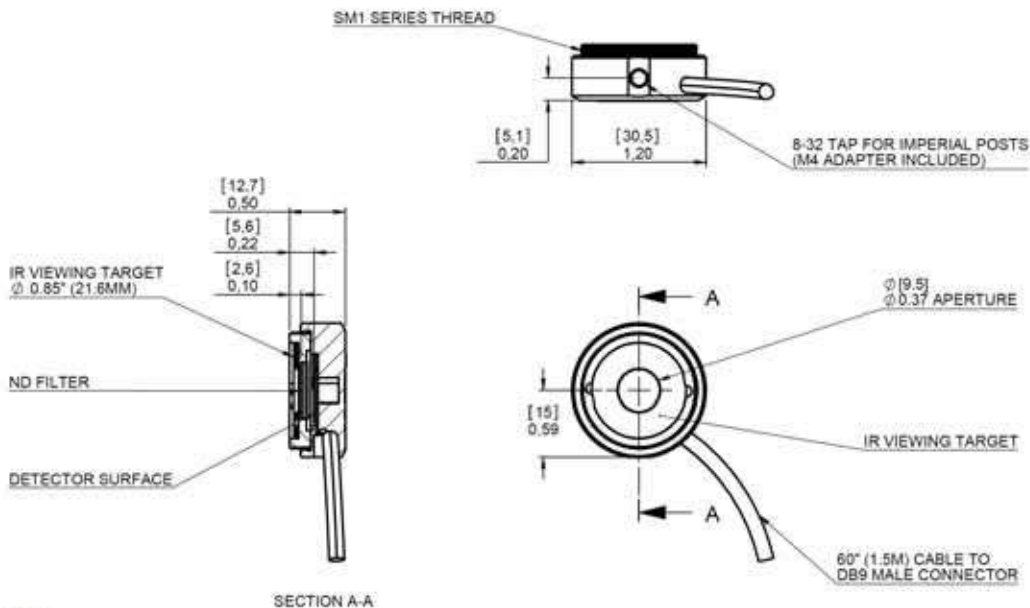
Please note that the S120C power meter head is not compatible with older Thorlabs power meter consoles (PM100, PM30, PM300, PM300E, S100).

US: PO Box 366, 435 Route 206N, Newton, NJ 07860, Tel: +1 (973) 579-7227, Fax: +1 (973) 3600,
 Europe: Hans-Boeckler-Str. 6, 85221 Dachau/Munich, Germany, Tel: +49 8131 59560, Fax +49 8131 595699
 Web: <http://www.thorlabs.com> Mail: europe@thorlabs.com

Weight	0.07 kg
Post	#8-32 thread, M4 Adapter included
Aperture Thread	SM1, outer thread
Fiber Adapters (optional)	FC, SC, LC, SMA, ST

Mechanical Drawing

INFORMATION ONLY; NOT FOR MANUFACTURING
ALL DIMENSIONS IN PARANTHESES ARE MILLIMETERS



Sensor Connector

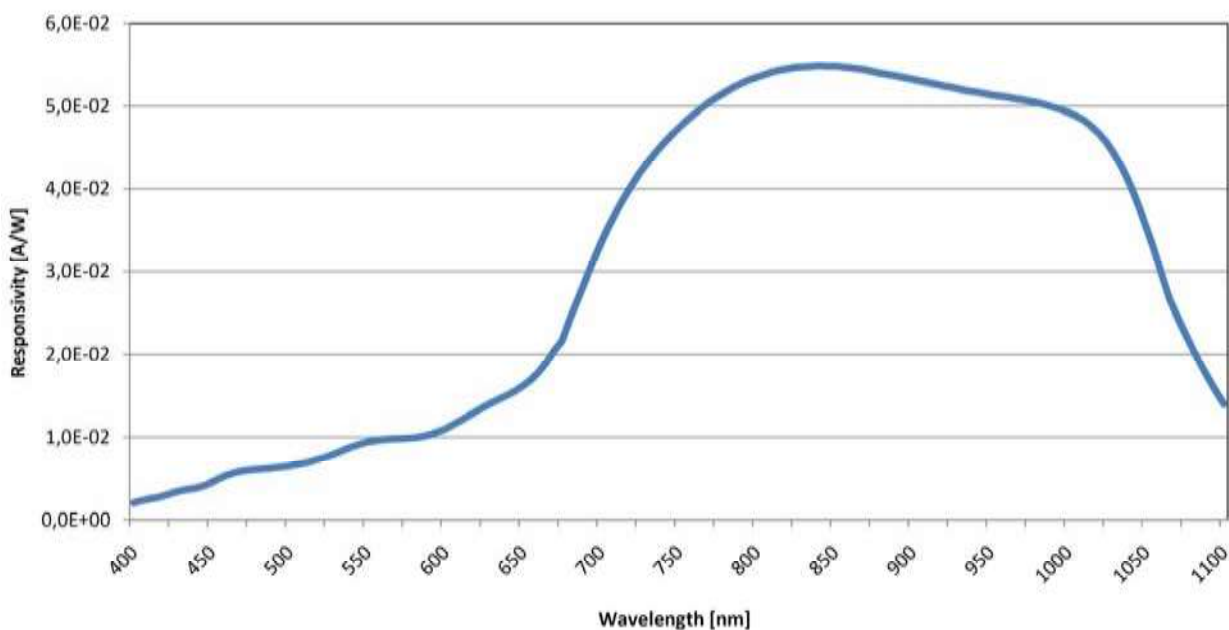
US: PO Box 366, 435 Route 206N, Newton, NJ 07860, Tel: +1 (973) 579-7227, Fax: +1 (973) 3600,
Europe: Hans-Boeckler-Str. 6, 85221 Dachau/Munich, Germany, Tel: +49 8131 59560, Fax +49 8131 595699

Web: <http://www.thorlabs.com> Mail: europe@thorlabs.com



Pin 3: Photodiode Anode
Pin 4: Photodiode Cathode

Typical Spectral Response Graph



Available Accessories

- S120-FC** FC fiber adapter
- S120-SMA** SMA fiber adapter
- S120-SC** SC fiber adapter

US: PO Box 366, 435 Route 206N, Newton, NJ 07860, Tel: +1 (973) 579-7227, Fax: +1 (973) 3600,
Europe: Hans-Boeckler-Str. 6, 85221 Dachau/Munich, Germany, Tel: +49 8131 59560, Fax +49 8131 595699

Web: <http://www.thorlabs.com> Mail: europa@thorlabs.com

S120-LC	LC fiber adppter	
S120-ST	ST fiber adapter	
AS4M8E	M4 to 8-32 Adapter	(included)
SM1CP1	Dust cap	(included)

The *S120C* is also compatible to the Thorlabs imperial and metric post and post-holder series and Thorlabs SM1 mechanics.

Cleaning and Maintenance

There are no serviceable parts in the *S120C* head. The housing may be cleaned by wiping with a soft damp cloth. When cleaning the aperture filter, treat it as any other fine optic. Gently blow off any debris using compressed air and wipe gently with an optic tissue wetted with propanol. If you suspect a problem with your *S120C* please call Thorlabs and an engineer will be happy to assist you.

As long as the sensor has not been exposed to excessive optical power (please pay attention to the maximum ratings in the technical specifications), the calibration should be very stable over long periods of time (well over a year). To keep the accuracy and performance of the *S120C*, Thorlabs recommends a yearly recalibration, starting one year after purchase.

WEEE

As required by the WEEE (Waste Electrical and Electronic Equipment Directive) of the European Community and the corresponding national laws, Thorlabs offers all end users in the EC the possibility to return "end of life" units without incurring disposal charges.

This offer is valid for Thorlabs electrical and electronic equipment

- sold after August 13th 2005
- marked correspondingly with the crossed out "wheelie bin" logo (see fig. 1)
- sold to a company or institute within the EC
- currently owned by a company or institute within the EC
- still complete, not disassembled and not contaminated

As the WEEE directive applies to self contained operational electrical and electronic products, this "end of life" take back service does not refer to other Thorlabs products, such as

- pure OEM products, that means assemblies to be built into a unit by the user (e. g. OEM laser driver cards)
- components
- mechanics and optics
- left over parts of units disassembled by the user (PCB's, housings etc.).

If you wish to return a Thorlabs unit for waste recovery, please contact Thorlabs or your nearest dealer for further information.

US: PO Box 366, 435 Route 206N, Newton, NJ 07860, Tel: +1 (973) 579-7227, Fax: +1 (973) 3600,
Europe: Hans-Boeckler-Str. 6, 85221 Dachau/Munich, Germany, Tel: +49 8131 59560, Fax +49 8131 595699

4

Web: <http://www.thorlabs.com> Mail: europa@thorlabs.com

Waste treatment on your own responsibility

If you do not return an “end of life” unit to Thorlabs, you must hand it to a company specialized in waste recovery. Do not dispose of the unit in a litter bin or at a public waste disposal site.

Ecological background

It is well known that WEEE pollutes the environment by releasing toxic products during decomposition. The aim of the European RoHS directive is to reduce the content of toxic substances in electronic products in the future.

The intent of the WEEE directive is to enforce the recycling of WEEE. A controlled recycling of end of live products will thereby avoid negative impacts on the environment.



Crossed out “wheelie bin” symbol

Quick Reference

Thorlabs Instrumentation

Optical Power and Energy Meter

PM100D



2009

Safety

THORLABS

Attention

All statements regarding safety of operation and technical data in the instruction manual will only apply when the unit is operated correctly.

The power meter PM100D must not be operated in explosion endangered environments!

Sensor, photodiode and control inputs and outputs must only be connected with duly shielded connection cables.

Only with written consent from Thorlabs may changes to single components be carried out or components not supplied by Thorlabs be used.

Do not remove covers!

Refer servicing to qualified personal!

Table of Content

1 General Information	3 2 Getting Started	3
2.1 Unpacking	3 2.2 Preparation	3 2.3 Physical Overview 4
3 Operating the PM100D		6
3.1 Connecting a Power or Energy Sensor	6 3.2 Controlling the PM100D	
6		
3.2.1 Navigating the Menus	6 3.2.2 Power and Energy Measurement in the	
Numeric Display	8 3.2.3 Display Options	10 3.2.4 Analog Output
		11
3.2.5 Battery Charging	11 3.3 Computer Interface	11
4 Addresses		12

1 General Information

The PM100D Handheld Optical Power and Energy Meter is designed to measure the optical power of laser light or other monochromatic or near monochromatic light sources and the energy of pulsed light sources.

The space-saving, battery powered design and compatibility to all Thorlabs "C Series" Photodiode, Thermal, Pyroelectric sensors, and custom Photodiode, Thermal and Pyroelectric detectors, combined with a fast USB device interface open a wide range of applications in Manufacturing, Quality Control, Quality Assurance, and R&D for stationary and field use.

Please refer to the user manual on the data carrier supplied with the unit for detailed function description.

2 Getting Started

2.1 Unpacking

Inspect the shipping container for damage.

If the shipping container seems to be damaged, keep it until you have inspected the contents and you have inspected the PM100D mechanically and electrically.

Verify that you have received the following items within the hard-case:

1. PM100D power/energy meter console
2. 1GB SD memory card – installed in PM100D
3. Plug-In power supply with Interchangeable primary plug for USA, UK, Europe, and Australia
4. USB cable, type 'A' to 'mini-B'
5. Quick-start guide
6. USB memory stick with instrument drivers, user application and operation manual
7. Certificate of Calibration

2.2 Preparation

Configure the plug-in power supply with the primary plug for your local power supply. Connect a suitable power or energy sensor. The sensors have a self-fixing mechanism. To plug or unplug a sensor slightly press from both sides on the pins in the connector housing.

Turn the unit on by pressing the power button in the side panel.

After switching on the unit, the graphics display will show the device status and then jump to the last measurement screen before power down.

The PM100D is immediately ready to use after turning on.

2.3 Physical Overview



Function Keys:

Navigation: 
 Enter/Edit: **OK**

Wavelength: λ
 Relative Measure: Δ
 Backlight: 

Figure 1 Front Panel

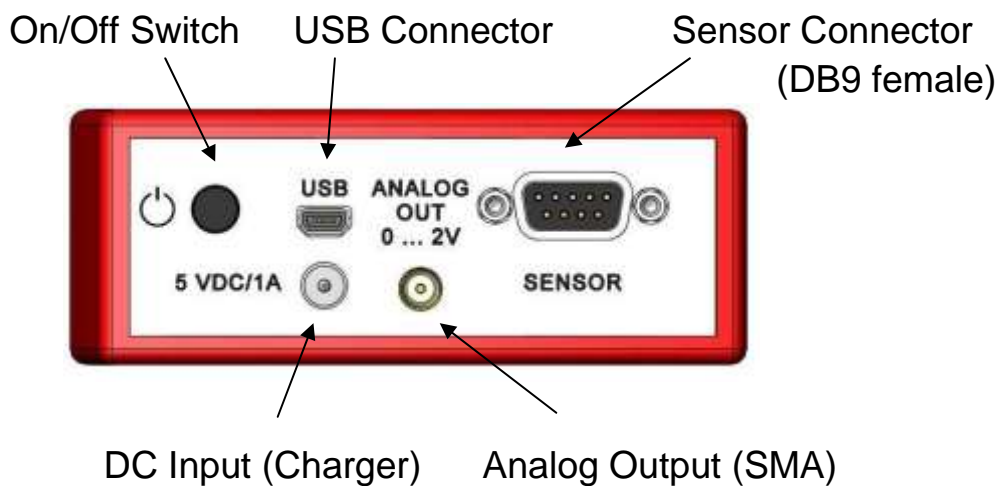


Figure 2 Side Panel

Mounting Thread 1/4"-20 SD Card Slot



Figure 3 Bottom View

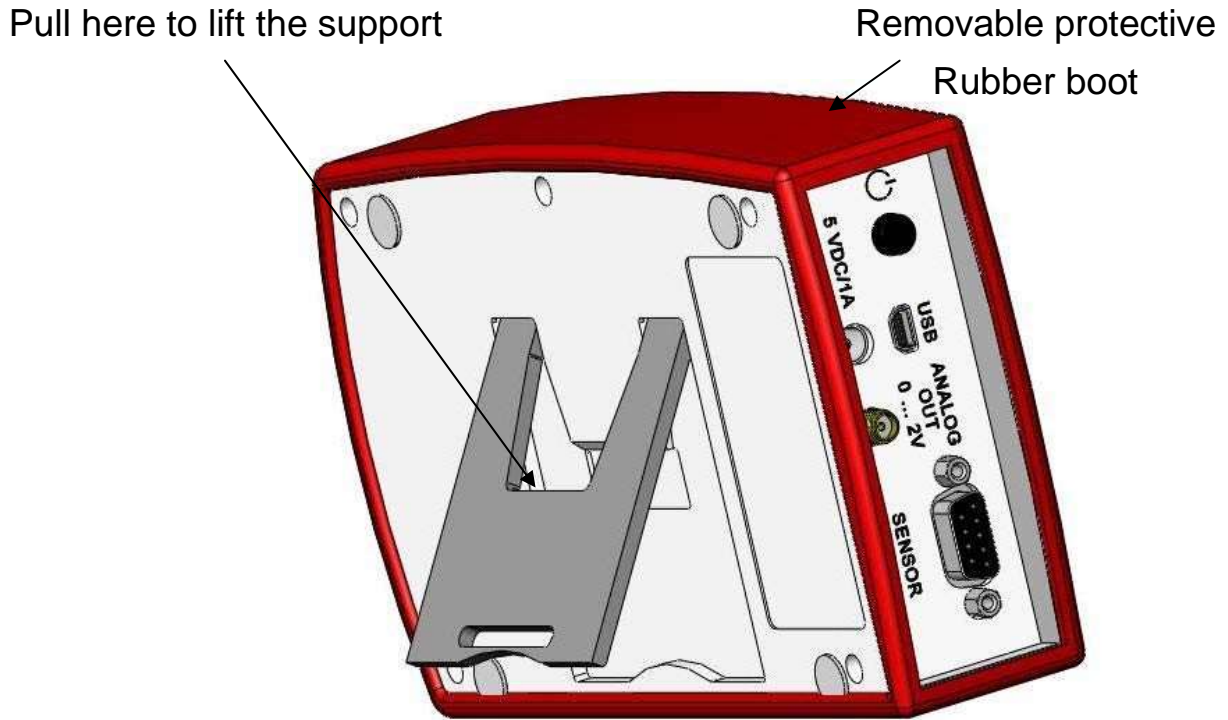


Figure 4 Rear View

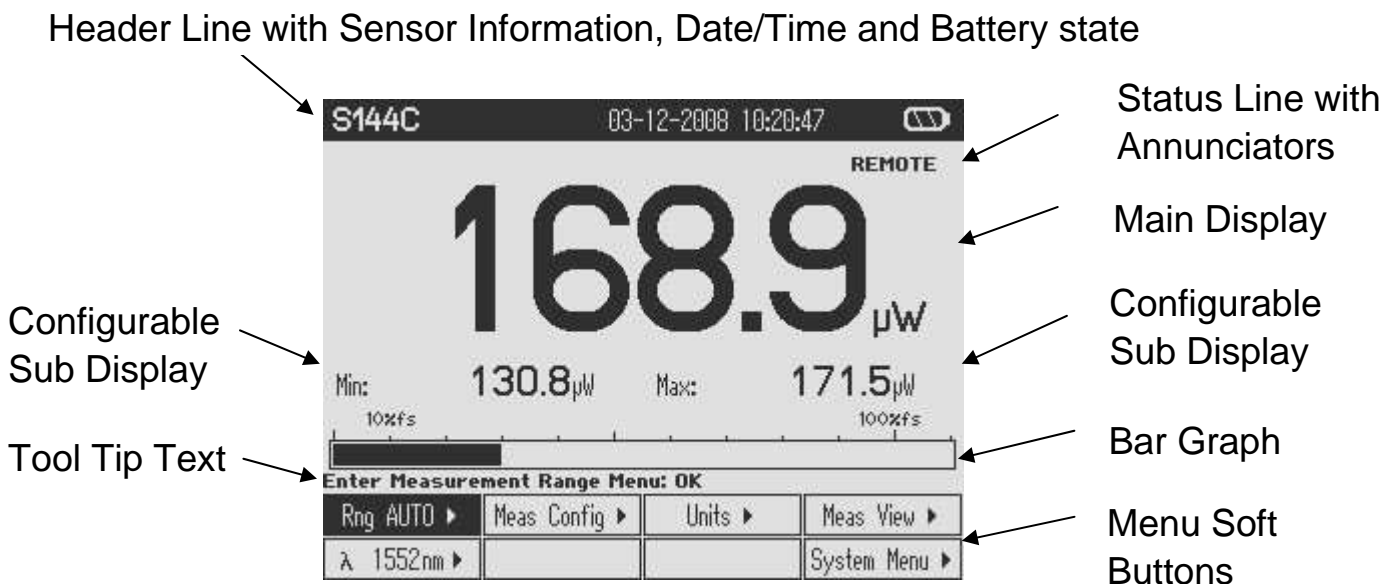


Figure 5 Numeric Display Setup

3 Operating the PM100D

3.1 Connecting a Power or Energy Sensor

The PM100D supports all Thorlabs 'C-Series' photodiode, thermal and pyroelectric sensors. These can easily identified against older versions of Thorlabs power or

energy sensors by their red connector housing. The console will not recognize sensors from the ‘A’ and ‘B’ series. Please contact Thorlabs for upgrading of old sensors with ‘C-Series’ connectors.

To plug or remove a sensor slightly press the two bolts in the connector housing. Sensors can be ‘hot-swapped’ to the console, after recognizing a new valid sensor the type and calibration data will be downloaded to the console in approximately 2 seconds and the unit is ready to operate with the new sensor.

3.2 Controlling the PM100D

3.2.1 Navigating the Menus

Each measurement screen contains of eight soft buttons that are arranged in 2 rows in the bottom of the graphics display. These can be controlled by the four navigation (\leftarrow \rightarrow \uparrow \downarrow), and the enter/edit (**OK**) key. An interactive help text above describes shortly the function of each selected button.

The soft buttons may be configured with the following functions:

Type	Indicator	Function when pressing ‘OK’	Example
Menu		Shows a sub menu, by rearranging the soft button labels	Meas Config 
Ring Control		Scrolls up and down the ring with the up and down navigation buttons. The changes are valid immediately. A blinking button frame indicates that the control is active. Confirm with ‘OK’	Range 
Function key	Label in capitals	Proceeds the described function	RESET
Radio button		Selects the function of the pressed key. The active key gets the ‘checked’ mark ()	 W
Numeric	Key label contains a number	The button goes in the ‘edit’ mode. This is indicated by a blinking frame and one digit with a blinking underline. With the \leftarrow \rightarrow \uparrow \downarrow buttons navigate the digit to change; with the \leftarrow \rightarrow keys increment or decrement the digit. Confirm with ‘OK’	1.55 <u>0</u> µm

Button Appearance: Focus on Button **Text** Edit Mode **Blinking frame**

All sub menus can be left by **Negative** navigating to the **EXIT** button at the downright soft button location or to any empty button, and pressing the **OK** key.

System Settings

System Menu ▶ The following sub menus will appear: -

Measurement Settings

- Remote state PM100D can be switched back to local mode
- Line filter Sets the unit to the local line frequency 50Hz/60Hz to avoid aliasing effects
- Default sensor Sets the PM100D in a mode to measure photo current, thermal voltage or peak voltage from a pyroelectric detector. See user manual.

- Console Settings

- Language User interface language setting
- Backlight Switches the LCD and key backlight on and off (Same function as the key)
- Brightness Sets the brightness of the LCD and key backlight. The setting range is 0 – 100% in 1% increments
- LCD Contrast Adjusts the LCD contrast. The setting range is 0 – 100% in 1% increments
- Sound Switches on and off the key and warning sounds
- Shutdown The unit automatically powers off in battery operation after a certain time without user action. This feature can be set to 10 minutes, 1 hour or switched off; and is not active when an external power supply (AC adapter or USB) is connected.
- Firmware Upload Needs to be ‘enabled’ before uploading a new firmware version. The function will automatically reset to ‘disabled’ when powering down.

- Date and Time

Enters a submenu to set date and time. It is possible to chose various date and time formats.

- Console Info

Shows the console related information.

- Sensor Info

Shows the related information of the currently connected power or energy sensor.

3.2.2 Power and Energy Measurement in the Numeric Display

The numeric display contains a large configurable measurement value, two small sub displays for additional measurement information, and a bar-graph that shows the saturation degree of the chosen measurement range. To control and configure the numeric display the soft buttons in the top level are arranged as following:

Rng 570µW ▶	Meas Config ▶	Units ▶	Meas View ▶
λ 1552nm ▶	MAX RESET	TUNE ◀	System Menu ▶

3.2.2.1 Range Control

Rng 570µW ▶

Set Measurement Range: ▲▼ Exit: OK

Rng 3.30mW ◄	AUTO OFF		
			EXIT

Up to 6 power corresponding current and 4 power / energy corresponding voltage ranges can be chosen manually with the \curvearrowright or \curvearrowleft keys. For power measurements an auto-ranging function is available.

3.2.2.2 Wavelength Correction

λ 1552nm ▶

λ

Select Wavelength: OK Edit Wavelength: Hold OK Exit: λ

λ 405 nm	λ 535 nm	λ 635 nm	λ 780 nm
λ 1064 nm	λ 1310 nm	✓ λ 1550 nm	λ 10600 nm

✓ λ 1552 nm

The menu offers 8 individually configurable sensor independent wavelength settings. To edit a wavelength keep the **OK** key pressed for 1 second. Set the desired wavelength with the \curvearrowright \curvearrowleft \downarrow \uparrow keys.

3.2.2.3 Readout Configuration

Units ▶

Select Units of Main Display: OK

dBm	✓ Watt	Ampere	
Sub Left ▶	Sub Right ▶		EXIT

Depending on the connected sensor the units of measure for the large display can be configured to Watt, dBm, Joule, Volt or Ampere.

For additional information two small displays are arranged below the main display

Sub Left ▶

Hide left Sub Display: OK

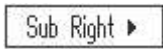
Min Val	✓ Frequency	Temperature	Off
			EXIT

Min Val: Minimum level until MAX RESET is pressed. Same unit as main display.

Frequency: Displays the frequency of a power signal or the repetition rate for pulsed laser sources

Temperature: Shows the sensor head temperature.

Off: Hides the left sub-display



Ratio Max/Min: OK

Max Val	✓ Max/Min	Area	Off
	Alt Unit		EXIT

Max Val: Maximum level until MAX RESET is pressed in main display unit.

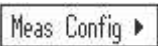
Max/Min: Ratio between maximum and minimum.

Area: Calculates power and energy density from the set beam diameter.

Alt Unit: Shows the measurement in its alternate unit (e.g. W – dBm)

Off: Hides the right sub-display

3.2.2.4 Measurement Configuration Menu



Photodiode Sensor

Exit Menu: OK

Att 0.00dB	BW LO	∅ 1.000mm	ZERO
			EXIT

Thermal Sensor

Exit Menu: OK

Att 0.00dB	Acc ON	∅ 2.00mm	ZERO
			EXIT

Pyroelectric Sensor

Edit: ▲▼ Cursor: ◀▶ Save: OK

Att 0.00dB	Trig 10.0%	∅ 10.00mm	
			EXIT

Att: Sets an attenuation or gain factor

BW: Sets the bandwidth of the photodiode input stage to High or Low

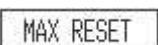
Acc: Switches the acceleration circuit for the thermal sensor input stage

Trig: Sets the trigger level for laser pulse detection.

∅ x.xxmm Set the input beam diameter for power or energy density calculation

ZERO Performs a zeroing for thermal sensors and dark current adjustment for photodiode sensors.

3.2.2.5 Max Reset Button



Sets back the Min, Max and Max/Min displays

3.2.2.6 Tuning Sound



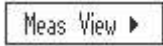
Switches on and off an audible tone for laser tuning support

3.2.2.7 Relative Measurements



Switches on and off the relative measurement mode

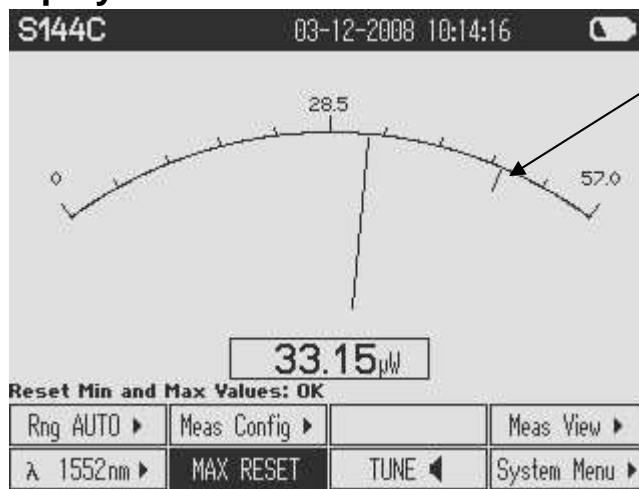
The main display will set to zero, the offset and the absolute power or energy value will be displayed in the sub displays. The bar graph and needle display will change to a measurement range from -10% to +10% of the set range. **3.2.3 Display Options**



Select Measurement Representation: OK

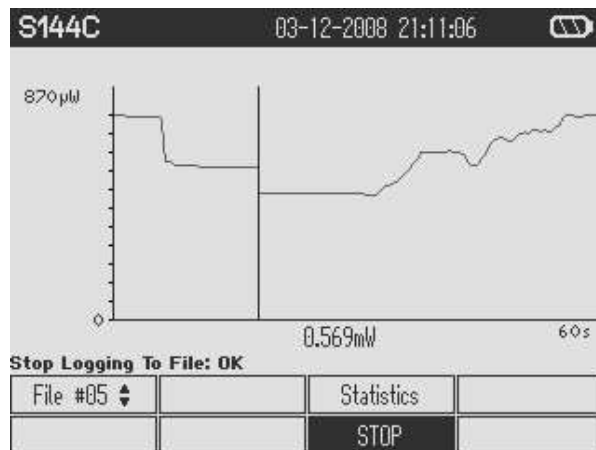
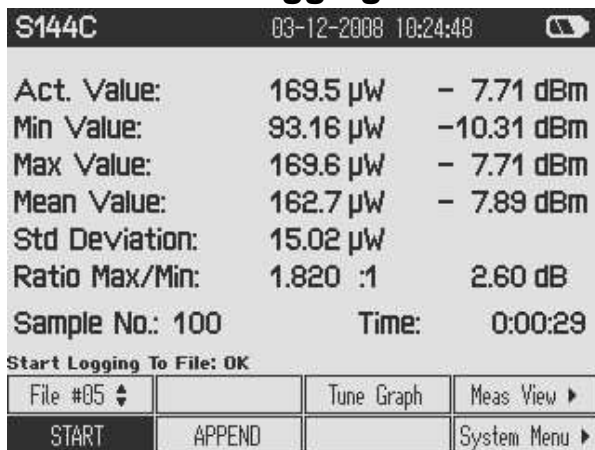
Numeric	Tune Graph	Statistics	<input checked="" type="checkbox"/> Needle
			EXIT

3.2.3.1 Needle Display



Max value indicator

3.2.3.2 Data Logging Screens



After pressing the START button the data that are sampled in these screens will be stored to the built in SD memory card on the selected file until STOP is pressed. With START the selected file will be overwritten.

3.2.4 Analog Output

The analog output provides the amplified photo-diode current or the amplified thermal or pyroelectric sensor voltage.

The signals from the analog outputs are not wavelength and zero corrected. The analog output voltage is range dependent and can be calculated to:

$U_{\text{Analog Out}} = 2V / \text{full scale range value} \times \text{measurement value}$ The analog output voltage can range from -0.3V to +2.3V.

3.2.5 Battery Charging

The PM100D is powered by a 1 cell LiPo+ battery that needs to be recharged intermittently by plugging the AC adapter or plugging the USB cable to a computer. To fully charge the battery it takes approximately 3-4 hours. A built in charging circuit automatically regulates and terminates the charging.

Following battery icons in the display header show the charging state from empty to full battery



The empty battery symbol starts blinking for one minute until the unit shuts off.

When an external power supply is plugged the symbols above change sequent until the battery is fully charged.

3.3 Computer Interface

The PM100D optical power meter contains a USB 2.0 interface. When connecting the PM100D to the PC first time, a new hardware will be found. For proper installing the PM100D it requires a NI-VISA runtime version on the PC (available on the National Instruments website www.ni.com) or from the data carrier that comes with the instrument. Allow installing and follow the dialog instructions. The PM100D comes with a utility software that easily enables remotely operating the PM100D (also PM100A and PM100USB) and visualizing and logging measurement data. Perform the setup.exe and follow the installing instructions. The LabVIEW source code of this application is included on the data carrier as well and can be used to build own applications or to modify the utility program to specific requirements (LabVIEW 8.5.1 or higher required).

4 Addresses

Our Company is represented by several distributors and sales offices throughout the world.

Europe

Thorlabs GmbH
Hans-Böckler-Str. 6
85221 Dachau
Germany

Sales and Support
Phone: +49 (0)8131-5956-0
Fax: +49 (0)8131-5956-99
Email: europa@thorlabs.com
Web: www.thorlabs.com

Japan

Thorlabs Japan, Inc.
Higashi Ikebukuro
Q Building 1st floor 2-23-2
Toshima-ku,
Tokyo 170-0013
Japan

Sales and Support
Phone: +81-3-5979-8889
Fax: +81-3-5979-7285
Email: sales@thorlabs.jp
Web: www.thorlabs.jp

USA

Thorlabs, Inc.
435 Route 206 North
Newton, NJ 07860
USA

Sales and Support
Phone: 1-973-579-7227
Fax: 1-973-300-3600
Email: sales@thorlabs.com
techsupport@thorlabs.com
Web: www.thorlabs.com

China

Thorlabs China
Oasis Middlerring Centre
3 Building 712 Room
915 Zhen Bei Road
Shanghai
China

Sales and Support
Phone: +86 (0)21-32513486 Fax: +86 (0)21-32513480
Email: chinasales@thorlabs.com
Web: www.thorlabs.com

Please call our hotlines, send an Email to ask for your nearest distributor or just visit our homepage <http://www.thorlabs.com>



Series PicoScope 3000 PC- Oszilloskopen

Handbuch

PS3000049-2

Copyright 2005-7 Pico Technology Limited. All rights reserved.

Inhaltsverzeichnis

1 Einführung	1
1 Übersicht	1
2 Sicherheitszeichen	1
3 Sicherheitshinweise	2
4 CE-Hinweis	2
5 FCC-Hinweis	3
6 Garantie	3
7 Rechtliche Hinweise	4
8 Warenzeichen	4
Firmenanschrift	5
2 Produktinformationen	6
1 Systemanforderungen	6
2 Installationsanleitung	6
Technische Daten	8
3 Fehlerbehandlung	9
1 Fehlercodes	9
2 Stromversorgung des PicoScope 3204/5/6	10
Index	11

1 Einführung

1.1 Übersicht

Die Serie PicoScope 3000 ist eine Reihe von High-Speed-PC-Oszilloskopen, die USB 2.0 vollständig unterstützen und abwärtskompatibel zu USB 1.1 sind.

Mit der Software von PicoScope können Oszilloskope der Serie PicoScope 3000 als PC-Oszilloskope und Spektrumanalysatoren verwendet werden. Mit dem Programm PicoLog können Oszilloskope der Serie PicoScope 3000 als Datenerfassungsgeräte eingesetzt werden. Vielleicht sind Sie auch an der Alternative interessiert, die verfügbaren API-Funktionen für die Entwicklung eigener Programme zum Erfassen und Analysieren von Oszilloskopdaten zu verwenden.

Ein typisches PicoScope 3000-Oszilloskop wird mit folgendem Zubehör geliefert:

- USB-Kabel passend zu beiden USB-Arten
- Software-CD
- Installationshandbuch

1.2 Sicherheitszeichen

Warnzeichen 1: Warndreieck



Dieses Sicherheitszeichen gibt an, dass an den angegebenen Anschlüssen eine Sicherheitsgefahr vorliegt, wenn die vorgeschriebenen Sicherheitsmaßnahmen nicht getroffen werden. Stellen Sie sicher, dass alle Sicherheitsunterlagen im Zusammenhang mit dem Produkt gründlich gelesen werden, bevor das Produkt verwendet wird.

Warnzeichen 2: Äquipotential



Dieses Sicherheitszeichen gibt an, dass die Außengehäuse der angezeigten BNC-Stecker das gleiche Potential haben (d.h. kurzgeschlossen sind). Der Benutzer muss daher die notwendigen Vorsichtsmaßnahmen ergreifen, um zu vermeiden, dass ein Potential zwischen den Außengehäuseanschlüssen der BNC-Anschlüsse angelegt wird, da dies zum Fließen eines hohen Stroms und damit zu Beschädigung am Produkt und/oder angeschlossenen Geräten führen kann.

1.3 Sicherheitshinweise

Wir empfehlen dringend, vor dem ersten Verwenden des Oszilloskops die allgemeinen Sicherheitsinformationen zu lesen. Die in das Gerät eingebauten Schutzvorrichtungen können außer Kraft gesetzt werden, wenn das Gerät nicht richtig benutzt wird. Dies kann zu einem Schaden am Computer oder zu Verletzungen bei Ihnen oder anderen führen.

Maximaler Eingangsspannungsbereich

Oszilloskope aus der PicoScope 3000-Palette sind auf die Messung von Spannungen im Bereich von -20 V bis + 20 V ausgelegt. Spannungen über ± 100 V können physische Schäden verursachen.

Netzspannung

Produkte von Pico Technology sind nicht für den Gebrauch mit Netzspannung ausgelegt. Verwenden Sie zum Messen von Netzspannung eine isolierende Differenzsonde, die speziell für hohe Quellspannungen ausgelegt ist.

Sicherheitserdung

Oszilloskope aus der Serie PicoScope 3000 werden über das mitgelieferte Kabel direkt mit der Masse des Computers verbunden. Dadurch werden Interferenzstörungen minimiert.

Wie bei den meisten Oszilloskopen sollte es vermieden werden, den Erdungsanschluss mit etwas anderem als Erde oder Masse zu verbinden. Verifizieren Sie im Zweifelsfall mit einem Multimeter, dass keine bedeutende Gleich- oder Wechselspannung anliegt. Diese Prüfung zu versäumen, kann zu Schäden am PC und zu Verletzungen bei Ihnen und anderen führen.

Grundsätzlich sollte man davon ausgehen, dass ein Produkt keine Schutzerdung hat.

Reparaturen

Das Oszilloskop enthält keine zu wartenden Teile: Reparatur und Kalibrierung erfordern spezielle Prüfgeräte und dürfen nur von Pico Technology durchgeführt werden.

1.4 CE-Hinweis

Die PC-Oszilloskope der Serie PicoScope 3000 entsprechen den Zielen der **EMC-Richtlinie 89/336/EWG** und die folgende Norm wurde angewendet: **EN61326-1 (1997) Klasse B** Emissionen und Störfestigkeit.

Produkte aus der Reihe PicoScope 3000 entsprechen auch den Zielen der Niederspannungsrichtlinie und die folgende Norm wurde angewendet: **BS EN 61010-1:2001 IEC 61010-1:2001** (Sicherheitsanforderungen für elektrische Geräte, Bedienelemente und Laboreinsatz).

1.5 FCC-Hinweis

Dieses Gerät entspricht den FCC-Vorschriften, Teil 15 (FCC: US-Behörde für Telekommunikation). Der Betrieb erfordert die Einhaltung der folgenden beiden Bedingungen:

- (1) Dieses Gerät darf keine schädlichen Störungen verursachen.**
- (2) Dieses Gerät muss jede empfangene Störung aufnehmen, einschließlich Störungen, die unerwünschte Effekte verursachen.**

Dieses Gerät wurde gemäß Teil 15 der FCC-Vorschriften geprüft und entspricht den Grenzwerten für ein digitales Gerät der Klasse B. Diese Grenzwerte sind darauf

ausgelegt, einen angemessenen Schutz vor gesundheitsgefährdenden Störungen in Wohngebäuden sicherzustellen. Dieses Gerät erzeugt und verwendet hochfrequente Spannungen und kann diese ausstrahlen; wenn es nicht anweisungsgemäß betrieben wird, kann es erhebliche Störungen des Funkverkehrs verursachen. Es gibt jedoch keine Garantie, dass bei einer bestimmten Einrichtung keinerlei Störungen auftreten. Wenn dieses Gerät den Radio- oder Fernsehempfang beeinträchtigt (was durch das Aus- und Einschalten des Geräts überprüft werden kann), wird dem Benutzer der Versuch empfohlen, diese Störungen durch eine oder mehrere der folgenden Maßnahmen zu beseitigen:

- Richten Sie die Empfangsantenne neu aus oder platzieren Sie diese an einer anderen Stelle.
- Vergrößern Sie den Abstand zwischen dem Gerät und dem Empfänger.
- Verbinden Sie das Gerät mit einer Steckdose, die zu einem anderen Stromkreis gehört als zu dem, an den das Empfangsgerät angeschlossen ist.
- Fragen Sie Ihren Händler oder einen erfahrenen Radio/Fernsehtechniker um Rat.

weitere Informationen über Sicherheit und Wartung finden Sie in den [Sicherheitshinweisen](#).

1.6 Garantie

Pico Technology garantiert für einen Zeitraum von 24 Monaten ab Auslieferdatum, wenn nicht anders angegeben, dass die Waren bei Lieferung frei von Material- und Verarbeitungsfehlern sind.

Pico Technology übernimmt keine Haftung für eine Garantieverletzung, wenn der Defekt durch angemessenen Verschleiß, absichtliche Beschädigung, Fahrlässigkeit, Missbrauch, abnormale Arbeitsbedingungen oder Nichtbeachtung von Pico Technologys mündlichen oder schriftlichen Hinweisen zu Lagerung, Installation, Inbetriebnahme, Gebrauch oder Wartung der Waren oder (falls keine Hinweise vorliegen) gutem Handelsbrauch oder falls der Kunde diese Waren ohne schriftliche Zustimmung von Pico Technology ändert oder repariert.

1.7 Rechtliche Hinweise

Das in dieser Version enthaltene Material wird nur lizenziert und nicht verkauft. Pico Technology Limited gewährt der Person, die das Programm installiert, eine Lizenz mit den folgenden Bedingungen:

Zugriff

Der Lizenznehmer stimmt zu, nur Personen Zugriff zur Software zu gewähren, die über diese Bedingungen informiert wurden und diesen zugestimmt haben.

Verwendung

Diese Programmversion darf nur mit Pico-Produkten oder mit Daten, die mit Hilfe von Pico-Produkten erstellt wurden, verwendet werden.

Copyright

Pico Technology Limited beansprucht das Copyright und behält sich alle Rechte an den

Materialien (Software, Dokumentationen usw.) dieser Version vor. Sie können diese Version in ihrem Originalzustand kopieren und weitergeben, dürfen aber einzelne Teile der Version nur zu Sicherungszwecken kopieren.

Haftung

Pico Technology und seine Bevollmächtigten sind, wenn nicht anders festgelegt, nicht haftbar für Verluste, Schäden oder Verletzungen, wie auch immer verursacht, die durch die Nutzung von Geräten oder Software von Pico Technology entstehen.

Zweckdienlichkeit

Zwei Anwendungen sind nie ganz gleich: Pico Technology kann keine Gewähr übernehmen, dass Geräte oder Software für einen bestimmten Zweck geeignet sind. Daher liegt es in Ihrer Verantwortung festzustellen, ob das Produkt für Ihre Anwendung geeignet ist.

Kritische Anwendungen

Diese Software ist für die Ausführung auf Rechnern vorgesehen, auf denen auch andere Software-Produkte ausgeführt werden. Aus diesem Grund ist es eine Bedingung dieser Lizenz, dass die Benutzung bei kritischen Anwendungen, wie beispielsweise Lebenserhaltungssystemen, ausgeschlossen wird.

Viren

Bei der Erstellung wurde diese Software ständig auf Viren überprüft. Wenn sie einmal installiert ist, sind Sie jedoch selbst für die Überprüfung auf Viren verantwortlich.

Unterstützung

Sind Sie mit der Leistung dieser Software nicht zufrieden, nehmen Sie Kontakt mit unserer technischen Abteilung auf. Sie wird versuchen, die Probleme innerhalb eines angemessenen Zeitraums zu beheben. Sind Sie danach immer noch unzufrieden, geben Sie Produkt und Software innerhalb von 28 Tagen an Ihren Händler zurück.

Upgrades

Sie können Upgrades kostenlos von unserer Internetseite www.picotech.com herunterladen. Wir behalten uns jedoch das Recht vor, Updates oder Ersatzlieferungen, die Ihnen zugesandt werden, zu berechnen.

1.8 Warenzeichen

Windows und **Exel** sind Schutzmarken der Microsoft Corporation. **Pico Technology Limited**, **DrDAQ** und **PicoScope** sind international registrierte Handelsnamen.

1.9 Firmenanschrift

Adresse:

Pico Technology Limited
The Mill House
Cambridge Street
St Neots
Cambridgeshire
PE19 1QB

Großbritannien

Telefon: +44 1480 396395

Fax: +44 1480 396296

E-Mail:

Technischer Support: support@picotech.com

Vertrieb: sales@picotech.com

Website:

www.picotech.com

2 Produktinformationen

2.1 Systemanforderungen

Für den Betrieb von Oszilloskopen der Serie PicoScope 3000 ist ein Computer erforderlich, auf dem Windows oder eines der folgenden Betriebssysteme ausgeführt wird (es gilt die jeweils höhere Anforderung):

Prozessor	Mindestanforderung: Pentium-Prozessor oder vergleichbare Leistungsklasse
RAM	256 MB Minimum.
Festplatte	10 MB Minimum.
Betriebssystem	Microsoft Windows XP SP2 oder Vista.
Ports	Mindestens kompatibel zu USB 1.1. Kompatibilität zu USB 2.0 wird empfohlen. Muss direkt mit dem Port oder einem Aktiv-HUB verbunden werden. Funktioniert nicht mit einem Passiv-Hub.

2.2 Installationsanleitung

Achtung:
Verbinden Sie kein Oszilloskop der Serie PicoScope 3000 mit dem PC, bevor die Software installiert ist.

Installieren Sie die Software gemäß der im Installationshandbuch Ihres Oszilloskops beschriebenen Vorgehensweise. Das Oszilloskop wird über das mitgelieferte USB-Kabel mit dem PC verbunden. Eine zusätzliche Stromversorgung ist nicht erforderlich, da der Strom aus dem USB-Port bezogen wird.

Überprüfen der Installation

Nachdem die Software installiert wurde, stellen Sie sicher, dass das Oszilloskop mit dem PC verbunden ist und starten sie dann das Programm PicoScope oder PicoLog. Das Programm sollte nun die angeschlossene Spannung anzeigen. Wenn Sie eine Messsonde und PicoScope verwenden, sollten Sie ein schwaches Netzspannungssignal von 50 oder 60 Hz im Oszilloskop-Fenster sehen, sobald Sie die Spitze der Sonde mit dem Finger berühren.

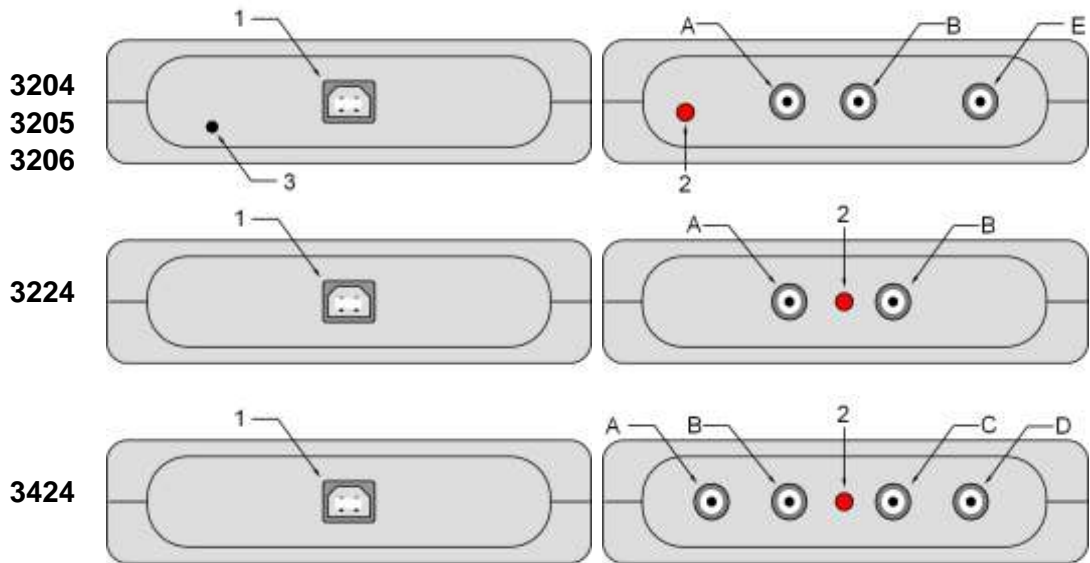
Standard-Oszilloskopanschlüsse

Oszilloskope der Serie PicoScope 3000 haben Standardanschlüsse. Auch der Eingangswiderstand ist standardmäßig, daher funktioniert die x10-Funktion mit Messsonden einwandfrei.

Der im folgenden Diagramm mit **E** bezeichnete BNC-Anschluss und im Oszilloskop hat zwei Funktionen. Bei normaler Verwendung ist es der Eingang für ein externes Triggersignal mit einstellbarem Schwellwert. Alternativ kann dieser Anschluss bei manchen Oszilloskopen auch verwendet werden, um Sinus-, Rechteck- und

Dreieckwellen auszugeben, die mit einer benutzerdefinierten Frequenz vor- und zurück laufen können. Der integrierte Signalgenerator kann über das Programm PicoScope oder über API-Aufrufe gesteuert werden. Der Signalgenerator kann auch verwendet werden, um bei eingestellter Ausgabe von Rechteckwellen die x10-Messsonden zu kompensieren.

Anschlussdiagramm



Produktinformationen

7

- 1 USB-Anschluss
- 2 LED. Zeigt durch Aufleuchten an, dass das Oszilloskop der Serie PicoScope 3000 Daten abtastet. 3 12-V-DC-, 500-mA-Eingang **A-D** Eingangskanäle A-D.
- E Externer Trigger / Signalgenerator

Masseschleifen

Bei starkem Rauschen oder Fehlspannungen bei Verwendung der Varianten PicoScope 3204/5/6 könnte ein Masseschleifenfehler vorliegen. Zu Ratschlägen zur Beseitigung dieses Problems siehe bitte "Stromversorgung des 3204/5/6".

Verlegung Ihres PicoScope-Oszilloskops an einen anderen USB-Anschluss

Wenn Sie das Oszilloskop der PicoScope Serie 3000 installieren, indem sie es in einen USB-Anschluss stecken, verknüpft Windows die Pico-Treibersoftware mit diesem Anschluss. Wenn Sie nun das Oszilloskop später an einen anderen USB-Anschluss anschließen, zeigt Windows erneut den "Hardware-Assistent" an. Folgen Sie in diesem Fall einfach den Schritten in der Kurzanleitung unter der Anweisung "Schließen Sie das PC-gestützte Oszilloskop der Serie PicoScope 3000 an den PC an...". Da die Software, die Sie benötigen, bereits auf Ihrem Computer installiert ist, müssen Sie die Pico Software-CD nicht erneut einlegen.

2.3 Technische Daten

	3204	3205	3206	3224	3424
Vertikale auflösung	8 bits	8 bits	8 bits	12 bit	
Analog-bandbreite	50 MHz	100 MHz	200 MHz	10 MHz	

Maximale abtastrate					
1-Kanal	50 MS/s	100 MS/s	200 MS/s	20 MS/s	20 MS/s
2-Kanal	50 MS/s	100 MS/s	100 MS/s	10 MS/s	10 MS/s
3/4-Kanal	-	-	-	-	5 MS/s
Repetitive Signale	2.5 GS/s	5 GS/s	10 GS/s	-	-
Trigger-bandbreite	50 MHz	100 MHz	150 MHz	10 MHz	
Puffergrösse					
1-Kanal	256 K	512 K	1 M	512 K	512 K
2-Kanal	128 K	256 K	512 K	256 K	256 K
3/4-Kanal	-	-	-	-	128 K
Eingänge	2 Kanäle über BNC				4 Kanäle über BNC
	1 MW Impedanz AC/DC-Kopplung 20 pF Eingangskapazität				
Ausgänge					
Signalgenerator	(1)	(2)		-	
Externer Trigger	1 BNC-Ausgang gemeinsam mit Signalgenerator Variabler Triggerschwellwert ± 20 V ansteigend/abfallend 12,2 mV Auflösung 1 MW Impedanz			-	
Spannungsbereiche	± 100 mV bis ± 20 V Bereiche in 1, 2, 5 Stufen			± 20 mV bis ± 20 V	
Genauigkeit	3 % Spannung 50 ppm Zeit			1 % Spannung 50 ppm Zeit	
Umgebungsbedingungen	0 °C bis 70 °C (25 °C für die angegebene Genauigkeit)			0 °C bis 70 °C (20 °C bis 30 °C für die angegebene Genauigkeit)	
Temperaturbereich	25 % bis 75 % relative Luftfeuchtigkeit			25 % bis 75 % relative Luftfeuchtigkeit	
Feuchtigkeit					
Überlastungsschutz					
Kanäle	± 50 V			± 100 V	
Externer Trigger	± 30 V			-	
PC-Verbindung	USB 2.0 Kompatibel mit USB 1.1				
Stromversorgung	Aus USB-Port: 4,6 bis 5,25 V; 500 mA Externe Stromversorgung ist nicht erforderlich.			Aus USB-Port	
Abmessungen	140 mm x 190 mm x 45 mm				
Prüfzeichen	CE-Norm ; FCC-Norm				

(1) 1 BNC gemeinsam mit externem Trigger. Festfrequenz 1kHz. 5 V-Rechteckwelle. 600 W Impedanz.

(2) 1 BNC gemeinsam mit externem Trigger. Variable Frequenz 100 Hz bis 1 MHz. 5 V-Rechteckwelle. 1 V-Sinuswelle und Dreiecksfunktionen. Wobbelwiederholungsfunktion. Dual Slope-Funktion. 600 W Impedanz.

3 Fehlerbehandlung

3.1 Fehlercodes

Sehen Sie in diesem Abschnitt nach, wenn Sie PicoScope oder PicoLog verwenden.

PicoLog meldet Fehlercode 1.

Dieser Fehler wird gemeldet, wenn mehr als 4 Oszilloskope auf einem PC geöffnet werden. Mit PicoLog können nicht mehr als 4 Oszilloskope zugleich verwendet werden.

PicoScope oder PicoLog meldet Fehlercode 2.

Dieser Fehler wird gemeldet, wenn dem Treiber nicht ausreichend Speicher zur Verfügung steht, um das Oszilloskop zu betreiben. Weitere Informationen finden Sie im Abschnitt [Systemanforderungen](#).

PicoScope oder PicoLog meldet Fehlercode 3.

Dieser Fehler zeigt an, dass auf Ihrem System kein Oszilloskop aus der Serie PicoScope 3000 gefunden wurde. Stellen Sie sicher, dass die Software installiert ist, bevor das Oszilloskop mit der USB-Buchse verbunden wird und starten Sie Ihren Computer neu.

Stellen Sie sicher, dass das Oszilloskop im Geräte-Manager unter dem Eintrag USB aufgeführt wird. Wenn das Oszilloskop hier nicht aufgeführt wird, wenden Sie sich an den Technischen Support von Pico.

PicoScope oder PicoLog meldet Fehlercode 4, 5 oder 6.

Dieser Fehler wird gemeldet, wenn es ein Problem mit dem Oszilloskop selbst gibt. Solche Probleme können daraus entstehen, dass die Konfigurationseinstellungen beschädigt sind, ein Hardware-Fehler vorliegt oder ein spezielles Programm nicht richtig funktioniert.

Ziehen Sie den Stecker des Oszilloskops, warten Sie ein paar Sekunden und stecken Sie ihn wieder in die USB-Buchse. Wenn der Fehler immer noch gemeldet wird, fragen Sie den Technischen Support von Pico.

PicoScope oder PicoLog meldet Fehlercode 7.

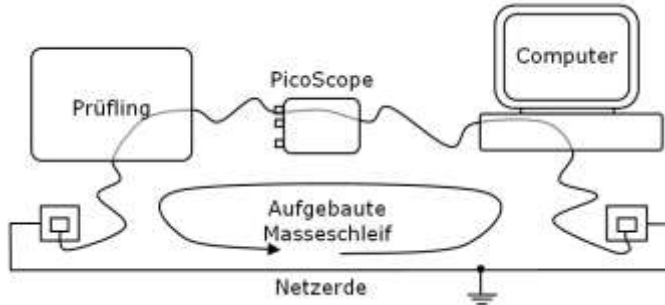
Dieser Fehler wird gemeldet, wenn das Betriebssystem zu alt ist, um das Oszilloskop der Serie PicoScope 3000 zu unterstützen. Weitere Informationen finden Sie im Abschnitt [Systemanforderungen](#).

3.2 Stromversorgung des PicoScope 3204/5/6

Die PC-gestützten Oszilloskope PicoScope 3204/5/6 werden normalerweise über die USB-Schnittstelle des Computers mit Strom versorgt. Liegen jedoch der Computer und

der Prüfling beide in Bezug zur gleichen Masse, kann sich eine Masseschleife aufbauen. Dies kann die Gleichstromgenauigkeit und Störfestigkeit beim Messen von Signalen mit niedrigen Pegeln verschlechtern.

Eine Masseschleife baut sich normalerweise auf, wenn das PicoScope an einen vom Netz gespeisten Computer angeschlossen ist und zum Messen eines Signals an einem anderen netzgespeisten Gerät verwendet wird. In diesem Fall baut sich die Masseschleife über die Netzerde auf, wie nachstehend abgebildet:



Die meisten Laptop-Netzteile (Ladegeräte) sind erdfrei und haben keinen Massebezug. Verursacht jedoch der Anschluss Ihres geerdeten Laptop-Netzteils Störpegel-/Versetzungsfehler, können Sie das Oszilloskop entweder verwenden, während der Laptop im Akkubetrieb ist, oder das Oszilloskop über den Netzadapter im Lieferumfang mit Strom versorgen.

Bei Bedarf sollte der Netzadapter in die Buchse hinten am Oszilloskop (neben der USB-Buchse) eingesteckt werden. Sie können den Netzadapter im Betrieb ohne weiteres anschließen und abziehen, ohne eine Beschädigung des Oszilloskops zu riskieren.

Index

Rechteckwelle 6

A

API 1

API-Funktionen 1

Serie PicoScope 3000 2, 6

B

Signalgenerator 6

BNC-Anschluss 6

D

Datenerfassungsgerät 1

E

F Externer Trigger 6

USB 1.1 1, 6

Firmenanschrift 5

H

Hochgeschwindigkeit 1

K

Kalibration 2

M

Maximaler Eingangsspannungsbereich 2

Messsonde 6

R

Reparatur 2

S

Sicherheitshinweis 3

Sonde 6

Spektrumanalysator 1

Systemanforderungen 6

T

Technische Daten 8

U

USB 2.0 1, 6

P

PC-Oszilloskope 1, 2
PicoLog-Programm 1
PicoScope 3000-Serie 1
PicoScope-Software 1, 6
Prüfgeräte 2

Pico Technology Ltd

The Mill House
Cambridge Street
St Neots PE19 1QB
Großbritannien
Tel: +44 (0) 1480 396 395
Fax: +44 (0) 1480 396 296
Web: www.picotech.com

PS3000049-2 24.4.07

Copyright 2005-7 Pico Technology Limited. All rights reserved.

